2004

Non-linear development of the secular bar-mode instability in rapidly rotating neutron stars

Shangli Ou
Louisiana State University and Agricultural and Mechanical College, sou1@lsu.edu

NON-LINEAR DEVELOPMENT OF THE SECULAR BAR-MODE INSTABILITY IN RAPIDLY ROTATING NEUTRON STARS

A Dissertation

Submitted to the Graduate Faculty of the
Louisiana State University and
Agricultural and Mechanical College
in partial fulfillment of the
requirements for the degree of
Doctor of Philosophy

in

The Department of Physics and Astronomy

by
Shangli Ou
B.S., Nanjing University, 1995
M.S., Louisiana State University, 2001
M.S. in Sy. Sc., Louisiana State University, 2005
December, 2004

Acknowledgments

First, I would like to thank my wife, Yu, and my parents for their unselfish support and understanding during my five-year journey at LSU, I will remember all the joys and sadness we have shared through these years.

I am indebted to Joel Tohline, Alumni Professor of LSU, for directing me to this research work and the field of high performance parallel computing. Without his elegant mentor art, I would have fallen away from science a long time ago; and without his formidable editorial skills, this dissertation would never have been finished. I am also grateful to Professor Juhan Frank for his helpful thoughts and bright insights, which provided me with different perspectives of thinking. Special thanks go to Lee Lindblom from Caltech, who gave lots of valuable "electronic" comments and advice on this dissertation work.

I would like to thank two senior LSU theoretical astrophysics group members — Eric Barnes and, especially, Patrick Motl — for helping me with the LSU hydrodynamics code, visualization tools, and various computer skills needed in this work. Thanks go to Gabriela Gonzalez for directing us to use the most updated LIGO data. Thanks also go to Mario D'Sousa and Karly Pitman for their help and friendship. I have enjoyed the time I have spent with many LSU physics graduate students, whose names partly appear here: Weichang Zhao, Jian Zuo, Mitsuko Murakami, Vayu Gokhale, Ravi Kumar, Xiaomeng Peng, and Ilsoon Park.

At this moment, I would also like to thank Yuntong Zhang, senior engineer of Beijing Institute of Spacecraft System Engineering, Lin Liu, professor of Nanjing University, and Xinhao Liao, Director of Shanghai Astronomical Observatory, for their help in my career.

This work has been supported in part by the U.S. National Science Foundation through grants AST-9987344, PHY-0326311, AST-0407070 and NASA grant NAG5-13430 at LSU. This research has relied heavily upon two beowulf clusters at LSU — SuperMike and

SuperHelix —, which are facilities operated by the Center for Computation and Technology whose funding largely comes through appropriations by the Louisiana state legislature.

Table of Contents

List of Tables

List of Figures

Abstract

We present results from investigations of the nonlinear development of the secular bar-mode instability that is driven by gravitational radiation-reaction (GRR) forces in rotating neutron stars. Our fully three-dimensional hydrodynamical simulations have shown that, in the absence of any competing viscous effects, initially uniformly rotating axisymmetric $n = 1/2$ polytropic stars with a ratio of rotational to gravitational potential energy greater than the critical limit are driven by GRR forces to a bar-like structure, as predicted by linear theory. The pattern frequency of the bar slows to nearly zero, that is, the bar becomes almost stationary as viewed from an inertial frame of reference as GRR forces remove energy and angular momentum from the star. In this "Dedekind-like" state, rotational energy is stored as motion of the fluid in highly noncircular orbits inside the bar. However, in a very short time after its formation, the bar loses its initially coherent structure as the ordered flow inside the bar is disrupted by what appears to be a purely hydrodynamical, short-wavelength, "shearing" type instability. The gravitational waveforms generated by such an event are determined, and an estimate of the detectability of these waves is presented. Our results also suggest that since a Dedekind-like configuration is susceptible to this turbulent instability, the long believed evolutionary path of a secularly unstable star driven by gravitational radiation toward the Dedekind ellipsoid, becomes questionable.

1. Introduction

The structure and stability of rapidly rotating and self-gravitating fluid systems, i.e., rotating stars or galaxies, have been studied extensively over centuries by many mathematicians such as Maclaurin, Jacobi, Dedekind, Riemann, and especially Chandrasekhar (1969). Through the classical work of these forerunners, it has been well understood that a uniformly-rotating and uniform-density axisymmetric star while treated as an incompressible fluid, i.e., a Maclaurin spheroid, may undergo a variety of nonaxisymmetric instabilities when it rotates sufficiently fast. The two lowest-order instabilities — the so-called bar-mode instabilities — have the shortest growth times and become dominant in most cases.

The first instability can set in when a star is rotating sufficiently rapidly that $\beta \equiv |T/W| \geq 0.14$, where T is the rotational kinetic energy and W is the gravitational potential energy of the star, provided that there is some kind of dissipation mechanism such as gravitational radiation or viscosity acting within the star. This instability is expected to cause the star to deform into a rotating bar-like structure in the inertial frame, and develop on a time scale much longer than the star's characteristic dynamical time, $\tau_{\rm dyn} \equiv 1/\sqrt{\pi G \bar{\rho}}$, where G is the universal gravitational constant, $\bar{\rho}$ is the mean density of the star. Thus it is referred to as the secular bar-mode instability. The final fate of a secularly unstable star is thought to be evolution to a triaxial configuration on the so-called Jacobi/Dedekind ellipsoidal sequences. The second instability occurs at a higher β value, $\beta \geq 0.27$, and also causes the deformation into a bar-like structure (some kind of Riemann ellipsoid). However, this latter instability develops on a time scale that is comparable to $\tau_{\rm dyn}$, therefore it is often referred to as the dynamical bar-mode instability.

Recently, these two instabilities have drawn a considerable amount of attention from the gravitational wave community because, according to Einstein's theory of General Relativity, the bulk mass motion involved in the transition from a spheroidal configuration into a bar-like configuration will emit gravitational waves. Relatively strong gravitational-wave signals

may be emitted especially when these instabilities arise in rapidly rotating neutron stars, which rotate with a period of a couple of milliseconds and are extremely compact (with a mass ~ 1.4 solar masses squeezed into a volume that is only a few tens of kilometers in diameter). Such signals are potentially detectable by the Laser Interferometer Gravitational Wave Observatory (LIGO), which is designed to detect gravitational waves that come from various astrophysical sources and in so doing, test the validity of Einstein's theory of general relativity.

The objective of this work is two-fold: The major task is to model the nonlinear development of the secular bar-mode instability in rapidly rotating neutron stars and predict the wave forms of gravitational wave signals arising from this instability; this should help LIGO detect the gravitational waves and identify such a source in our universe. At the same time, the credibility of the long-believed evolutionary path of a secularly unstable star that is driven unstable by gravitational radiation reaction (GRR) forces will be examined.

1.1 Astrophysical Relevance

The bar-mode instabilities just discussed are of broad astrophysical interest in the context of star formation, stellar structure, and stellar stability because all stars in our universe are rotating. Stars that are sufficiently rapidly rotating will become unstable to either a dynamical or secular bar-mode instability, and evolve from an initially spheroidal-like configuration into a bar-like structure. Although it is very hard to directly observe a bar-like structure that might form in an individual star because the radii of stars are too small compared to their distances, we do observe bar-like structures in galaxies. In fact, about a third of all spiral galaxies in Hubble's classification of galaxies have spiral arms that emerge from the ends of a pronounced bar residing in the galaxy. By way of illustration, Figure 1.1 shows the image of the galaxy NGC3504; a bar-like structure is clearly seen in the central region of this galaxy. As a comparison, Fig. 1.2 shows an image from a 3D simulation of a rapidly rotating proto-stellar cloud that was unstable to the above

mentioned dynamical bar-mode instability. It shows that the initially axisymmetric cloud has deformed into a bar-like configuration with two arms spiraling out from both of the bar ends. The similarities between these two figures suggest that the bar-mode instability is indeed a very common phenomenon in our universe, even though one of the configurations is formed by a large cluster of stars while the other is made of gas.

In most realistic cases, astrophysical fluid systems range from highly compressible systems, such as protostellar clouds, to extremely compact and nearly incompressible objects, such as neutron stars. However, to solve the stability problem of these compressible systems is so difficult that only the stability analysis of uniform density configurations, i.e. incompressible systems, is analytically solved. Nevertheless, the stability analysis of incompressible fluid systems does help to shed some light on that of compressible systems. Therefore, although we are going to be dealing with compressible configurations with rather complex internal flows, it is convenient to set the context by first discussing what is known from analytical studies about uniform-density, incompressible configurations (Chandrasekhar, 1969).

In the classical literature on incompressible fluid flows, an object with a bar-like sturcture is described mathematically as an ellipsoid with three principal axes, namely, the major axis a, the intermediate axis b and the minor axis c, which is normally the rotation axis of the configuration. Figure 1.3 shows the parameter space for an incompressible triaxial object: the horizontal axis denotes the ratio b/a, the vertical axis is the ratio c/a. The straight line segment MT at $b/a = 1$ represents the Maclaurin spheroid "sequence" with M representing a sphere and T representing an infinitesimally thin disk. This axisymmetric sequence largely represents possible initial structures for rotating stars. As one moves along this sequence, from M to T, a star spins up. "S" identifies the point where the Maclaurin spheroids become secularly unstable to the bar-mode instability; it also identifies where the Jacobi/Dedekind sequences (curve SO) branch off Maclaurin sequence. "D" is the point where the Maclaurin spheroids become dynamically unstable to the bar-mode instability,

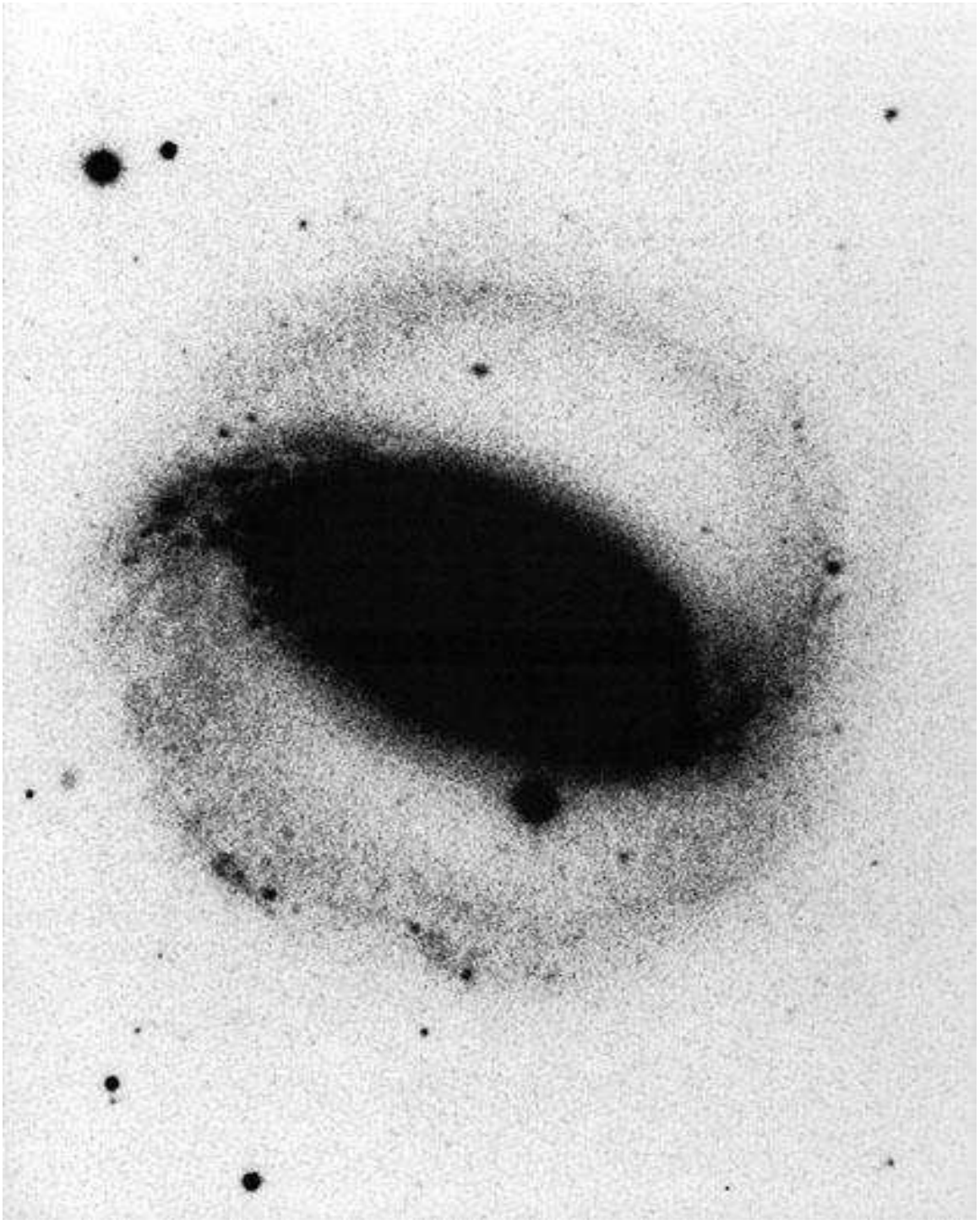

Figure 1.1: Image of NGC 3504 (Courtesy of the Observatories of the Carnegie Institution of Washington), which belongs to the class of barred-spiral galaxies. The central region has a very pronounced bar-like shape.

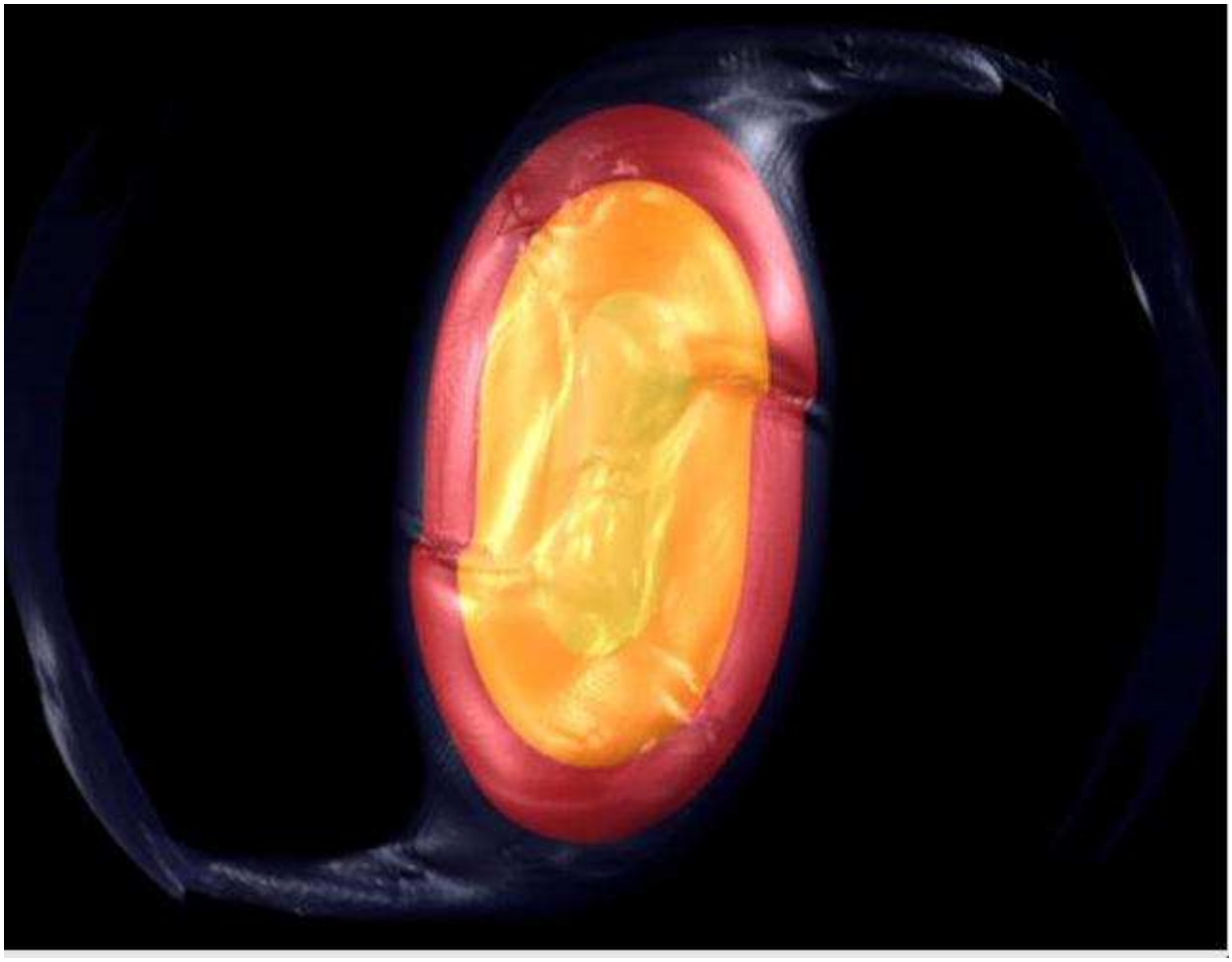

Figure 1.2: Image of a simulated protostellar gas cloud that is undergoing the dynamical bar-mode instability. It has developed a bar-like shape and spiral arms very similar in structure to the galaxy NGC3504. The numerical simulation from which this image has been drawn reproduces a portion of the results discussed by Cazes & Tohline (2000).

and the ellipsoidal sequence "DO" that branches off at point D traces out a series of more and more elongated "Riemann ellipsoids".

As mentioned earlier, the secular instability happens over a much longer time scale than the dynamical instability and requires some kind of dissipation. A secularly unstable Maclaurin spheroid will evolve into different ellipsoid configurations depending on the particular type of dissipation mechanism that is involved in driving the instability. A rigidly rotating Jacobi ellipsoid has a lower total energy than the corresponding Maclaurin spheroid that has the same mass, angular momentum and volume, but the angular momentum *distribution* is different between Jacobi ellipsoids and Maclaurin spheroids. Hence, in order for a Maclaurin spheroid to evolve to a Jacobi ellipsoid, a mechanism that is capable of removing energy from and redistributing angular momentum within the system is needed. Normal fluid viscosity is such a mechanism, so it is generally thought that viscosity will cause a secularly unstable Maclaurin spheroid to evolve into a Jacobi ellipsoid. On the other hand, Dedekind found that there is another special ellipsoidal configuration (now referred to as a "Dedekind ellipsoid") that has lower total energy and angular momentum than the corresponding Maclaurin spheroid that has the same mass and circulation. Interestingly, Dedekind ellipsoidal configurations have the same geometric shapes as Jacobi configurations — hence, the two sequences overlap in Fig. 1.3 — but the rotational properties are different. Jacobi ellipsoids are rigidly rotating and therefore have no internal flows in a frame corotating with the bar; but Dedekind ellipsoids have very large internal rotational flows, yet the ellipsoidal configuration itself remains stationary in the inertial frame. A mechanism that is capable of removing energy and angular momentum from the system while conserving circulation is required in order for a Maclaurin spheroid to evolve into a Dedekind ellipsoid. Since GRR forces are able to radiate energy and angular momentum away from the system, yet conserve circulation, it is generally thought that a secularly unstable Maclaurin spheroid will evolve into a Dedekind ellipsoid in the presence of GRR forces. Jacobi ellipsoids have been extensively studied over the past century. Dedekind

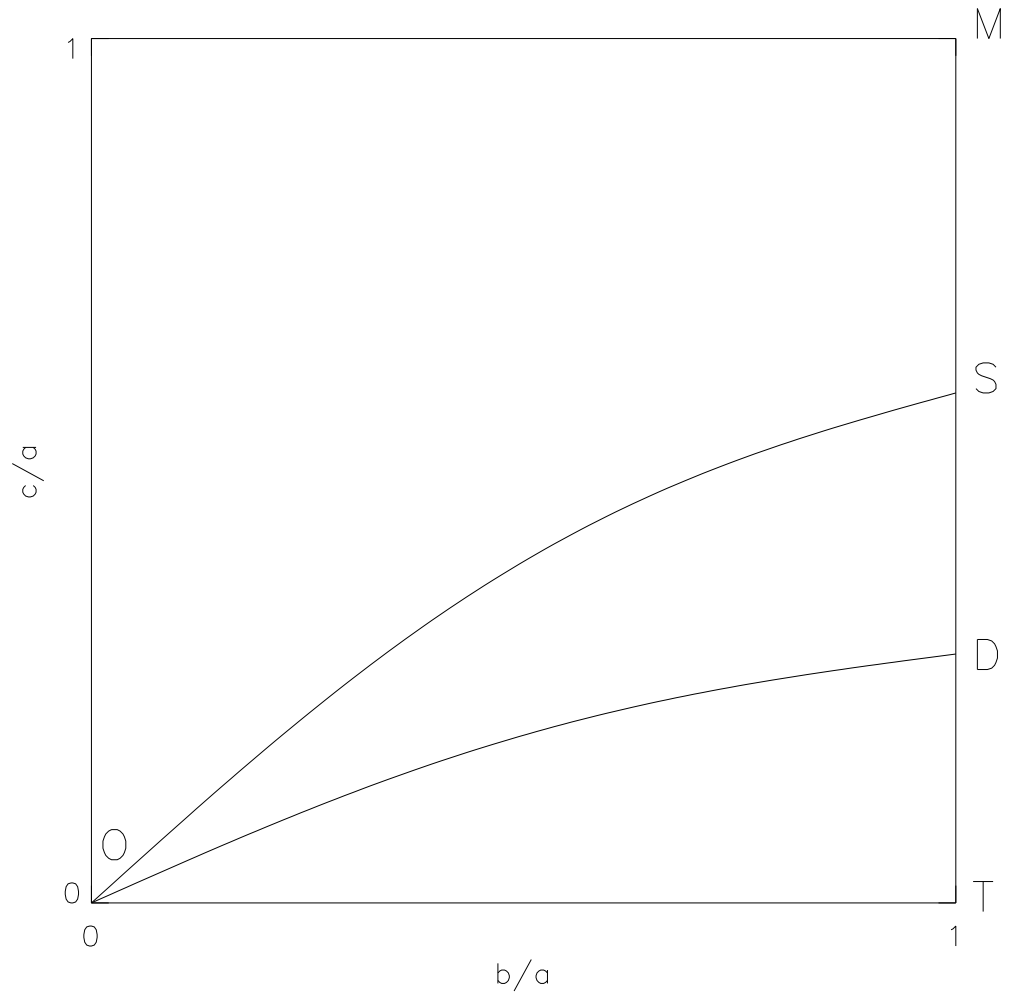

Figure 1.3: Schematic illustration of the parameter space occupied by incompressible, triaxial equilibrium models of stars. Details and a complete quantitative description of various sequences can be found in Chandrasekhar (1969). The straight line MT represents the Maclaurin spheroid sequence, with M representing a sphere and T representing an infinitesimally thin disk. As one moves along this sequence from M to T, a star spins up but maintains an axisymmetric ($b/a = 1$) structure. "S" is the point where Maclaurin spheroids become secularly unstable to the bar-mode instability, and the Jacobi/Dedekind sequences (curve SO) branch off Maclaurin sequence. "D" is the point where Maclaurin spheroids become dynamically unstable to the bar-mode instability, and a Riemann ellipsoid sequence branches off along curve DO.

ellipsoids, on the other hand, are rarely visited. They mostly only exist in mathematical theory. So, one interesting question in astrophysics is, "Can nature make Dedekind ellipsoids?" Furthermore, if Dedekind ellipsoids do exist in our universe, are they stable or not? Our current work is aimed at studying the GRR-driven bar-mode instability in an effort to cast some light on these issues.

1.2 The Relevance of the Bar-mode Instability to Gravitational Wave Detection

According to Einstein's theory of General Relativity, space-time is curved by gravity; masses that are in asymmetric motion will change the curvature of the space-time around themselves and cause space-time ripples to propagate away in the form of gravitational waves, which will carry energy and angular momentum away from the system. In order to test the validity of this prediction of general relativity, the gravitational wave community has been working very hard trying to detect gravitational waves. However, almost ninety years have passed since Einstein's formulation of general relativity, yet no direct detection of gravitational waves has even been made. This is because gravitational wave signals are extremely weak compared to electromagnetic waves. To date, the best proof of the existence of gravitational waves is an indirect observational proof from the Taylor-Hulse binary pulsars (Hulse & Taylor, 1975), which have been shown to have a gravitational-radiation-driven orbital decaying rate that matches the predictions of general relativity very well.

The Laser Interferometer Gravitational Wave Observatory (LIGO) uses ground-based detectors to detect gravitational waves from various astrophysical sources in the high frequency band (from a few tens of hertz to a few kilohertz), but the Laser Interferometer Space Antenna mission (LISA) will utilize space-based detectors to detect gravitational waves within a low frequency band (below 1 millihertz). They both make use of laser interferometry technology to detect very tiny length variations in the curved space-time caused by passing gravitational waves. The LISA mission is still in an early development stage;

its launch is planned to be in 2013 followed by a planned five-year operation. LIGO is now in operation and is being pushed toward its designed optimal sensitivity.

In LIGO's operation, the so-called template matched filtering method will be utilized to dig gravitational wave signals out from the daily recorded data. In order for LIGO to work effectively, numerous accurate and reliable gravitational-wave signal templates must be generated numerically. Large-scale and high-resolution numerical simulations are being used to produce model wave-form templates from different gravitational-radiation related astrophysical phenomena, such as inspiraling binary black holes, binary neutron stars, the core collapse of massive stars, and rapidly rotating neutron stars. The strength of the gravitational radiation and hence, the amplitude of gravitational waves from these systems will depend on the ratio of $G\mathrm{M}/(Rc^2)$, where c is the speed of light, and M and R are the mass and radius of the system, respectively. In order for a neutron star to radiate gravitational waves, it needs to have some asymmetric structure. Since a typical neutron star has $\mathrm{M} \sim 1.4\mathrm{M}_\odot$ (where $\mathrm{M}_\odot$ denotes for solar mass) yet has R $\sim$ a few kilometers, it is a very compact object with a reasonably strong gravitational field, $G\mathrm{M}/R \approx 0.2c^2$. Hence, a neutron star with only a tiny asymmetry may radiate strong gravitational waves. In addition, however, the strength of a gravitational-wave signal from a rotating neutron star will depend on its spin frequency raised to some power ($\sim \omega^5$, as discussed in Chapter 3). Radio observation (e.g., Backer et al. 1982) reveal that the rotation period of neutron stars can be as short as a few milliseconds! Thus, the gravitational radiation emitted from neutron stars can be very strong.

Unlike electromagnetic radiation, which can be generated by a time-varying dipole electric field, the lowest-order term in the expansion form of gravitational radiation comes from the time-variation of the $l = m = 2$ quadrupole moment of the mass distribution (Thorne, 1969). It is this lowest-order moment that should generally contribute most to the gravitational radiation, so the quadrupole nature of the bar-mode instability makes it one of the most promising physical mechanisms for the generation of gravitational waves that might

be detectable by LIGO. Detweiler & Lindblom (1977) and Lai & Shapiro (1995) have used simplified, approximate numerical methods to follow the nonlinear evolution of rotating neutron stars that are susceptible to the secular (or the dynamical) bar-mode instability. As is discussed in Chapter 2, for example, Lai & Shapiro (1995) have used circulation conservation to construct sequences of quasi-equilibrium ellipsoidal configurations to mimic the evolutionary paths of rotating neutron stars. As multi-dimensional hydrodynamical techniques have matured, and computing power has dramatically increased over the past decades, it has become possible to study the nonlinear development of the secular bar-mode instability in a much more realistic manner. These new developments have provided us with the motivation and capability to carry out the work presented here. We have not only modelled the linear and nonlinear development of the secular bar-mode instability in rapidly rotating neutron stars, but we have also estimated the detectability of gravitational waves generated by this instability.

A more complete background discussion of bar-mode instabilities and their relevance to astrophysical sources of GR is presented in Chapter 2. Chapters 3 and 4 describe the modeling techniques that we have used in this investigation. Chapter 5 compares our model of an oscillating sphere to the predictions of linear theory. Chapter 6 presents results from simulations of several different rotating neutron star models. Finally, a summary of this work is given in Chapter 7.

2. Background

2.1 Classification of Stellar Oscillation Modes

The stability of the normal modes of uniformly-rotating stars has been studied extensively over the past century by the means of normal mode analysis (see, e.g., Cox 1980), in which the perturbations (density, velocity, pressure, etc.) are decomposed into infinite modes via multipole expansion onto spherical harmonics with radial, polar, and azimuthal quantum numbers (k, l, m), therefore the angular and time dependence of each mode can be written as $e^{im\phi+i\omega t}$, where ω is the angular eigenfrequency of each mode. According to their characteristics and forces that drive them, these oscillations are classified into a variety of modes listed below.

The p-mode (pressure or acoustic mode) is driven by pressure between fluid elements. Its oscillations can be both radial and nonradial. Because the radial component of its fluid displacement vector is much larger than the tangential component, its oscillation is dominant by radial pulsations. P-modes generally have high angular eigenfrequencies and occupy the high frequency band region. The eigenfrequency tends to infinity as k increases, thus the lowest order of p-modes ($k = 1$) has the lowest frequency compared to other modes in its family.

The g-mode is another family of modes that is frequently confronted in the study of stellar structure and oscillations, whose restoring force is the buoyancy force inside the fluid. Its displacement vector has a dominant tangential component compared to the radial component. Contrary to the p-mode, the g-mode occupies the low frequency band region, its eigenfrequency tends to zero as k increases, the lowest order of g-modes ($k = 1$) has the highest frequency in its family.

The f-mode (fundamental mode) is a pure nonradial mode of oscillation whose radial quantum number k is zero, i.e. the radial eigenfunction has no nodes (zeroes) between the

center and the surface of the star. Its radial eigenfunction goes to zero only at the center of the star and reaches maximum at the surface; this feature makes the f-mode more like a surface-wave. For a given pair of polar and angular quantum numbers (l, m), there exists only one f-mode, which has an intermediate frequency compared to p-mode, which occupies the high frequency band, and g-mode, which occupies the low frequency band. Therefore, the f-mode has an intermediate character to p-mode and g-mode, so it is thought of as the fundamental pressure mode of the star (Andersson, 2003).

Many other modes also may appear in a rotating star, such as Rossby modes (r-modes) driven by the Coriolis force due to the rotation of the star, and so-called w-modes that arise only in the context of general relativity. These will not be discussed further.

2.2 Review of the Secular Bar-mode Instability

For over thirty years, it has been known that the f-mode in a rotating star undergoes some secular instability due to gravitational radiation (GR). This instability, generally called CFS (Chandrasekhar-Friedman-Schutz) instability, was first discovered by Chandrasekhar (1970) while studying the $l = m = 2$ f-mode of rigidly rotating and uniform-density stars with incompressible equations of state (i.e., the Maclaurin spheroids). This work was extended by Friedman & Schutz (1978) and Comins (1979a, 1979b) to stars with arbitrary equations of state and higher azimuthal mode numbers ($m > 2$). It was shown that this instability is generic to the f-mode in the sense that for a star rotating with any frequency Ω, f-modes with sufficiently large m will be unstable, because ω (the angular eigenfrequency of the mode as measured in the inertial frame) and $\omega - m\Omega$ (the same frequency as measured in a frame that is corotating with the star) will have opposite signs.

Because the high m modes have very long growth times, the $l = |m| = 2$ f-mode which has the shortest growth time in its family is of special interest here. Since the star will deform into a bar-like shape if this mode grows, the instability is also referred to as bar-

mode instability for $m = 2$ case. According to the linear perturbation theory, the stability of this $l = |m| = 2$ f-mode is as follows:

For rotating stars, there are two kinds of modes. One of them is the $m = -2$ mode, which is said to be forward moving because it is moving in the same direction as the rotation of the star, yet the other one is the $m = 2$ mode which is backward moving because it is moving in the opposite direction.

For nonrotating stars, these two modes are degenerate with each other, having the same oscillation frequency in the inertial frame but with different signs. The forward going wave has positive frequency and the backward going wave has negative frequency. GR tends to remove positive or negative angular momentum from a mode depending on which direction the wave moves in the inertial frame. For the forward going wave, which has positive angular momentum in the inertial frame, GR radiates away positive angular momentum, thus it brings down the value of the angular momentum and therefore damps this mode. On the other hand, the forward going mode also has positive angular momentum in the corotating frame of the star, so it is also damped in the corotating frame because positive angular momentum is radiated away. Similarly, the backward moving wave carries negative angular momentum in both frames, and GR radiates away negative angular momentum, thus it brings down the magnitude of the negative angular momentum in both frames and therefore damps the backward moving wave.

When the star spins up, the frequency of the forward moving wave remains positive in both the inertial and corotating frames, but the original negative frequency of the backward going wave starts to increase (but decrease in magnitude since it is initially negative) as viewed in the inertial frame. If the star is rotating slowly enough, the signs of the frequencies won't change, so the situation is very close to the non-rotating case, that is, gravitational radiation will damp both modes. However, when the star spins up to some point where the frequency of the backward going wave in the inertial frame crosses zero, a dramatic change happens. At this critical point, the backward moving mode is neutral since it has zero

frequency in the inertial frame, in other words, the object is a Dedekind ellipsoid that has a stationary bar-like structure in inertial frame, yet maintains internal elliptical flows as viewed from the corotating frame of the star. When the star spins up further, the frequency of the backward moving wave becomes positive in the inertial frame yet always remains negative in the corotating frame. This means that this mode is moving forward as viewed by an inertial observer but it is still moving backward in the star's corotating frame, so it has positive angular momentum in the inertial frame and negative angular momentum in the corotating frame. Because it has positive angular momentum in the inertial frame, GR radiates away positive angular momentum and brings down the magnitude of the angular momentum in the inertial frame; but it has negative angular momentum in the corotating frame, so some positive angular momentum is radiated away from this originally negative quantity, and makes the angular momentum of the mode increasingly negative in the corotating frame (increasing in magnitude). Therefore, the mode actually grows in the corotating frame under the influence of GR. As the angular momentum of the mode is drained from the system, the frequency of the mode in the inertial frame drops. The final fate of such a star that is driven unstable by gravitational radiation was thought to be a Dedekind ellipsoid, as mentioned before.

In summary, the $l = |m| = 2$ f-mode is stable to GR in the nonrotating and slowly rotating cases, but as long as the critical limit is reached, i.e., the star's angular velocity is higher than some critical value, the backward going wave becomes unstable to GR. The critical limit is generally measured by $\beta \equiv |T/W|$, which can take a value ranging from 0 to 0.5 as the star spins up from a sphere to an infinitely thin disk (from M to T in Fig. 1.3). The faster the star rotates, the larger the β value. For Maclaurin spheroids, the critical value is around $\beta = 0.14$, as discussed in the introduction. Managan (1985), Imamura et. al. (1985), Ipser & Lindblom (1990), and Lai & Shapiro (1995) have all shown that this critical value for the $m = 2$ bar-mode does not depend sensitively on the equation of state or the angular momentum distribution inside the star. (However, Imamura et. al. (1995)

find that the critical value for the secular bar-mode is reduced to 0.093 in some extremely differential rotation cases.)

The above picture is based on linear perturbation theory. In the nonlinear regime, it is still unclear how the f-modes will grow and to what amplitude they would grow. Through the work presented in this dissertation, we will try to find answers to these questions.

2.3 The Role of Viscous Mechanisms

Aside from gravitational-radiation, fluid viscosity can also drive the secular bar-mode instability in sufficiently rapidly rotating stars. The end result of a secularly unstable star driven by viscosity is thought to be a Jacobi ellipsoid because viscosity tends to make the star rotate rigidly. It turns out that in weak gravitational fields the gravitational-radiation-driven secular instability and the viscosity-driven secular instability have the same critical limit. Hence, the Jacobi/Dedekind ellipsoid sequences both bifurcate from the Maclaurin spheroid at the same point, i.e., where $\beta \approx 0.14$ and one would expect both types of secular instabilities to set in at the same time, However, in fully relativistic stellar models these two secular instabilities have different critical limits (Stergioulas & Friedman, 1998).

Lindblom & Detweiler (1977) first showed that viscous processes within compact stars can act to compete with and consequently suppress the GRR-driven secular bar-mode instability. Because viscosity and gravitational-radiation destabilize different modes and the mode that is not unstable to one dissipation is stabilized by that dissipation, the net result of considering both dissipation mechanisms is that both effects tend to cancel with each other. The actual critical upper limit for a secularly stable Maclaurin spheroid, where the Jacobi/Dedekind sequences bifurcate from the Maclaurin spheroid sequence, goes beyond the traditional bifurcation point of $\beta = 0.14$ and depends on the ratio of the strengths of gravitational radiation and viscous forces. In some extreme cases, this critical limit for secular instability may reach to the point of the onset of dynamical instability, i.e., $\beta = 0.27$.

There are various physical viscosities that can act as dissipation mechanisms in neutron stars. Flowers & Itoh (1976) first considered shear viscosities due to electron and neutron scattering. Cutler & Lindblom (1987) studied the effect of electron-electron scattering in the superfluid state, in which the viscosity due to neutron-neutron scattering should effectively vanish. Kazanas & Schramm (1977) first emphasized that shear viscosity due to neutrino scattering needs to be taken into account while considering the damping time of nonradial pulsations in gravitational collapse, but Lindblom & Detweiler (1979) argued that neutrino radiation only provides damping for cores whose density $\leq 10^{13}\mathrm{g/cm}^3$, and for modes with higher l values. The effects of bulk viscosity due to weak nuclear interaction (Jones 1971; Sawyer 1989; Ipser & Lindblom 1991; Yoshida & Eriguchi 1995) and "mutual friction" effects in a superfluid (Lindblom & Mendell, 1995) have also been investigated. Ipser & Lindblom (1991) have shown that in neutron stars cooler than $T \approx 10^{6\sim7}K$, the shear viscosity is sufficiently large to completely suppress the gravitational-radiation driven instability. On the other hand, in neutron stars hotter than $T \approx 2\times10^{10}K$, the bulk viscosity is also sufficiently large to suppress this instability. Hence, only in the intermediate temperature region, this instability may occur, but only for stars that rotate faster than $90 \sim 95\%$ of their breakup angular speed, i.e. the speed at which equatorial masses will be ejected from the star by the centrifugal force.

In the present work, we will not be investigating the influence of viscous processes on the gravitational-radiation driven bar-mode instability, focusing instead on following the nonlinear development of the bar-mode in purely inviscid systems.

2.4 Contemporary Related Studies

As we have just reviewed, a considerable amount of work has been published utilizing linear perturbation techniques to analyze the stability of rotating stars and to identify situations of interest to the gravitational wave community. However, in order to study these instabilities in the nonlinear regime and accurately predict their importance to the

detection of gravitational waves, time-dependent nonlinear modelling is badly needed. Here we briefly review the limited amount of work in recent years that has begun to address these key issues.

2.4.1 Nonlinear Development of Dynamical Bar-Mode Instability

Over the past couple of decades, a number of groups have made use of full three-dimensional (3D) numerical hydrodynamic techniques to study the nonlinear development of the dynamical bar-mode instability in the context of the evolution of protostellar gas clouds (Tohline, Durisen, & McCollough 1985; Durisen et al. 1986; Williams & Tohline 1988; Pickett et. al. 1998; Cazes & Tohline 2000). In recent years, the detectability of gravitational wave signals coming from this dynamical bar-mode instability that arises in rapidly rotating neutron stars has also been investigated (New, Centrella, & Tohline 2000; Brown 2000; Liu 2001). All of these investigations have shown that the critical limit of the dynamical bar-mode instability $\beta \gtrsim 0.27$ is largely independent of the compressibility and rotational law inside the stars. However, a very recent investigation by New et. al. (2002) shows that the $m = 2$ bar-mode becomes dynamically unstable at β values significantly lower than this limit ($\beta \sim O(0.1)$) if the star is in highly differential rotation and, in some cases, even the $m = 1$ mode becomes dynamically unstable. Further investigation by Shibata et. al. (2003) has shown that the $m = 2$ bar-mode becomes dynamically unstable even for $\beta \sim O(0.01)$ in some extremely differentially rotating models. These newly found instabilities are leading researchers in this field to reconsider the criterion regarding the dynamical instability of the bar-mode in realistic stars.

2.4.2 Nonlinear Development of Secular R-Mode

In contrast to studies of the dynamical bar-mode instability, hydrodynamical modelling of the nonlinear development of secular instabilities remained unvisited until very recently.

Lindblom et. al. (2001, 2002) carried out the first full 3D numerical study on the nonlinear development of the secular r-mode instability that is driven by gravitational radiation in young neutron stars. Their work has shown that in the absence of any viscous force, the GRR-driven r-mode is able to grow to the nonlinear regime to the order of unity. At the late stage of their simulation, the r-mode underwent a catastrophic decay and died out. If the r-mode can grow to an amplitude of order unity in real neutron stars, it would be a very good and strong source of gravitational waves. However, the Cornell group (Schenk et al., 2002; Arras et al., 2003) has argued that the mode-mode coupling between r-mode and other high order modes is so strong that the r-mode will saturate by leaking energy to high order modes long before it can reach an amplitude of order unity, and therefore, the detectability of the r-mode is not as optimistic as previously expected.

Despite the fact that the dynamical bar-mode instability and the secular r-mode instability have gained much attention and have been extensively studied, to the author's knowledge, there is no work which utilizes the numerical techniques such as full 3D hydrodynamics to model the nonlinear development of the secular bar-mode instability in a fully self-consistent manner.

2.4.3 Quasi-Equilibrium Evolution of Secularly Driven Bar-mode Instability

Lai & Shapiro (1995) have made a comprehensive investigation on various gravitational wave signatures that may arise from the secular bar-mode instability in rotating nascent neutron stars. Three possible evolutionary mechanisms were investigated in detail by using energy and angular momentum conservation to construct sequences of quasi-equilibrium, ellipsoidal configurations in order to mimic evolutionary paths of rotating neutron stars in an inexpensive and simplified way. The detectability of corresponding gravitational-waves from such events were also estimated.

(1) The first mechanism happens in a secularly unstable but dynamically stable axisymmetric star ($0.14 \lesssim \beta \lesssim 0.27$), which is driven unstable by gravitational radiation. Under such a circumstance, a rotating star beginning from a Maclaurin spheroid configuration will evolve along the Dedekind-like ellipsoid sequence toward a Dedekind ellipsoid configuration. The gravitational waves emitted during this evolution have certain characteristics: the wave amplitude is small in the beginning because the star is nearly axisymmetric, but it will increase as the bar-mode instability develops; after reaching a peak value, it drops quickly because the frequency of the bar-mode decreases as angular momentum is radiated away, and because the gravitational radiation is proportional to the fifth power of this frequency; the amplitude will finally drop to zero when a Dedekind ellipsoid is formed, because a Dedekind ellipsoid is stationary in the inertial frame and does not emit gravitational waves at all. For a typical neutron star, the overall frequency starts from a few hundred Hz then steadily drops to zero. Although this evolution path has been believed for a long time as the mechanism that is capable of generating a Dedekind ellipsoid, its credibility is thought to be dubious by some investigators. For example, Lebovitz & Lifschitz (1996) argued that adjoint configurations (Dedekind-like ellipsoids) are susceptible to an "elliptic flow" instability on a dynamical time scale and therefore it is unlikely that real stars will settle down to the Dedekind ellipsoid configuration.

(2) The second mechanism involves an initially Jacobi-like ellipsoid, whose evolution is driven by gravitational radiation. Such a Jacobi-like ellipsoid will evolve to either a secularly stable Maclaurin spheroid or a secularly unstable Maclaurin spheroid, then further evolve to a Dedekind ellipsoid following the evolution path described by the first mechanism. This evolution will give birth to gravitational waves with increasingly high frequency, because as the angular momentum is radiated away, the moment of inertia of the system drops quickly, even faster than the loss of angular momentum. Although a uniformly rotating Jacobi ellipsoid can only exist in neutron stars with pretty stiff equations of state due to the mass shedding constraint (see Appendix B), a slightly differential rotation can inhibit

the mass shedding and help to form a more deformed Jacobi-like configuration, which will emit much more energy than a uniformly rotating configuration does.

(3) The third mechanism involves a Dedekind-like configuration but with a negative eigenfrequency for the mode, i.e., $\beta \lesssim 0.14$. In this case, gravitational radiation actually carries negative angular momentum, and the internal vorticity is responsible for the major contribution to the overall angular momentum of the system. In such a configuration, the gravitational radiation radiates away negative angular momentum, causing an increase of the angular momentum in the system; yet, the energy of the system continues to decrease. The wave frequency can be low, but its amplitude decreases monotonically. Such a configuration will evolve toward a Dedekind ellipsoid or a stable Maclaurin spheroid.

By constructing sequences of quasi-equilibrium, ellipsoidal configurations to represent approximate neutron star models along these various evolutionary paths, Lai & Shapiro were able to make a qualitative estimate of the gravitational wave forms and wave amplitudes for the above types of astrophysical scenarios.

2.4.4 This Dissertation Research

The work presented here is the first attempt to use state-of-the-art 3D hydrodynamical techniques to explore the nonlinear development of the secular bar-mode instability in rapidly rotating neutron stars. A 3D hydro code is used to integrate forward in time the coupled set of nonlinear partial differential equations that govern dynamical motions in nonrelativistic fluids, and the effects of GRR forces are handled by including a post-Newtonian radiation reaction force term in the equation of motion. We also examine the credibility of previous studies that have estimated the frequency and amplitude of gravitational waves that are generated by the GRR-driven secular bar-mode instability in rapidly rotating neutron stars.

3. Basic Equations and Numerical Techniques

3.1 Newtonian Hydrodynamics

Since individual stars are mostly isolated from their outside environment, their thermal and global properties change very slowly. Thus, generally speaking, it is reasonable to treat a star as a self-gravitating and adiabatic fluid that obeys the following equations: Poisson's Equation relating the star's Newtonian gravitational potential Φ_N to its mass distribution,

$$\nabla^2 \Phi_N = 4\pi G\rho; \tag{3.1}$$

Euler's Equation describing the motion of inviscid fluid elements,

$$\rho(\frac{\partial \vec{v}}{\partial t} + \vec{v} \cdot \vec{\nabla}\vec{v}) = -\vec{\nabla}p - \rho\vec{\nabla}\Phi_N; \tag{3.2}$$

the continuity equation expressing conservation of mass,

$$\frac{\partial \rho}{\partial t} + \vec{\nabla} \cdot (\rho\vec{v}) = 0; \tag{3.3}$$

and a polytropic equation of state relating the fluid's thermal properties,

$$p = (\Gamma - 1)\epsilon\rho, \tag{3.4}$$

if we consider our fluid system to be an ideal gas. In these equations, ρ is the mass density of each fluid element, $\vec{v}$ is the three-velocity field, p is the pressure, ϵ is the specific internal energy, Γ is the chosen adiabatic exponent.

The above equations are closed with an adiabatic form of the energy equation,

$$\frac{\partial \tau}{\partial t} + \nabla \cdot (\tau\vec{v}) = 0, \tag{3.5}$$

where $\tau \equiv (\epsilon\rho)^{1/\Gamma}$ is the entropy tracer,

Our simulations of rotating neutron stars largely involve solving the above set of partial differential equations (PDE) by numerical techniques such as finite difference. Our philosophy is to build stellar models that are initially in equilibrium and then use the above equations to evolve each system. Since our systems are mostly rotationally flattened, it is natural to adopt the cylindrical coordinate system as our basic frame. In all the work presented here, we will concentrate on solutions to these equations on a cylindrical coordinate grid. Our hydrocode has adopted a set of dimensionless units, in which the gravitational constant G and the maximum density $\rho_{\max}$ of the initial model have been set to 1. In addition, the maximum radius of our cylindrical grid, $\varpi_{\rm grid}$, has also been set to 1. Therefore, every physical quantity in our simulations has been normalized to the hydrocode units so that $G = \rho_{\max} = \varpi_{\rm grid} = 1$. In order to get any quantity in real units, one has to take into account the conversion from the hydrocode units to real units.

3.2 Initial Model, Equation of State and Self-Consistent-Fluid Technique

Although our ultimate goal is to study the secular bar-mode instability in rapidly rotating neutron stars, it is nontrivial to obtain an accurate and realistic solution to such a problem because of the presence of many complicated physical phenomena assiciated with ultra relativistic motions, extreme compact matter, and very strong magnetic fields. In our first attempt to explore this problem, we decided to adopt a simple polytropic equation of state (EOS) for our neutron star models:

$$p = K\rho^{1+\frac{1}{n}} = K\rho^{\Gamma}, \tag{3.6}$$

where n is the polytropic index that determines the compressibility of the fluid(the higher the value of n, the more compressible the fluid), and K is the polytropic constant. On the other hand, we also chose to study initial polytropic models that are rotating uniformly

because the analytical solutions of some of such systems have been known for a long time, hence, we were able to compare our results with analytical predictions.

We have made use of Hachisu's self-consistent-field (Hachisu 1986, hereafter HSCF) technique to build these initial models that are either spherical (nonrotating) or axisymmetric (uniformly rotating). We start from a system that obeys the following assumptions: (A) The fluid is in axisymmetric rotation around the rotation axis; (B) The angular velocity is constant everywhere, hence, the fluid velocity $\vec{v}$ takes the form of $\vec{v} = \hat{e_\phi}\varpi\Omega$, where Ω is the spin angular velocity of the star; (C) The system is in hydrostatic equilibrium; and (D) The fluid obeys polytropic equation of state, i.e. the pressure p and density ρ are related by equation (3.6). For such a system, its internal structure is determined by the following integral form of the equation of hydrostatic equilibrium, which is derived from equation (3.2) for steady-state axisymmetric flows:

$$H + \Phi_N + \Psi = \text{const} = C, \tag{3.7}$$

where the fluid enthalpy H is defined from $dH = dp/\rho$, and Ψ is the centrifugal potential and determines the angular momentum distribution within the system. For a uniformly rotating system, Ψ has the following form,

$$\Psi = \frac{1}{2}\Omega^2\varpi^2. \tag{3.8}$$

The Newtonian gravitational potential Φ_N is determined by the mass distribution through Poisson's equation (3.1).

As discussed by Hachisu (1986), the self-consistent-field technique utilizes an iterative scheme to obtain the equilibrium configuration of a rotating and self-gravitating star. It starts from a trial mass distribution $\rho(\varpi, z)_{\text{trial}}$, calculates the corresponding gravitational potential field; then takes into account proper boundary conditions on H and Ψ, e.g. H must vanish at the surface of the star; uses equation (3.7) to calculate the constant C at the boundary of the star and hence yields the enthalpy H everywhere else; then recomputes

a new mass distribution $\rho(\varpi, z)_{\rm new}$ by the following relationship of polytropic gas systems,

$$H = (1+n)K\rho^{\frac{1}{n}}. \tag{3.9}$$

The whole iteration is stopped when the old and new mass distributions converge and the errors between old and new parameters fall within some specific control tolerance. Specifically, if the fractional changes in C and Ω between two successive iteration steps are less than a chosen threshold, which in our current computation is set to 10^{-4}, the model is considered to be converged. In order to measure if the system is in hydrostatic equilibrium, we also compute the so-called Virial error VE defined as:

$$VE \equiv (2T + 3\int pdV)/|W|. \tag{3.10}$$

According to the virial theorem, VE should take the value of 1.0 for equilibrium systems. Our calculation of VE agrees with this very well; the typical error is of order 10^{-4}.

3.3 Gravitational Radiation Reaction (GRR) Force

In order to study the effect of gravitational radiation on the secular bar-mode instability, we need to add some relativistic correction to the above equations, because a pure Newtonian system will not emit gravitational radiation. Thorne (1969) studied the non-radial pulsation of relativistic stellar models in the weak field limit. He derived the post-Newtonian corrections to the Newtonian gravitational field due to relativistic effects. Specifically, the total gravitational potential can be written as

$$\Phi = \Phi_N + \kappa\Phi_{GR}, \tag{3.11}$$

where Φ_{GR} is the gravitational radiation correction due to relativistic effects. For modelling purposes, a dimensionless coefficient κ has been affixed to the radiation-reaction potential term. By adjusting the value of κ, we can readily turn off the effect of non-Newtonian

forcing or artificially enhance the effect. The gravitational radiation correction takes the form of

$$\Phi_{GR} = -\sum_{l=2}^{\infty}\sum_{m=-l}^{l}(-1)^l N_l r^l Y_{lm}\frac{d^{2l+1}D_{lm}}{dt^{2l+1}}, \tag{3.12}$$

where Y_{lm} is the spherical harmonics function, r is the spherical radius, the associated mass multipoles are,

$$D_{lm} \equiv \int \rho r^l Y^*_{lm} d^3x\,, \tag{3.13}$$

and the leading coefficient,

$$N_l \equiv \frac{4\pi G}{c^{2l+1}}\frac{(l+1)(l+2)}{l(l-1)[(2l+1)!!]^2}\,, \tag{3.14}$$

where c is the speed of light.

According to the above expression for Φ_{GR}, the leading order term is the $l = m = 2$ quadrupole term, because higher order terms go as $1/c^{2l+1}$ and are relatively small in general. On the other hand, we are only interested in the secular bar-mode, which is driven by the quadrupole radiation. Thus, we only keep the quadrupole term in the current context and omit all the higher order terms. With this in mind, the expression for Φ_{GR} used in our simulations is,

$$\Phi_{GR} = -N_2 r^2 Y_{22}\frac{d^5 D_{22}}{dt^5} = -N_2 r^2 Y_{22} D^{(5)}_{22} \tag{3.15}$$

$$= -N_2 r^2\sqrt{\frac{15}{32\pi}}e^{2i\phi}\sin^2\theta D^{(5)}_{22} \tag{3.16}$$

$$= -N_2 \varpi^2\sqrt{\frac{15}{32\pi}}e^{2i\phi} D^{(5)}_{22}\,, \tag{3.17}$$

where ϖ is the cylindrical radius, ϕ is the azimuthal angle, $N_2 = 8\pi G/(75c^5)$, and the superscript (5) indicates that Φ_{GR} depends on the fifth time-derivative of the mass quadrupole moment D_{22}. Therefore, the radiation-reaction potential, hence the strength of GRR forces is proportional to the fifth time derivative of the quadrupole moment of the system. Following Lindblom et. al. (2001, 2002), we assume that the time dependence of D_{22} is exactly

sinusoidal - which is true if we have a pure eigenmode - so that the time derivatives are easily handled as follows:

$$D_{22}^{(n)} \approx (i\omega_{22})^n D_{22}, \tag{3.18}$$

where ω_{22} is the angular eigenfrequency of the $l = m = 2$ f-mode. As we see from this expression, the fifth time derivative of the quadrupole moment, and therefore the radiation reaction potential, is proportional to the eigenfrequency raised to the fifth power. Hence a small change in the eigenfrequency can significantly affect the radiation reaction potential and, consequently, the growth or decay rate of the $l = m = 2$ f-mode. (This is what happens in our forthcoming rotating model simulations: Because our models are just beyond the critical limit, the eigenfrequency is very close to zero so we have to introduce a large pre-factor κ in equation (3.11) in order to permit the mode to grow out of the various noises in a reasonable amount of time.)

As shown by Finn & Evans (1990), we can express dD_{22}/dt as an integral over the standard fluid variables as follows.

$$\begin{aligned} D_{22}^{(1)} &= \frac{dD_{22}}{dt} = \frac{d}{dt}\int \rho r^2 Y_{22}^* d^3x \\ &= -\int \nabla\cdot(\rho\vec{v}) r^2 Y_{22}^* d^3x \\ &= -\int \nabla\cdot(\rho\vec{v} r^2 Y_{22}^*) d^3x + \int \rho\vec{v}\cdot\nabla(r^2 Y_{22}^*) d^3x \\ &= -\int \rho r^2 Y_{22}^* \vec{v}\cdot d\vec{s} + \int \rho\vec{v}\cdot\nabla(r^2 Y_{22}^*) d^3x \\ &= \sqrt{\frac{15}{8\pi}}\int \rho\varpi e^{-2i\phi}(v_\varpi - i v_\phi) d^3x\,. \end{aligned} \tag{3.19}$$

In the above, we have discarded the surface integral, assuming the mass density ρ drops to zero at the surface of our control volume. Given dD_{22}/dt and D_{22}, we easily obtain,

$$|\omega_{22}| \approx \frac{1}{|D_{22}|}\left|\frac{dD_{22}}{dt}\right|, \tag{3.20}$$

thus, the fifth time-derivative of the mass quadrupole moment becomes

$$D_{22}^{(5)} = \omega_{22}^4 D_{22}^{(1)}. \tag{3.21}$$

3.4 Numerical Schemes of Hydrodynamics

For our numerical simulations, we cast equation (3.2) into a rotating cylindrical coordinate system, and replace Φ_N by Φ as given in equation (3.11), then obtain the following equations of motion as the basic evolution equations of our fluid system:

$$\frac{\partial S}{\partial t} + \nabla \cdot (S\vec{v}) = -\frac{\partial p}{\partial \varpi} - \rho\frac{\partial \Phi}{\partial \varpi} + \frac{A^2}{\rho\varpi^3} + \rho\Omega_f^2\varpi + \frac{2\Omega_f A}{\varpi}, \tag{3.22}$$

$$\frac{\partial T}{\partial t} + \nabla \cdot (T\vec{v}) = -\frac{\partial p}{\partial z} - \rho\frac{\partial \Phi}{\partial z}, \tag{3.23}$$

$$\frac{\partial A}{\partial t} + \nabla \cdot (A\vec{v}) = -\frac{\partial p}{\partial \phi} - \rho\frac{\partial \Phi}{\partial \phi} - 2\Omega_f\varpi S, \tag{3.24}$$

where Ω_f is the angular velocity of the rotating frame, $S \equiv \rho u$, $T \equiv \rho w$, and $A \equiv \rho\varpi v_\phi$ are the radial, vertical, and angular momentum densities, respectively (and u, w, and v_ϕ are the radial, vertical and azimuthal components of the velocity, respectively). The $A^2/\rho\varpi^3$ term in the radial equation of motion is the curvature term that arises naturally in a cylindrical coordinate system; the $\rho\Omega_f^2\varpi$ term is due to the centrifugal force; the $2\Omega_f A/\varpi$ and $2\Omega_f\varpi S$ result from the Coriolis force.

As implemented on our cylindrical computational mesh (ϖ, ϕ, z), D_{22} and its first time-derivative take the following forms,

$$D_{22} = \sqrt{\frac{15}{32\pi}} \int \rho\varpi^2(\cos 2\phi - i \sin 2\phi) d^3x\,, \tag{3.25}$$

$$D_{22}^{(1)} = \sqrt{\frac{15}{8\pi}} \int \rho\varpi[v_\varpi \cos 2\phi - v_\phi \sin 2\phi - i(v_\phi \cos 2\phi + v_\varpi \sin 2\phi)] d^3x \quad . \tag{3.26}$$

We use an explicit finite-differencing scheme that is second-order accurate in both time and space to self-consistently integrate all the above equations forward in time. The details of our hydrocode are discussed in Motl, Tohline, & Frank (2002). Here, we give a brief description.

We have chosen S, T, A, ρ, and τ as our primary evolutionary variables. The equations governing their time evolution — equations (3.1), (3.3), (3.4), (3.22), (3.23), (3.24) — have a common conservative form; that is, all of them have a divergence term on the left-hand-side of the equation and a right-hand-side that is either nonzero or zero. This characteristic form allows us to write only one numerical scheme, but to solve all these equations in a similar fashion. Accordingly, our numerical scheme of solving such an equation can be divided into two steps: an advection step, which uses a volume integral method to convert the divergence term to a finite volume form; and a source step, which handles the right-hand-side terms that will act as a source term for any conserved quantity. The Van leer upwind linear interpolation technique is implemented in the advection step in order to calculate the flux at the surfaces of each grid cell. Artificial viscosity is introduced to handle shocks that may form during the evolution. The integration timestep is limited by the famous Courant condition. The Poisson equation is solved every integration timestep using a method developed by Cohl & Tohline (1999), which uses the half-integer degree Legendre functions of the 2^{nd} kind to solve for the boundary conditions on the cylindrical grid, and the alternating-direction implicit (ADI) method to solve for the potential throughout the internal volume of the grid.

4. Selected Models and Analysis Techniques

4.1 Initial Equilibrium Models

In this initial effort to study the effect that GRR forces have on the behavior of the $\ell = |m| = 2$ f-mode in compact stellar objects, we have decided to construct initial equilibrium configurations with a polytropic index $n = 1/2$ (and adiabatic exponent $\Gamma = 1 + 1/n = 3$) that fairly represents the stiff equation of state of neutron stars. We have also decided to restrict our investigation to initial equilibrium models that either are nonrotating (initially spherically symmetric) or are uniformly rotating (initially axisymmetric). Equilibrium structures of this type are easy to numerically construct using the HSCF technique as discussed in Chapter 3 and, from previous linear stability analyses (Ipser & Lindblom 1990), we have been able to gain some quantitative insight regarding how the $\ell = |m| = 2$ f-mode is likely to behave in such models. As mentioned earlier, for example, we expect that this so-called "barmode" will not be unstable unless the initial axisymmetric model exhibits a ratio of rotational to gravitational potential energy $\beta \equiv T/|W| \geq \beta_{\rm crit} \approx 0.14$. Indeed, in more slowly rotating models, the amplitude of this barmode is expected to damp in the presence of GRR forces. We also know from previous work that it is possible to construct uniformly rotating, $n = 1/2$ polytropes that have rotational energies above this threshold value. (When $n > 0.808$, it is not possible to construct uniformly rotating, axisymmetric polytropes with $\beta > 0.14$ because centrifugal forces would exceed gravity in the equatorial plane of such models and cause mass shedding out from the equator; see James 1964 and Appendix B for further discussion.)

More specifically, we have chosen to follow the evolution of the $\ell = |m| = 2$ f-mode in models that initially have four different rotational energies: $\beta = 0.0, 0.157$, 0.179, and 0.181. These initial models will generally be referred to, respectively, as "SPH," "ROT157,", "ROT179", and "ROT181;" details regarding the properties of these initial models are given

in Tables 4.1, 4.2, 4.3 and 4.4. Among the parameters that are itemized in column 1 of these tables but that have not already been defined, M is the total mass of the model; $r_{\rm eq}$ and $r_{\rm polar}$ are its equatorial and polar radii; $\bar{\rho}$ and $\rho_{\rm max}$ are its mean and maximum (central) densities; and $\Omega_0 \equiv \sqrt{\pi G \bar{\rho}_0}$ is the characteristic dynamical frequency of the model. (Following the convention adopted by Ipser & Lindblom 1990, 1991, for models ROT157, ROT179, and ROT181 we define Ω_0 in terms of the mean density $\bar{\rho}_0$ of a *spherical* polytrope that has the same values of n, K, and M.) Column 2 of Table 4.1 gives the parameter values for model SPH in the dimensionless units traditionally adopted for a spherical polytrope whose structure is derived through a solution of the Lane-Emden equation (based on $G = K = \rho_{\rm max} = 1$; *cf.*, Chandrasekhar 1953). Column 3 of Table 4.1, and column 2 of Tables 4.2, 4.3, and 4.4 give the parameter values that we derived from the initial models that we constructed numerically using the HSCF technique and the dimensionless units that have been adopted in our hydrocode (based on $G = \rho_{\rm max} = r_{\rm grid} = 1$; see Appendix A for further discussion). Finally, column 4 of Table 4.1 and column 3 of Tables 4.2, 4.3, and 4.4 give the parameter values in dimensional units, assuming the $n = 1/2$ polytrope is a neutron star of mass 1.4 $M_\odot$ with a polytropic constant $K = 1.83 \times 10^{-10}{\rm cm}^8\ {\rm g}^{-2}\ {\rm s}^{-2}$, which in model SPH gives the star a radius of 12.5 km.

Table 4.1 also contains numerical values for two characteristic velocities: $K^{1/2}\rho_{\rm max}$ is a measure of the central sound speed, assuming the pressure is generated by thermal motions; and $r_{\rm eq}\Omega_{\rm o}$ is a measure of the free-fall velocity at the surface of the star. In the fourth column of Table 4.1, these two velocities are expressed as fractions of the speed of light, c. By equating either of these velocities with their dimensionless counterparts in column 3, we conclude that, for model SPH, the speed of light in hydrocode units is $c_{\rm code} = 3.122$. Analogously, for models ROT157, ROT179, and ROT181 the speed of light in hydrocode units has been calculated from the central sound speed and recorded in column 2 of Tables 4.2, 4.3, and 4.4. Finally, for the three rotating models, Tables 4.2 through 4.4 each contain

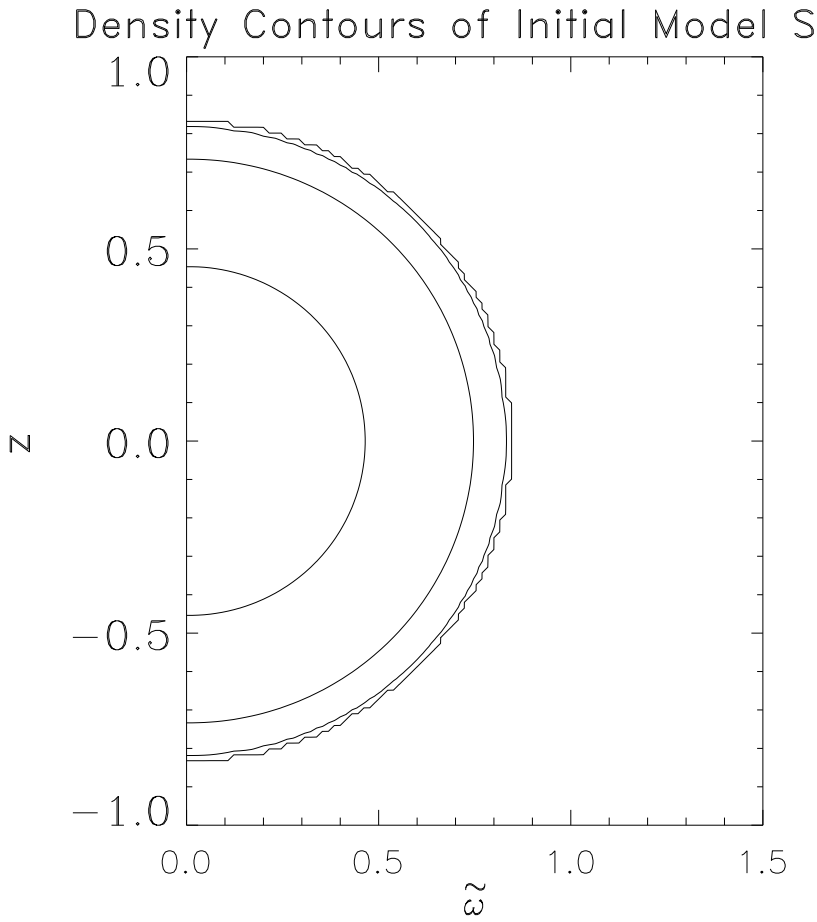

Figure 4.1: Iso-density contours of model SPH in the meridional plane. The vertical axis is the Z axis, the horizontal axis is the cylindrical radial axis. The four contours correspond to density levels of 0.8 (innermost contour), 0.4, 0.1, and 0.001 (outermost contour). The maximum density value is 1.0.

values of the angular velocity of the star $\Omega_{\rm rot}$, the star's total angular momentum $J_{\rm total}$, the dimensionless ratio of $\Omega_{\rm rot}$ to the dynamical frequency Ω_0, and β.

Figures 4.1 and 4.2 show iso-density contours in the meridional plane of models SPH and ROT181, respectively. It is very clear that as the β value increases, the star spins up and hence becomes more rotationally flattened.

For the spherical initial model, SPH, we know fairly accurately from linear stability analyses what the spatial structure and the time-varying behavior of the $\ell = |m| = 2$ f-mode should be. It therefore provides an important test case and benchmark for our nonlinear

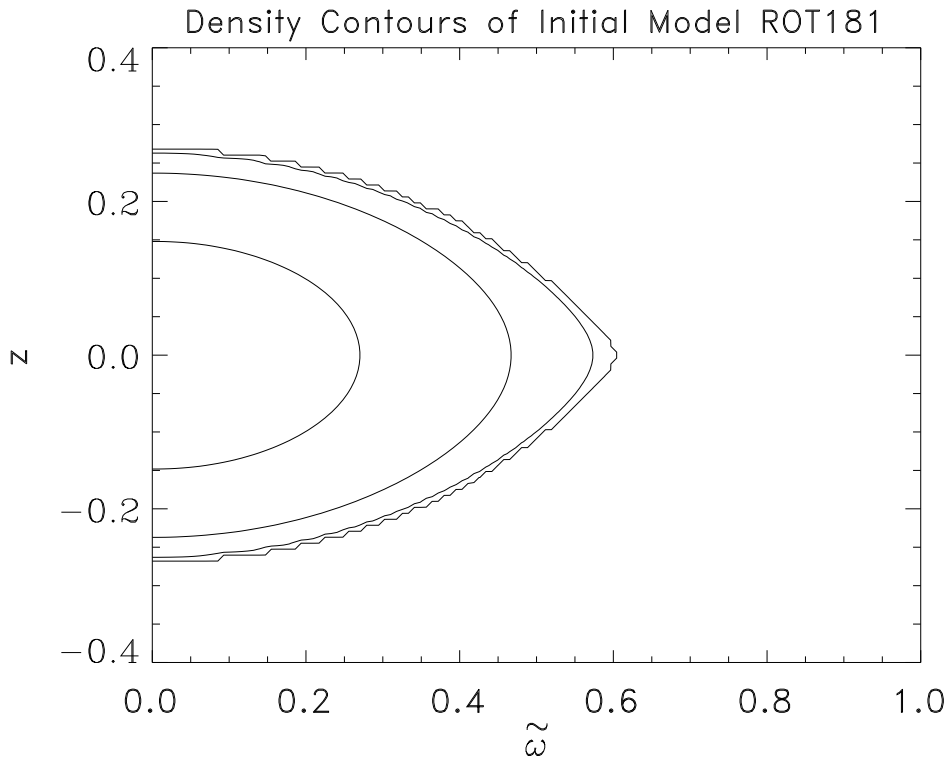

Figure 4.2: Iso-density contours of model ROT181 in the meridional plane. The vertical axis is the Z axis, the horizontal axis is the cylindrical radial axis. The four contours correspond to density levels of 0.8 (innermost contour), 0.4, 0.1, and 0.001 (outermost contour). The maximum density value is 1.0. The star is visibly flattened due to rotation.

Table 4.1: Parameters for Model SPH (spherical, $n = 1/2$ polytrope)

Parameter	Polytrope	Hydrocode	Neutron Star
M	1.963	1.359	1.4 $M_\odot$
G	1.0	1.0	6.67×10^{-8}cm^{3}g^{-1}s^{-2}
K	1.0	0.7825	1.83×10^{-10}cm^8 g^{-2} s^{-2}
$r_{\rm eq}$	0.9511	0.8413	12.5 km
$\bar{\rho}$	0.5446	0.5460	3.42×10^{14} g cm^{-3}
$\rho_{\rm max}$	1.0	1.0	6.26×10^{14} g cm^{-3}
$\Omega_{\rm o}$	1.308	1.309	8.47×10^{3} s^{-1}
$\mathrm{K}^{1/2}\rho_{\rm max}$	1.0	0.8846	0.2833 c
$r_{\rm eq}\Omega_{\rm o}$	1.244	1.102	0.3527 c
c	3.527	3.122	3.0×10^{10} cm s^{-1}

evolutionary simulations. Models ROT157, ROT179 and ROT181 have rotational energies that lie above the critical threshold that is required (by linear analysis) for instability, but below the termination point ($\beta = 0.185$; see Hachisu 1986) of the uniformly rotating, $n = 1/2$ sequence.

Table 4.2: Parameters for Model ROT157

Parameter	Hydrocode	Neutron Star
M	0.09929	1.4 $M_\odot$
G	1.0	6.67×10^{-8}cm^{3}g^{-1}s^{-2}
K	0.09504	1.83×10^{-10}cm^8 g^{-2} s^{-2}
$r_{\rm eq}$	0.4527	17.30 km
$r_{\rm polar}$	0.2414	9.23 km
$\bar{\rho}$	0.5107	2.58×10^{14} g cm^{-3}
$\rho_{\rm max}$	1.0	5.05×10^{14} g cm^{-3}
Ω_0	1.459	8.47×10^{3} s^{-1}
$K^{1/2}\rho_{\rm max}$	0.3083	0.2279c
c	1.353	3.0×10^{10} cm s^{-1}
$\Omega_{\rm rot}$	0.9507	5.67×10^{3} s^{-1}
$\Omega_{\rm rot}/\Omega_0$	0.6516	0.6516
β	0.157	0.157
$J_{\rm total}$	0.005904	1.45×10^{49} g cm^2 s^{-1}

Table 4.3: Parameters for Model ROT179

Parameter	Hydrocode	Neutron Star
M	0.1750	1.4 $M_\odot$
G	1.0	6.67×10^{-8}cm^{3}g^{-1}s^{-2}
K	0.1302	1.83×10^{-10}cm^8 g^{-2} s^{-2}
$r_{\rm eq}$	0.5952	19.21 km
$r_{\rm polar}$	0.2619	8.45 km
$\bar{\rho}$	0.4935	2.38×10^{14} g cm^{-3}
$\rho_{\rm max}$	1.0	4.84×10^{14} g cm^{-3}
Ω_0	1.487	8.46×10^3 s^{-1}
$K^{1/2}\rho_{\rm max}$	0.3608	$0.2193c$
c	1.645	3.0×10^{10} cm s^{-1}
$\Omega_{\rm rot}$	0.9705	5.52×10^3 s^{-1}
$\Omega_{\rm rot}/\Omega_0$	0.6527	0.6527
β	0.179	0.179
$J_{\rm total}$	0.01678	1.104×10^{49} g cm^2 s^{-1}

4.2 Analysis of Nonaxisymmetric Structure

At the start of each of our nonlinear simulations, we fed one of the four initial models (SPH, ROT157, ROT179, or ROT181) into our hydrocode, then added to the model's initially axisymmetric structure a low-amplitude, nonaxisymmetric perturbation that was intended to fairly represent the structure of the $\ell = |m| = 2$ f-mode. For model SPH, for example, we introduced perturbations in the gas density $\delta\rho$ and in each of the three components of the gas velocity δv^a of the forms,

$$\delta\rho(\varpi, \phi, z) = \delta\rho_0(\varpi, z)e^{2i\phi}\,, \tag{4.1}$$

$$\delta v^a(\varpi, \phi, z) = \delta v^a_0(\varpi, z)e^{2i\phi}\,, \tag{4.2}$$

where the meridional plane structure of the perturbations $\delta\rho_0(\varpi, z)$ and $\delta v^a_0(\varpi, z)$ were prescribed by eqs. (24) and (25) of Ipser & Lindblom (1991). (See Appendix C for detailed expressions.) Figure 4.4 displays the spatial structure of $\delta\vec{v}(\varpi, \phi)$ in the equatorial plane ($z = 0$) of model SPH, and Figure 4.3 shows $\delta\rho$ as a function of ϖ along the positive Y axis. After this nonaxisymmetric perturbation was introduced into each initial model, the

Table 4.4: Parameters for Model ROT181

Parameter	Hydrocode	Neutron Star
M	0.1716	1.4 $M_\odot$
G	1.0	6.67×10^{-8}cm^{3}g^{-1}s^{-2}
K	0.1281	1.83×10^{-10}cm^8 g^{-2} s^{-2}
$r_{\rm eq}$	0.6102	19.69 km
$r_{\rm polar}$	0.2746	8.86 km
$\bar{\rho}$	0.4922	2.39×10^{14} g cm^{-3}
$\rho_{\rm max}$	1.0	4.85×10^{14} g cm^{-3}
Ω_0	1.488	8.47×10^3 s^{-1}
$K^{1/2}\rho_{\rm max}$	0.3579	$0.2190c$
c	1.634	3.0×10^{10} cm s^{-1}
$\Omega_{\rm rot}$	0.9705	5.52×10^3 s^{-1}
$\Omega_{\rm rot}/\Omega_0$	0.6522	0.6522
β	0.181	0.181
$J_{\rm total}$	0.01632	1.58×10^{49} g cm^2 s^{-1}

behavior of the model was determined entirely by the time-integration of the coupled set of evolutionary equations given above in §3.

Although each of our simulations permit us to follow in detail the time-dependent behavior of many different local as well as global physical variables, we have found it most useful to focus our attention on the behavior of the mass-quadrupole moment D_{22}. As long as we are following the evolution of a single mass-quadrupole eigenmode and D_{22} remains "small", we expect that its time-dependent behavior will be described approximately by the expression,

$$D_{22}(t) = D_0 e^{i\omega_{22}t}\,, \tag{4.3}$$

where in general ω_{22} is an imaginary number,

$$\omega_{22} = \omega_r + i\omega_i\,, \tag{4.4}$$

that contains information about both the azimuthal oscillatory frequency of the mode (ω_r) and the rate at which the amplitude of the mode damps ($\omega_i > 0$) or grows ($\omega_i < 0$) with

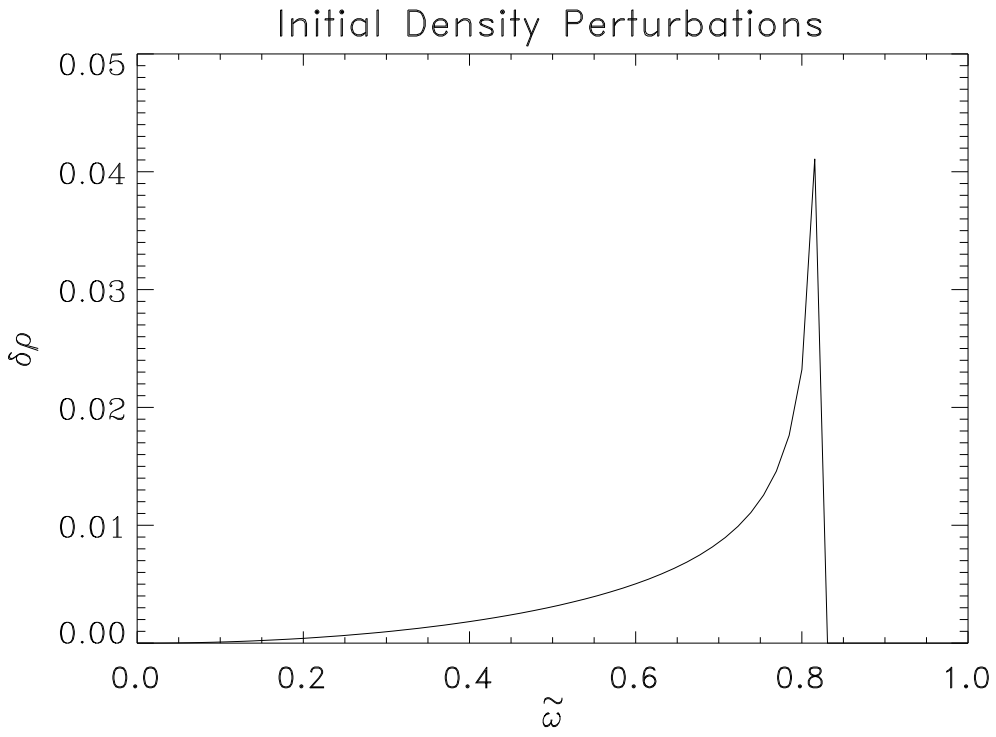

Figure 4.3: The initial density perturbation $\delta\rho$ as a function of ϖ along the positive Y axis of model SPH. It starts from zero at the center of the star, then reaches its maximum at the surface, and finally drops to zero outside the star. The density values are normalized so that the maximum density of the neutron star is 1.0.

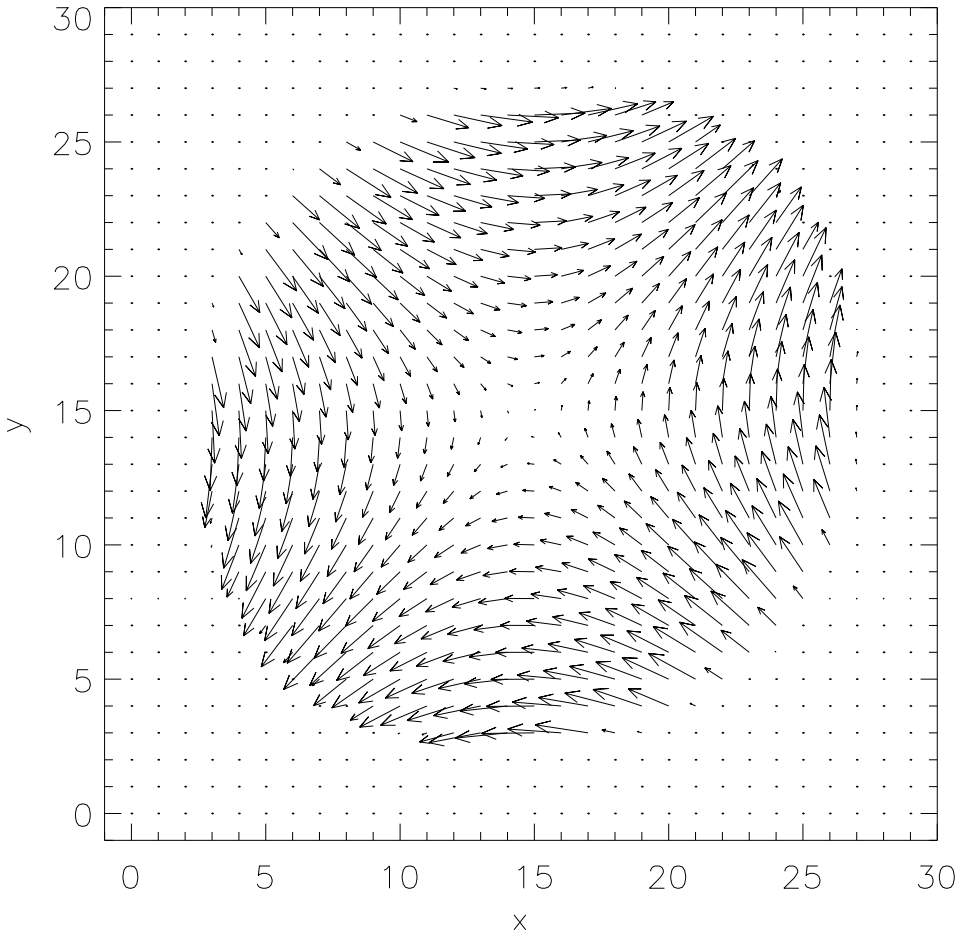

Figure 4.4: The equatorial velocity field of the velocity perturbation that was applied to the initial SPH model.

time. Also, under these conditions, the first time derivative of D_{22} is,

$$D_{22}^{(1)} = i\omega_{22} D_{22} \,. \tag{4.5}$$

By making judicious plots of D_{22} or $\ln(D_{22})$ as a function of time and/or by calculating the ratio of $D_{22}^{(1)}$ to D_{22}, we are able to measure both the real and imaginary parts of the barmode eigenfrequency that characterizes each of our models.

4.3 Previously Published Predictions from Linear Theory

Ipser & Lindblom (1990, 1991) have performed detailed analyses of the properties of the $\ell = |m| = 2$ f-mode in nonrotating polytropic stars having a range of polytropic indices. Table 4.5 summarizes the results of these analyses that are most relevant to our present investigation. For each value of the polytropic index shown in column 1 of Table 4.5, column 2 identifies the radius R and column 3 gives the dynamical frequency Ω_0 of a spherical, $1.5 M_\odot$ "neutron star" with the specified polytropic index and a central temperature of 10^9 K; column 4 lists Ipser & Lindblom's (1990) numerically determined value of the "pulsation frequency" $\omega_r = \mathrm{Re}(\omega_{22})$ in the corresponding spherically symmetric polytrope; and column 5 lists Ipser & Lindblom's (1991) numerically determined value of $\omega_i = \mathrm{Im}(\omega_{22}) = 1/\tau_{\mathrm{GR}}$, where τ_{GR} is the predicted "damping time" for this barmode in the specified spherical neutron star model.

Ipser & Lindblom (1990) also evaluated how the barmode frequency ω_r varies as a function of rotation frequency Ω_{rot} in uniformly rotating polytropes (see their Fig. 2). For $n = 0$ and $n = 3/4$ polytropes, they were able to determine at what critical rotation frequency Ω_{crit} the barmode becomes marginally unstable in the presence of dissipative forces. More precisely, they defined Ω_{crit} to be the rotation rate at which, as measured in a frame rotating with the same angular velocity as the star, the "pulsation frequency" $|\omega_r| = 2\Omega_{\mathrm{rot}}$ and, hence, the "backward moving" mode ($\omega_r < 0$) becomes stationary as

viewed from an inertial frame of reference. Their calculated values of $\Omega_{\rm crit}$ and associated values of $\beta_{\rm crit}$ are listed in columns 6 and 7, respectively, of Table 4.5.

Unfortunately, in their two key papers, Ipser and Lindblom did not include an analysis of $n = 1/2$ polytropic stars, so we cannot directly compare the results of our nonlinear simulations with their published predictions. With Lindblom's (2004) assistance, we have been able to use their analysis tools to extend the predictions displayed in Table 4.5 to the case we are investigating, however. The results are presented in Table 4.6. In this table, the uncertainties quoted for the predicted values of ω_r and ω_i come from an analysis of the spherical, $n = 1/2$ polytrope at five different radial grid resolutions (varying from 1250 to 10,000 grid zones).

We note that the dimensionless values of the barmode "pulsation frequencies" ω_r/Ω_0, critical rotation frequencies $\Omega_{\rm crit}/\Omega_0$, and critical β that are listed in Tables 4.5 and 4.6 do not depend on our introduction of $\Phi_{\rm GR}$ into the dynamical equations; they reflect only the Newtonian self-gravitating character of the models and are independent of the specified mass and radius. However, ω_i/Ω_0 is nonzero only because we have introduced a dissipative, radiation-reaction force into the equation of motion, and the values reported in Table 4.5 and 4.6 in each case depend on the choice of the neutron star mass and radius.

The values of ω_i/Ω_0 listed in Tables 4.5 and 4.6 are only appropriate for comparison with our nonlinear model simulations if the dimensionless coefficient κ that we have introduced into the equation of motion 3.2 is $\kappa = 1$. Because $\tau_{\rm GR}$ is inversely proportional to the magnitude of the radiation-reaction potential $\Phi_{\rm GR}$ (*cf.*, eq. (23) of Ipser & Lindblom 1991), however, we should expect the imaginary component of the barmode eigenfrequency to increase (and $\tau_{\rm GR}$ to decrease) in direct proportion to our selected value of κ.

From the data provided in Table 4.6 we should expect that the amplitude of the barmode will damp in model SPH exponentially on a time scale $\tau_{\rm GR} \equiv 1/|\omega_{\rm i}| = 192.3\kappa^{-1}\tau_{\rm pattern}$, where $\tau_{\rm pattern} \equiv 2\pi/|\omega_{\rm r}| = 3.97$ in dimensionless code units.

Table 4.5: Parameters Published by Ipser & Lindblom for $1.5 M_\odot$ Neutron Stars

Index	R (km)	Ω_0 (s^{-1})	$\lvert\omega_r\rvert/\Omega_0$	ω_i/Ω_0	$\Omega_{\rm crit}/\Omega_0$	$\beta_{\rm crit}$
0	17.171	5431	1.033	3.52×10^{-4}	0.612	0.1375
3/4	14.245	7188	1.292	1.84×10^{-3}	0.644	0.1298
1	12.533	8709	1.415	4.12×10^{-3}	...	...
5/4	9.822	12554	1.543	1.18×10^{-2}	...	...

Table 4.6: Predictions from Linear Theory for Model SPH

Index	R (km)	Ω_0 (s^{-1})	$\lvert\omega_r\rvert/\Omega_0$	ω_i/Ω_0
1/2	12.5	8470	1.188 ± 0.032	$9.53 \pm 0.56 \times 10^{-4}$

Linear perturbation analyses have not yet provided quantitative values of the bar-mode eigenfrequency in rapidly rotating, $n = 1/2$ polytropes. From the information given in Ipser & Lindblom (1990, 1991), however, we expect that in models ROT157, ROT179, and ROT181, (a) $\omega_{\rm r}/\Omega_0$ should be positive but close to zero, as viewed from an inertial reference frame because the models all have values of β just past the critical limit; and (b) $\omega_{\rm i}/\Omega_0$ should be slightly positive – that is, the mass-quadrupole moment should *grow* exponentially, but on a time scale that is very long compared to the *damping* time predicted for the nonrotating model, SPH. More specifically, if $|\omega_{\rm r}|/\Omega_0$ proves to be an order of magnitude smaller in the rotating models than it is in model SPH, we should expect $\tau_{\rm GR}$ to be $\sim 10^5$ times larger because the amplitude of the GRR driving term in Eq. (3.11) is proportional to ω_{22}^5.

Table 4.7: Predicted Decay Time Scale for Model SPH

N_r	ω_{22}/Ω_0	$\tau_{GR}\Omega_0$	$\tau_{GR}/\tau_{pattern}$
1250	1.156	1115	205.1
2500	1.172	1079	201.3
3000	1.175	1073	200.7
5000	1.168	1031	191.7
10000	1.219	991	192.3

5. Evolutions of Model SPH

To test if we have introduced the radiation-reaction potential correctly into our hydrocode, we performed a test run on the SPH model for which the stability properties are well-understood from linear analysis. Specifically, from the information presented in Table 4.6, we expect the $\ell = |m| = 2$ f-mode to exhibit an azimuthal oscillation frequency of $|\mathrm{Re}(\omega_{22})| = |\omega_r| = 1.188 \pm 0.032\ \Omega_{\rm o}$, as viewed from an inertial reference frame, and to damp exponentially on a timescale $\tau_{\rm GR} = 1/\omega_i = 991 \pm 62\ [\kappa\Omega_{\rm o}^{-1}]$. These are the two key quantitative predictions from linear theory against which our nonlinear simulation results can be compared.

After introducing model SPH into the hydrocode, we perturbed its density and velocity structure as described above in §4.2 and Figs. 4.3 and 4.4, which was designed to excite the "backward moving" $\ell = m = 2$ bar-mode, that is, the mode for which $\omega_{\rm r} < 0$. Part of the perturbation, for example, included an azimuthal velocity field designed to set the bar-like density distortion into its natural angular oscillation with a frequency $\omega_r \approx 1.219\Omega_0 = 1.595$ in dimensionless hydrocode units ($\approx 10^4$ s^{-1} for the $1.4M_\odot$ star described in column 4 of Table 4.1). We chose a perturbation amplitude such that an integral over the volume of the star, as defined by eq. (3.25), produced a global mass-quadupole moment with amplitude $D_0 \equiv D_{22}(t = 0) \approx 10^{-4}$ in hydrocode units. We then followed the evolution of model SPH on a cylindrical grid with moderately low spatial resolution — $66 \times 130 \times 128$ zones in the radial, vertical and azimuthal directions, respectively — and with the coefficient of the radiation-reaction force term in eq. (3.11) set to the value $\kappa = 20$. The effect of this is that the timescale for the exponential decay was shortened by a factor of 20, to a predicted value $\tau_{\rm GR} = 991(20\Omega_0)^{-1} = 37.9 = 9.63\tau_{\rm pattern}$ in hydrocode units. By shortening the timescale for the exponential decay of the mode from $\tau_{\rm GR} \sim 800$ to $\tau_{\rm GR} \sim 40$, we were able to significantly reduce the amount of computational resources that were required to follow the decay of the barmode while maintaining a decay rate that was slow compared

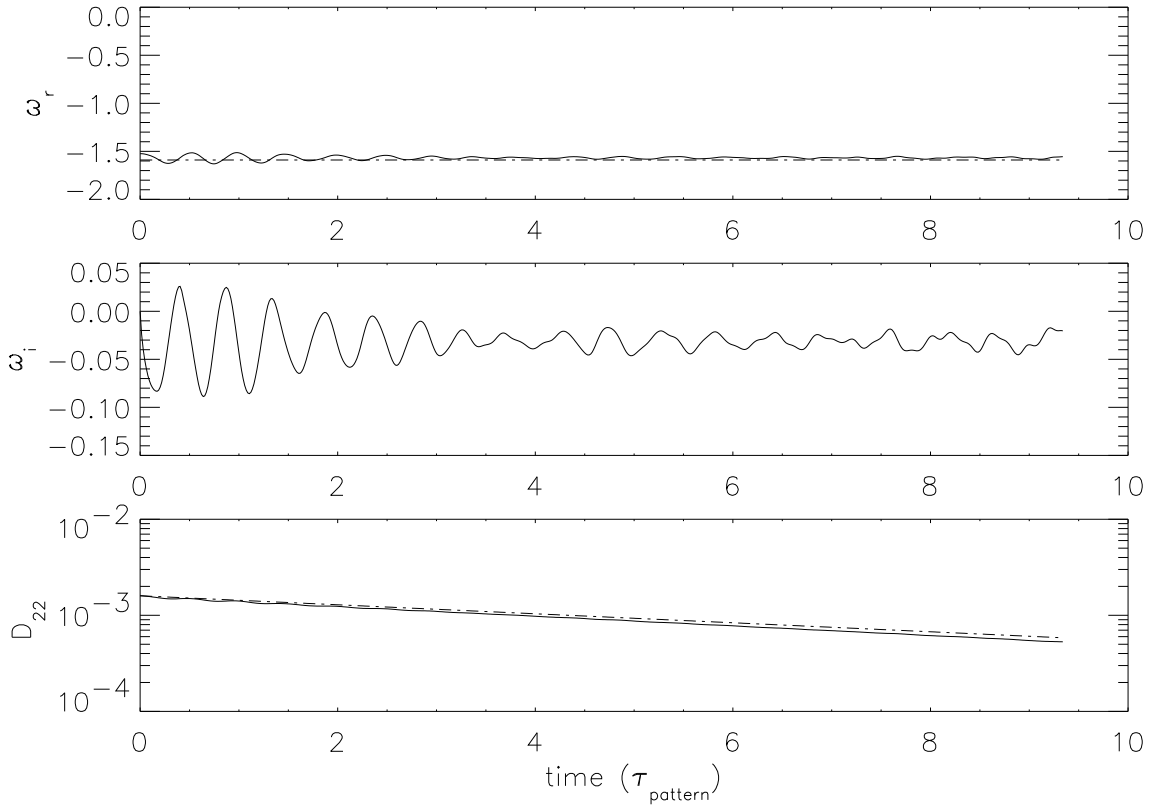

Figure 5.1: The time-evolution of the real part of the complex frequency ω_r (top panel), the imaginary part of the complex frequency ω_i (middle panel) and the amplitude $|D_{22}|$ (bottom panel) of the $\ell = m = 2$ bar-mode from the SPH model evolution. Dashed-dotted lines are predictions from linear analysis.

to the characteristic dynamical time of the system, $\Omega_0^{-1} \sim 1$ in hydrocode units. This is the same technique that was successfully employed in an earlier investigation of the r-mode instability in young neutron stars (Lindblom et al., 2001, 2002).

Figure 5.1 (see Chapter 6) displays the key results from our SPH model evolution. The solid curves in the top two frames display $\omega_{\rm r}$ and $\omega_{\rm i}$ as a function of time through just over nine pattern periods. Each of these frequencies oscillate about a fairly well-defined, mean value: $\langle\omega_{\rm r}\rangle \approx -1.56 = -1.19\Omega_0$; $\langle\omega_{\rm i}\rangle \approx -0.03 = -0.023\Omega_0$. Oscillations about these mean values initially had an amplitude $\sim \pm 0.05 = 0.038\Omega_0$, indicating that our initial nonaxisymmetric perturbation did not excite a pure eigenmode, but these oscillations decreased in amplitude somewhat as the evolution proceeded, which indicates that the noise

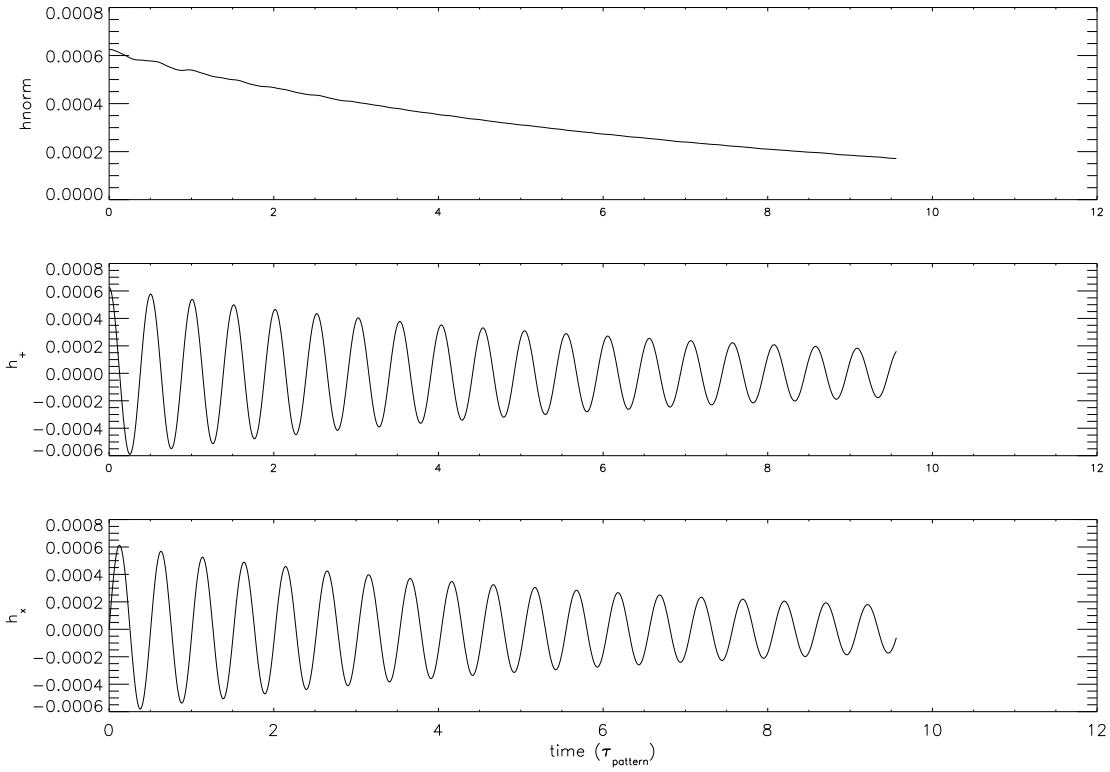

Figure 5.2: The time-evolution of $h_{\rm norm}$, h_+, and $h_\times$ from the SPH model evolution. The observed decay time is consistent with what comes from directly measuring the quadrupole moment amplitude evolution, as in the bottom panel of Fig. 5.1.

has died. Our measured values of $\omega_{\rm r}$ and $\omega_{\rm i}$ are within 3% and 15%, respectively, of the values predicted from linear theory. The solid curve in the bottom frame of Fig. 5.1 shows in a semi-log plot the behavior of $|D_{22}|$ with time. There is a clear exponential decay with a measured damping time (given by the slope of the solid curve) $\tau_{\rm GR} \approx 8.45\tau_{\rm pattern}$. This decay time is completely consistent with the measured value of $\langle\omega_{\rm i}\rangle$ that we have obtained from the middle frame of Fig. 5.1 and, again, within 15% of the predicted value (illustrated by the solid dash-dotted line in the top frame of the figure). The somewhat larger discrepancy in the measured value of ω_i is most probably due to the fact that the GRR formalism used here was derived under the assumption that $|\omega_i| << |\omega_r|$. Because we have artificially amplified the strength of the gravitational radiation in our simulation, the decaying time of the mode was shortened and hence the value of ω_i was amplified. In fact, $|\omega_i/\omega_r| \approx 0.02$ in this simulation. Since ω_i is caused by the Φ_{GR} potential which is proportional to the fifth power of the frequency, fractional discrepancies of the measured value of ω_i which are of order $5|\omega_i/\omega_r| \approx 0.1$ are not unexpected.

The first row of numbers in Table 6.1 summarizes these simulation results. Specifically, columns 4, 5 and 6 list the values of ω_r, ω_i, and $\tau_{\rm GR}$ that have been drawn directly from Fig. 5.1; all three numbers are given in dimensionless code units. In the last two columns of this table, the real and imaginary frequencies have been reexpressed in units of the dynamical frequency, Ω_0. In the last column, we also have adjusted ω_i by the factor of κ in order to show the frequency (and associated growth rate) as it would appear in a real neutron star where the GRR force would not be artificially exaggerated.

Making use of the quadrupole radiation formula derived by Finn & Evans (1990), we also calculated the moment of inertia and its second time derivative, and accordingly calculated the strain of the system, from which we can also derive the decay time. Specifically, the dimensionless strain $h_{\rm norm} \equiv \sqrt{h_+^2 + h_\times^2}$, where h_+ and $h_\times$ are the two polarization states of gravitational waves. For an observer located a distance r along the axis ($\theta = 0$, $\phi = 0$) of

a spherical coordinate system with the origin located at the center of mass of the system, we have

$$h_+ = \frac{G}{c^4}\frac{1}{r}(\ddot{I}_{xx} - \ddot{I}_{yy}) \tag{5.1}$$

$$h_\times = \frac{G}{c^4}\frac{2}{r}\ddot{I}_{xy}, \tag{5.2}$$

where the reduced moment of inertia I_{lm} is defined as

$$I_{lm} \equiv \int \rho(x_l x_m - \frac{1}{3}\delta_{lm} x_k x_k) dx^3. \tag{5.3}$$

Figure 5.2 shows plots of time-evolution of h_{norm}, h_+, and $h_\times$, all of which display an exponential decay similar to the quadrupole moment D_{22}. By measuring the decay rate of h_{norm}, we also obtained a measure of the decaying time scale. The result is $\tau_{\rm damp}/\tau_{\rm pattern} \approx 8.43\tau_{pattern}$, which is in good agreement with the value derived from evolution of the quadrupole moment amplitude.

As Fig. 5.3 illustrates, the total angular momentum of model SPH starts with a very tiny negative value, then it increases with time and approaches zero, that is, its amplitude is decreasing with time. This is consistent with the fact that the bar-mode itself is actually decaying. The minus sign of the angular momentum shows that the perturbation we introduced was a negative mode, which is going backward.

Our simulation of the nonrotating model agrees well with the predictions of the linear theory in many aspects, such as the measurement of the bar-mode oscillating frequency ω_r and the decay time $\tau_{\rm GR}$. This suggests that we have introduced the GRR force correctly into our 3D hydrodynamical code. In the following chapter, we will use this same numerical code to study the GRR-driven bar-mode instability in rapidly rotating neutron star models.

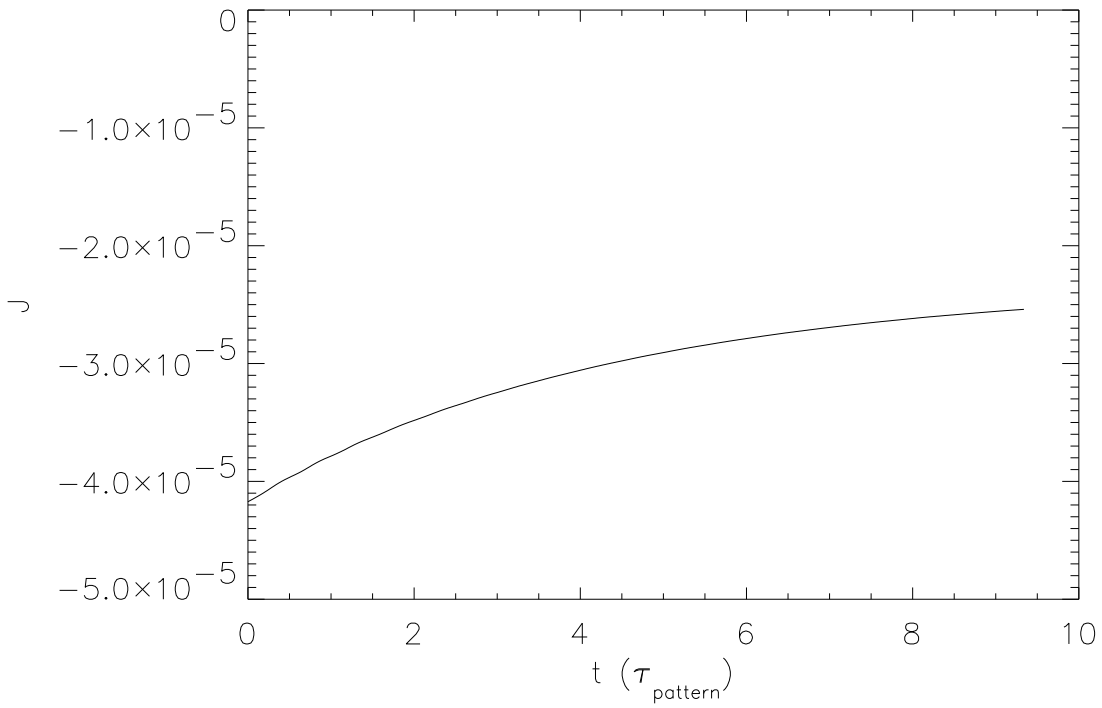

Figure 5.3: The time-evolution of the total angular momentum of the system J from the SPH model evolution. Its negative value reflects that the mode is backward going.

6. Evolutions of Rotating Models

Our primary objective is to investigate the nonlinear development of the f-mode in the unstable region where $\beta \geq \beta_{\rm crit}$. We constructed three uniformly rotating neutron star models with different β values (ROT157, ROT179, ROT181), then used our hydrocode to evolve them. We present our result in the following sections.

6.1 Tests of Initial Perturbation in Rotating Models

In the nonrotating case, we were able to draw upon the result of linear perturbation analyses to design an initial nonaxisymmetric perturbation that would excite a pure "backward moving" $\ell = m = 2$ f-mode in model SPH at time $t = 0$ (see discussion associated with eqs. (4.1) and (4.2), and Figs. 4.3 and 4.4). Unfortunately, there is no such available prescription for the eigenfunction of the $\ell = m = 2$ mode in the rotating case. This makes things more complicated because we have to experiment over a wide range of parameter space in order to find an initial perturbation that is capable of triggering the unstable eigenmode of the rotating model. The parameters that may affect the perturbations include, for example, amplitude of the initial density and velocity perturbations and the value of the factor κ that is used to control the strength of the GRR force in the equation of motion.

We made several test runs with model ROT157 that used combinations of the above parameters with different values, most of which were not successful in mimicking the eigenfunction of the mode. Our diagnostics showed that the perturbations primarily introduced undesirable noise into the system. As an illustration, Fig. 6.1 shows the results of one of these test runs; the large fluctuations of the measured frequency indicate that the perturbations applied to the initial model brought in a lot of noise instead of cleanly exciting the expected eigenmode.

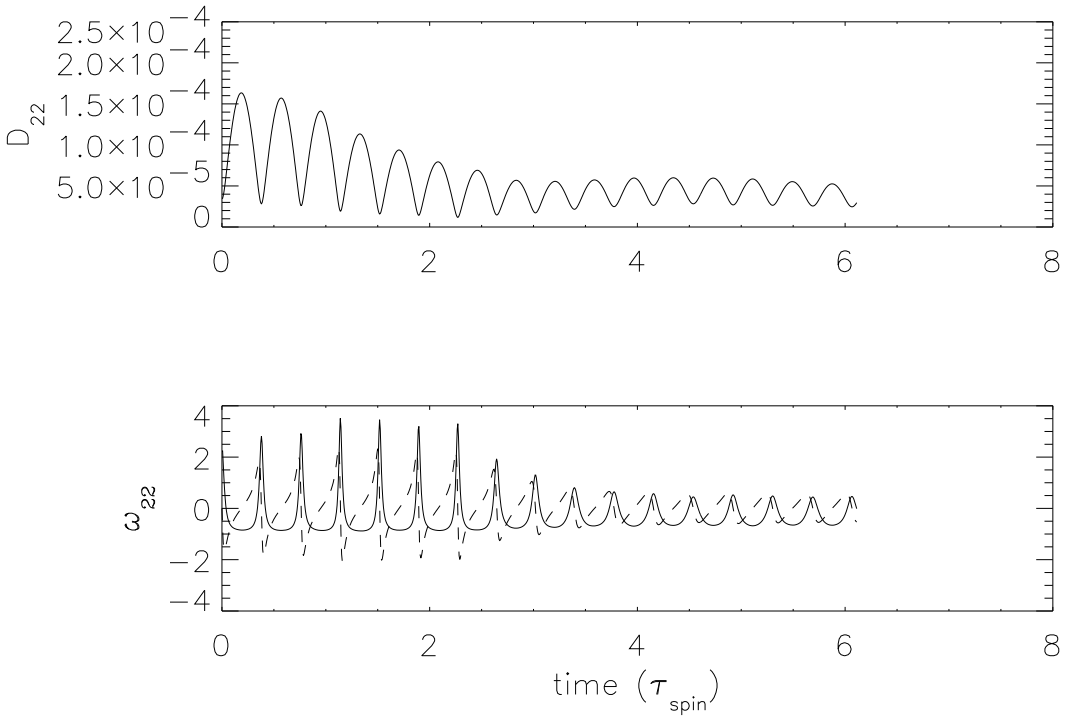

Figure 6.1: The time-evolution of the amplitude $|D_{22}|$ (top panel) and the real (bottom: solid line) and imaginary (bottom:dashed line) components of the $\ell = m = 2$ bar-mode frequency from a test run of model ROT157. The large fluctuations indicate that the initial perturbations bring in a lot of noise instead of the eigenmode. Time is shown in units of the initial rotation period $\tau_{\rm spin} = 2\pi/\Omega_{\rm rot}$ of the model; frequencies are shown in dimensionless code units.

We realized, however, that the rotating models that we were able to build were just beyond the critical limit for the onset of the secular bar-mode instability, thus the eigenfrequency of the unstable "backward moving" mode should be very close to zero in the inertial frame. This fact has two effects. 1) Since its eigenfrequency is very close to zero, the mode should be almost stationary in inertial space. Therefore, a density perturbation alone would be closer to the eigenmode than the combination of a density perturbation and velocity perturbation would be. With this in mind, we decided to only apply a density perturbation to the initial state of our rotating models and exclude the velocity perturbation. 2) The GRR force is proportional to the fifth power of the eigenfrequency of the mode and, hence, becomes very weak in these marginally unstable models. It was therefore necessary to adopt an unusually large value of the factor κ, in order to see the growth of the $\ell = m = 2$ f-mode.

Figures 6.2 and 6.3 show the results of a test run, in which we sccessfully triggered the secular bar-mode in model ROT157 by applying only the density perturbation to the initial model; the resolution of this test run is $130 \times 98 \times 128$ in the radial, vertical, and azimuthal directions, respectively. Figure 6.2 shows the time evolution of the quadrupole moment D_{22} (top panel), ω_r and ω_i (bottom panel). The evolution can be divided into two stages, stage one is when $[0 \leq t/\tau_{\rm spin} \lesssim 11]$; stage two is when $[t/\tau_{\rm spin} \gtrsim 11]$, where $\tau_{\rm spin} \equiv 2\pi/\Omega_{\rm rot}$ is the spin period of the unperturbed rotating neutron star. In stage one, the factor κ was set to 2×10^5; the magnitude of D_{22} doesn't appear to grow, and the magnitude of the eigenfrequency (bottom panel of Fig. 6.2) still contains large fluctuations. These all indicate that our choice of the value of κ was too small. Then, in stage two, starting from around $10.5\tau_{\rm spin}$, we set κ to 10^7. As a result, the amplitude of D_{22} starts to grow exponentially and continues to grow through the end of the simulation; Simultaneously, the fluctuation in the magnitude of the measured frequency starts to die out, which indicates that a pure eigenmode has developed. As the amplitude of the mode grew, it cleaned itself out from various noises and dominated the entire system. Therefore, we obtained

Table 6.1: Simulation Results

SPH	1.308	2.00×10^1	-1.56	-0.03	34	-1.19	-1.1×10^{-3}
ROT157	1.459	1.0×10^7	$+0.12$	$+0.03$	32	$+0.08$	$+2.1 \times 10^{-9}$
ROT181	1.488	1.75×10^5	$+0.27$	$+0.08$	12	$+0.18$	$+3.1 \times 10^{-7}$

a pretty constant eigenfrequency in the late stage of the evolution. Figure 6.3 shows the time evolution of the real and imaginary parts of D_{22} during this same test evolution. The fact that the real and imaginary parts of D_{22} both show a very low frequency oscillation compared to the spin of the star suggests that this mode is indeed the backward going mode whose frequency just passes zero. This is also consistent with the slightly positive value of the measured ω_r. Notice that ω_i has a very small positive value, which is consistent with the very slow exponential growth of the mode. The second row of numbers in Table 6.1 summarizes the results of this simulation, including the measured ω_r, ω_i, and $\tau_{\rm GR}$.

At the end of the late stage of this test run, the quadrupole moment was still exponentially growing. In order to study the nonlinear behavior of the secular bar-mode, we decided to use a more rapidly rotating neutron star, model ROT181, which should have a shorter growth time and allow us to follow the development of the secular bar-mode into nonlinear regime.

6.2 Evolution of Model ROT181

6.2.1 Radiation-reaction with $\kappa = 1.75 \times 10^5$

Model ROT181, which has the highest spin rate among our initial models, was introduced into our hydrocode with a nonaxisymmetric perturbation in the density that had the same structure as the perturbation that was introduced into model SPH. Because we expected the natural oscillation frequency of the bar-mode to be close to zero (as viewed from an inertial reference frame), however, we did not perturb the velocity field of the model. Based on our experiment with model ROT157, we hoped this would give the system an

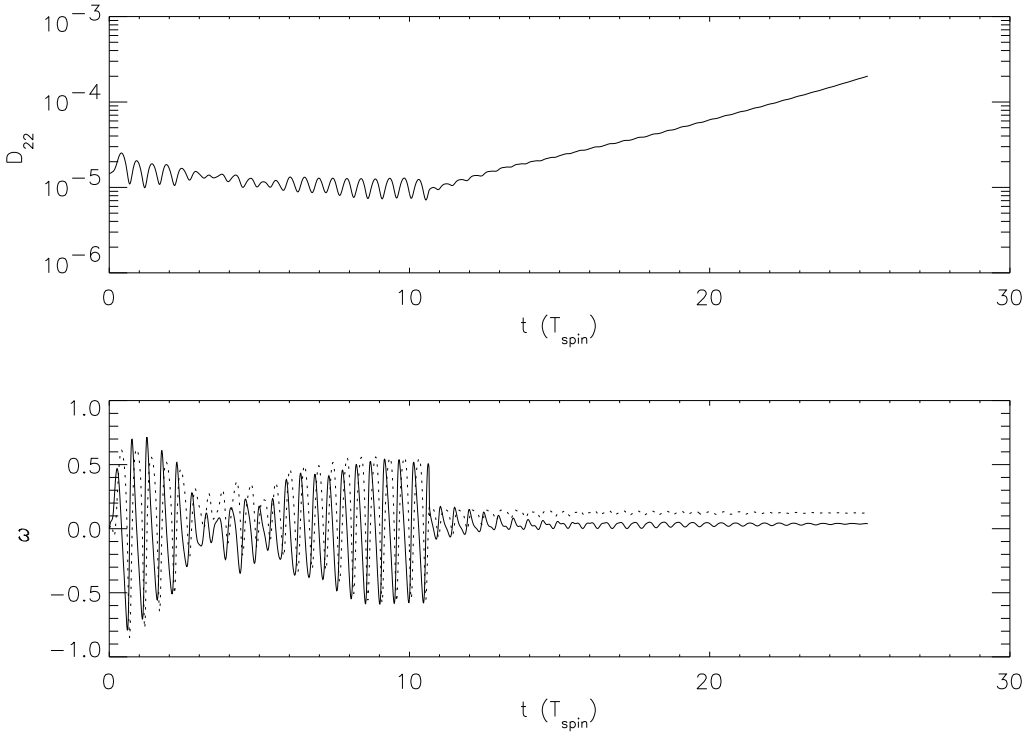

Figure 6.2: The time-evolution of $|D_{22}|$ (top panel) and ω_r (bottom: dashed line) and ω_i (bottom: solid line) of the $\ell = m = 2$ bar-mode from the second test run of model ROT157. From $t = 0$ to $t = 10.5$, $\kappa = 2 \times 10^5$; after $t = 10.5$, κ is set to 10^7. Notice that after $t = 10.5$, the quadrupole moment D_{22} grows exponentially; meanwhile, ω_r stabilized at a very small positive value, and ω_i has a very small positive value, which suggests that the mode is growing very slowly.

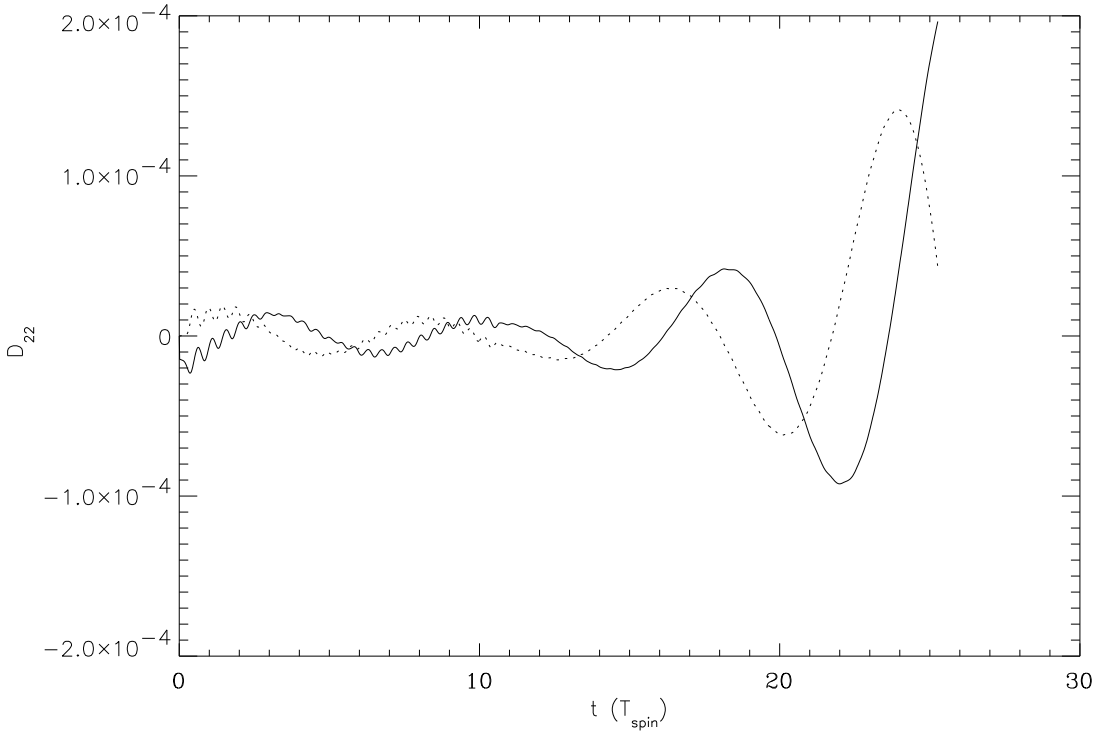

Figure 6.3: The time evolution of the real part of D_{22} (solid line) and the imaginary part of the D_{22} (dotted line) during the second test run of model ROT157. The fact that they both show a very low frequency oscillation compared to the spin of the star, suggests that this mode is indeed the backward going mode whose frequency is just above zero as viewed from the inertial reference frame. This is also consistent with the slightly positive value of the measured ω_r.

initial perturbation that was close to its pure eigen-mode. We followed the evolution of model ROT181 on a cylindrical grid with a resolution of $130 \times 128 \times 98$ zones in ϖ, ϕ, and z, respectively, and with the coefficient of the radiation-reaction force term set to $\kappa = 1.75 \times 10^5$ (Since the ROT181 model rotated faster than the ROT157 model, we expected that the bar-mode of model ROT181 would have a larger eigenfrequency than that of model ROT157. Because the growth rate is proportional to the eigenfrequency to the fifth power, we expected a value of $\kappa \sim 10^5$ to suffice. Note that fewer vertical grid zones were required than in model SPH because model ROT181 was significantly rotationally flattened (see Fig. 4.2), but more radial zones were used than in model SPH in order to allow room for model ROT181 to expand radially during the nonlinear-amplitude phase of its evolution.

Figures 6.4 and 6.5 display some of the key results from this ROT181 model evolution. The bottom frame of Fig. 6.4 shows the time-dependent behavior of the real (dash-dotted curve) and imaginary (solid curve) components of ω_{22}, in our code's dimensionless frequency units; the top frame displays the time-dependent behavior of $|D_{22}|$. Figure 6.5 shows how the global parameters $T/|W|$ (solid curve) and J (dashed curve) evolved with time. The behavior of the model can be best described in the context of three different evolutionary phases: *Early* $[0 \leq t/\tau_{\rm spin} \lesssim 7]$; *intermediate* $[7 \lesssim t/\tau_{\rm spin} \lesssim 12]$; and *late* $[t/\tau_{\rm spin} \gtrsim 12]$, where $\tau_{\rm spin} \equiv 2\pi/\Omega_{\rm rot} = 6.47$ in dimensionless code units.

During the model's *early* evolution, both components of the frequency ω_{22} oscillate about well-defined, mean values: $\langle \omega_{\rm r} \rangle \approx 0.27 = 0.181\Omega_0$; $\langle \omega_{\rm i} \rangle \approx 0.08 = 0.054\Omega_0$. During this same phase of the evolution, both J and $T/|W|$ remain fairly constant, but $|D_{22}|$ increases exponentially with a growth time (obtained from the slope of the displayed curve) $\tau_{\rm GR} \approx 1.85\tau_{\rm spin}$. This growth time is completely consistent with the measured value of $\langle \omega_{\rm i} \rangle$, from which we would expect $\tau_{\rm GR}/\tau_{\rm spin} = \langle \omega_{\rm i} \rangle^{-1}(\Omega_{\rm rot}/2\pi) = 1.93$. The third row of numbers in Table 6.1 summarizes these simulation results.

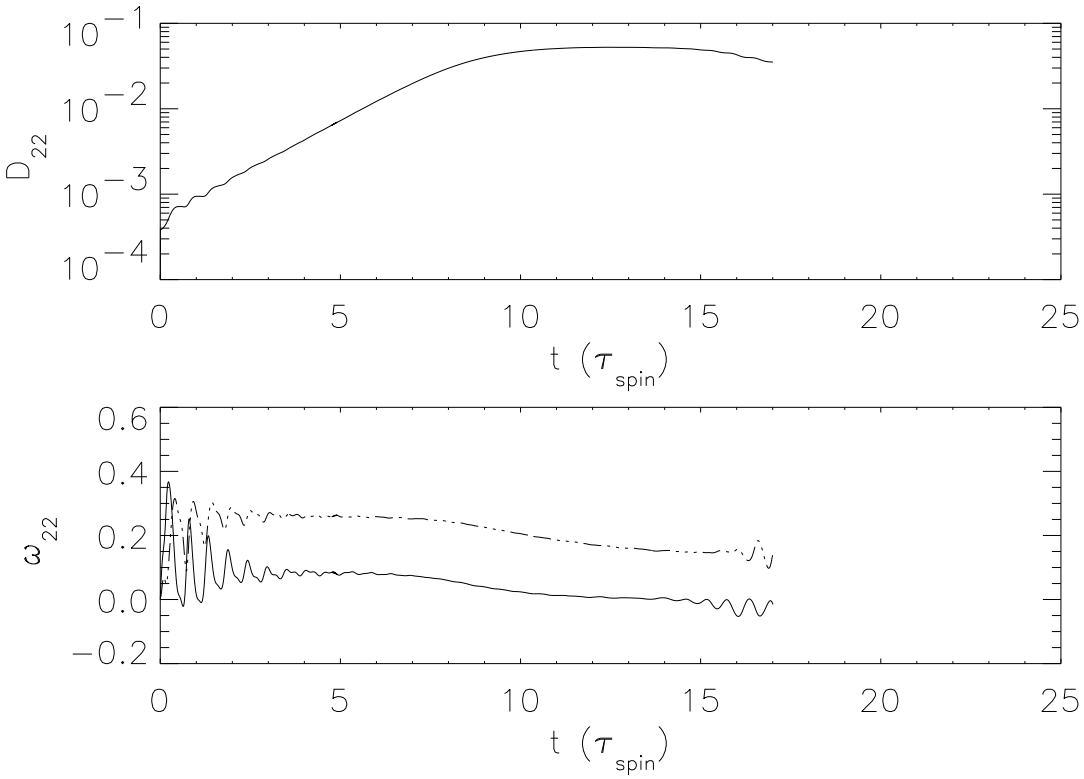

Figure 6.4: The time-evolution of the amplitude $|D_{22}|$ (top) and the real (bottom: dash-dotted curve) and imaginary (bottom: solid curve) components of the $\ell = m = 2$ bar-mode frequency from model ROT181. Time is shown in units of the initial rotation period $\tau_{\rm spin} = 2\pi/\Omega_{\rm rot}$ of the model; frequencies are shown in dimensionless code units.

After approximately seven rotation periods, the amplitude of $|D_{22}|$ begins to saturate, and the model deforms into a clearly visible bar-like configuration with an axis ratio measured in the equatorial plane of approximately 2:1 (see Fig. 6.6). The bar-like structure is initially spinning with a frequency given by $\langle\omega_{\rm r}\rangle/2$, as measured during the *early* phase of the ROT181 evolution. This pattern frequency of the bar is a factor of 7.2 smaller than the rotation frequency $\Omega_{\rm rot}$ of the model in its initial, axisymmetric state, so it is not surprising that the bar also exhibits sizeable internal motions – it has a "Dedekind-like" structure. Figure 6.6 illustrates the structure of the model at this time. Both frames contain the same set of equatorial-plane, isodensity contours delineating the bar, along with a set of velocity vectors depicting the fluid flow inside the bar: on the left-hand-side, the velocity vectors are drawn in a frame corotating with the bar (*i.e.*, rotating at the frequency, $\langle\omega_{\rm r}\rangle/2$) to illustrate the elliptical streamlines of fluid flow within the "Dedekind-like" bar; on the right-hand-side, the velocity vectors are drawn in a frame rotating at the frequency $\Omega_{\rm rot}$. When viewed in this latter frame, one sees a global velocity structure that is very similar to the flow-field depicted in Fig. 4.4, that is, it resembles the natural eigenfunction of the $\ell = m = 2$ bar-mode that was derived by perturbation analysis for nonrotating spherical stars, such as our model SPH. We note that this velocity structure developed spontaneously in model ROT181, as the initial model contained no velocity perturbation.

During this *intermediate* phase of the model's evolution, the bar remains a robust configuration, but its pattern frequency slows as the system loses approximately 10% of its angular momentum (through gravitational radiation) and $T/|W|$ drops to a value ~ 0.156. It is particularly interesting to note that, during this phase of the evolution, the GRR driving term in the equation of motion reaches a maximum, then drops as rapidly as it initially rose; this is illustrated in Fig. 6.7, where we have plotted the time-dependent behavior of the product, $|\omega_{22}|^5|D_{22}|$. Although the bar maintains a nonlinear structure, *i.e.*, $|D_{22}|$ remains large, during this *intermediate* phase of the model's evolution $\Phi_{\rm GR}$ drops quickly in concert with a decrease in the frequency $|\omega_{22}|$.

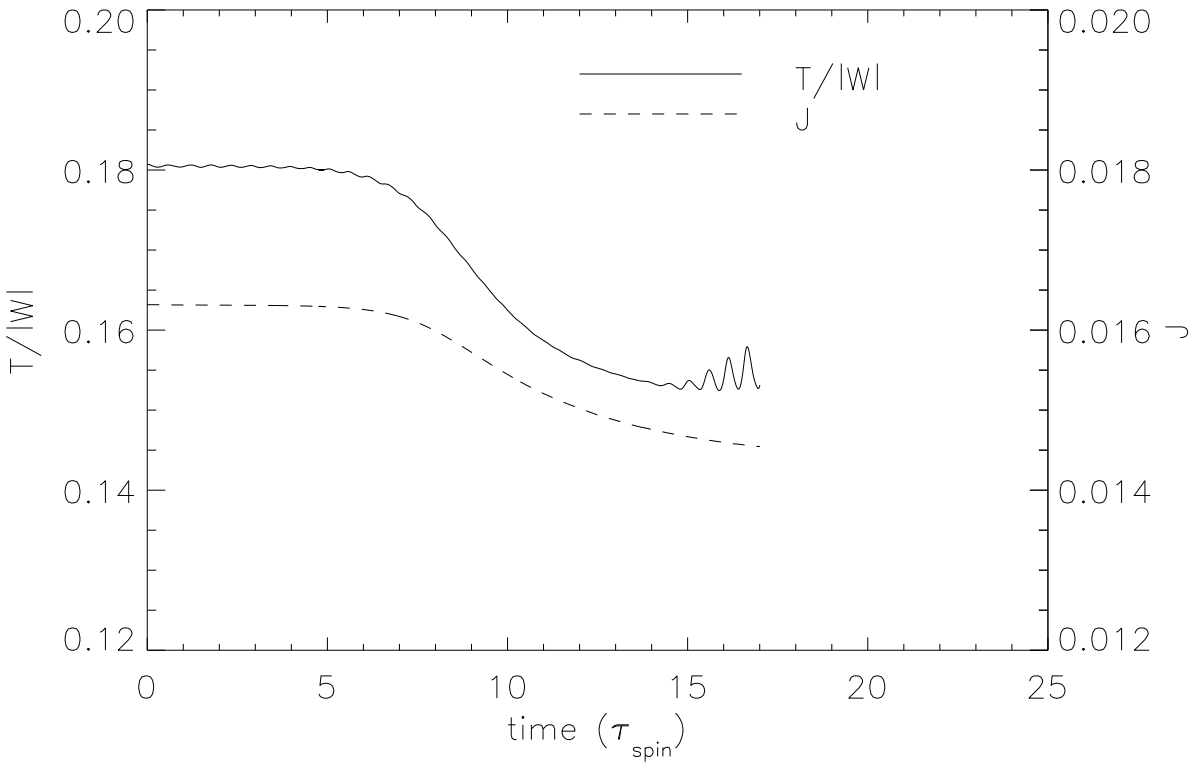

Figure 6.5: The time-evolution of the angular momentum J and the energy ratio $T/|W|$ from model ROT181; J is in dimensionless code units, time is shown in units of the initial rotation period of the model. During the *intermediate* phase of the evolution, both quantities noticeably drop as angular momentum is lost via the GRR force term in the equation of motion.

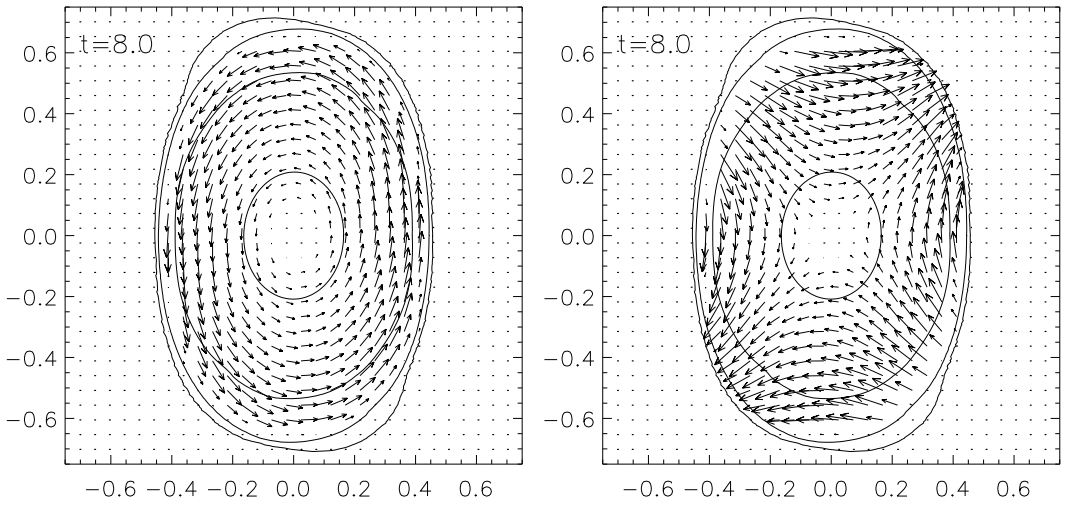

Figure 6.6: The structure of model ROT181 is shown at time $t = 8\tau_{\rm spin}$, during the *intermediate* phase of its evolution. In both frames, solid curves are isodensity contours in the equatorial plane while vectors illustrate the equatorial-plane, velocity flow field as viewed from a frame rotating with a specific frequency as follows: $\Omega_{\rm frame} = \langle\omega_{\rm r}\rangle/2$ (left); $\Omega_{\rm frame} = \Omega_{\rm rot}$ (right).

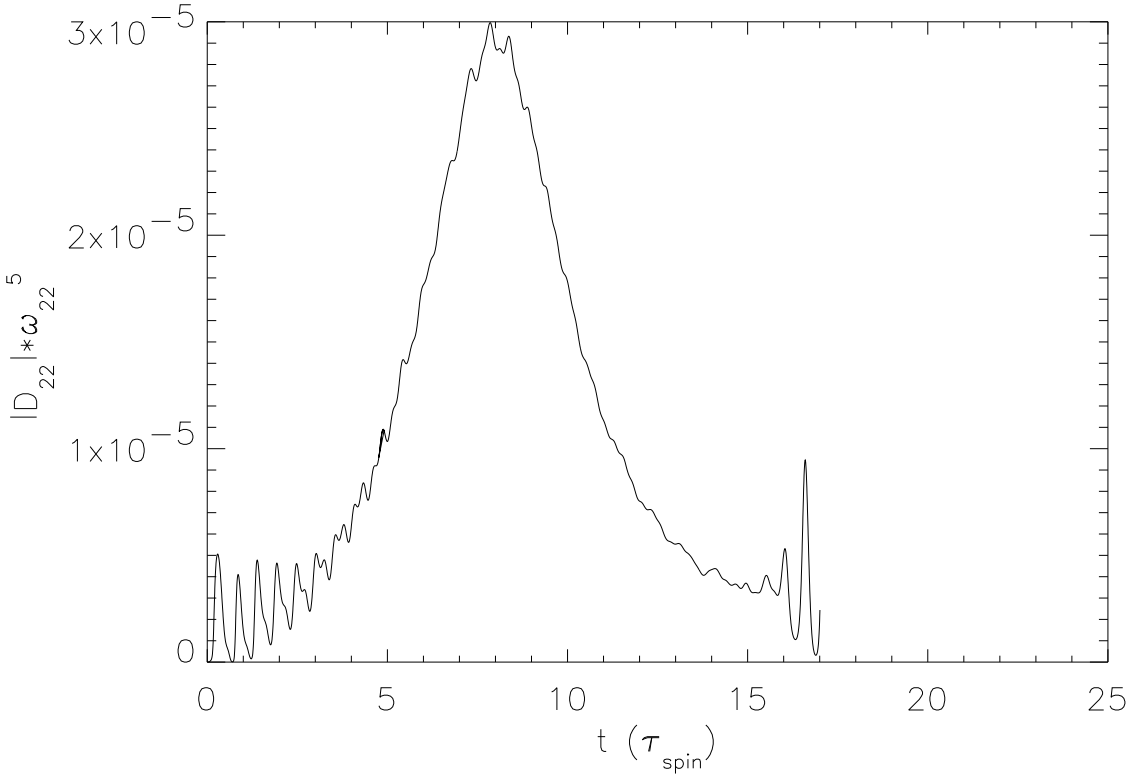

Figure 6.7: From model ROT181, this curve depicts the time-evolution of the product $\omega_{22}^5|D_{22}|$, which indicates the strength of $\Phi_{\rm GR}$ in the equation of motion. Time is shown in units of the initial rotation period.

During the *late* phase of the model ROT181 evolution, the Dedekind-like bar began to lose its coherent structure. Small-scale fluctuations in the density and velocity fields developed throughout the volume of the bar, and these fluctuations grew in amplitude on a dynamical time scale. Even vertical oscillations developed throughout the model, disrupting both the vertically stratified planar flow and reflection symmetry through the equatorial plane that persisted throughout the *early* and *intermediate* phases of the model's evolution. After approximately $15\tau_{\rm spin}$, the model was no longer a recognizable bar, although it remained decidedly nonaxisymmetric, showing density and velocity structure on a wide range of scales in all three dimensions. Figure 6.8 provides a snapshot of model ROT181's structure at $t = 19.9\ \tau_{\rm spin}$ during the *late* phase of its evolution. (Actually, Fig. 6.8 is drawn from the *late* phase of a "revised" evolution of model ROT181, which was evolved further in time; see §6.2.3 for details.) Isodensity contours reveal a nonaxisymmetric structure that no longer can be described simply as a bar and, when viewed from a frame rotating at a frequency $\Omega_{\rm rot}$ (the right-hand frame), the flow field is seen to be more complex than in the bar. To briefly illustrate the entire evolution of model ROT181, Figs. 6.9 through 6.12 show 3D images of model ROT181 at different times.

6.2.2 Detectability of Gravitational-wave Radiation

A rapidly spinning neutron star located in our Galaxy (and perhaps anywhere in our local group of galaxies) that acquires the type of nonlinear-amplitude, bar-like structure that developed in model ROT181 will produce gravitational radiation at a frequency and amplitude that should soon be detectable by gravitational-wave detectors such as LIGO (Abramovici et al., 1992; Abbott et al., 2004), VIRGO (Acernese et al., 2002), GEO600 (Willke et al., 2002; Gossler et al., 2002), or TAMA300 (Tagoshi et al., 2001). As our simulation shows, however, both the amplitude and pattern frequency of the bar — and, hence, the strength and observed frequency of the gravitational radiation — will vary with time. To illustrate this, Fig. 6.13 depicts the evolution of model ROT181 across a "strain-

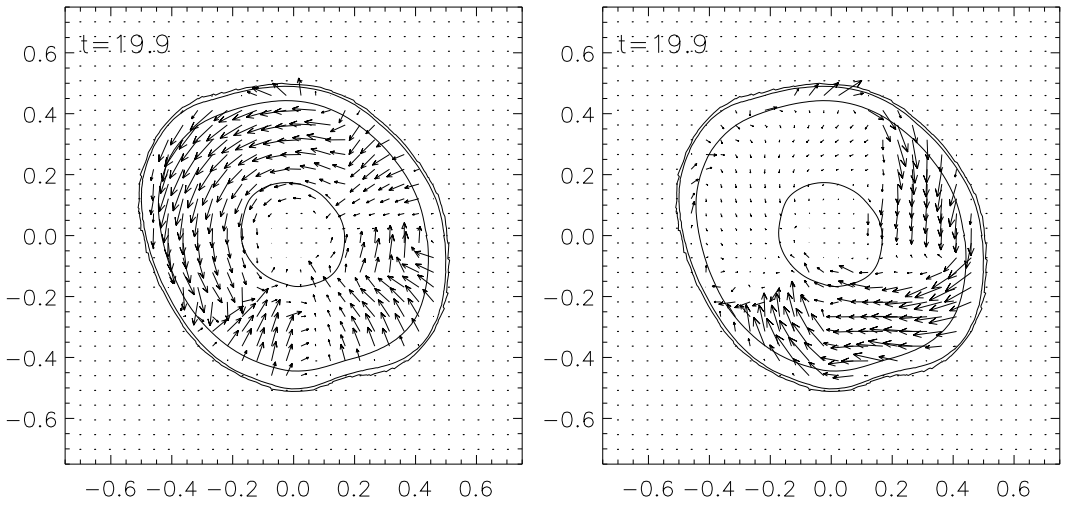

Figure 6.8: The neutron star's structure is shown at time $t = 19.9\ \tau_{\rm spin}$ during the *late* phase of the "revised" ROT181 model evolution. In both frames, solid curves are isodensity contours in the equatorial plane while vectors illustrate the equatorial-plane, velocity flow field as viewed from a frame rotating with a specific frequency as follows: $\Omega_{\rm frame} = 0$ (left); $\Omega_{\rm frame} = \Omega_{\rm rot}$ (right).

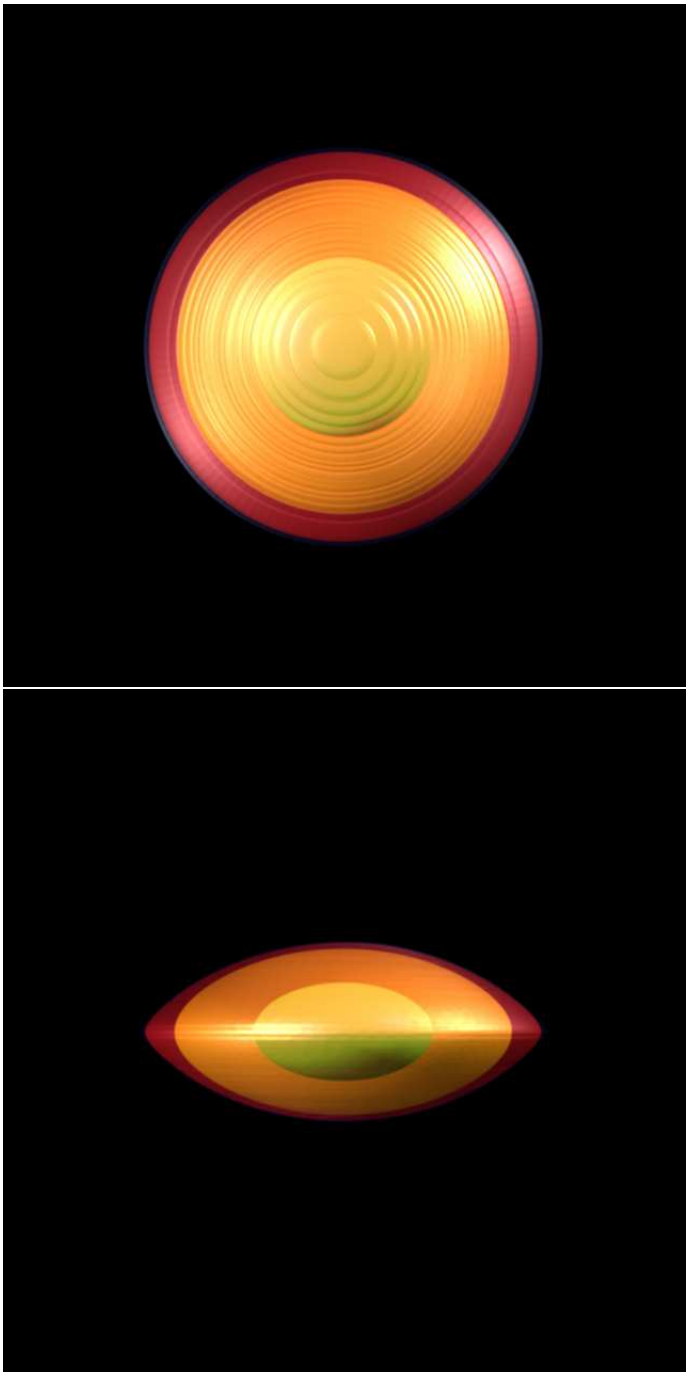

Figure 6.9: 3D images of model ROT181 at $t = 0$. The top panel is the image of the system as viewed from the positive z axis, the bottom panel is the image of the system as viewed from the positive x axis. The four shells correspond to density levels of 0.8 (innermost shell), 0.4, 0.1, and 0.001 (outermost shell), relative to the maximum density.

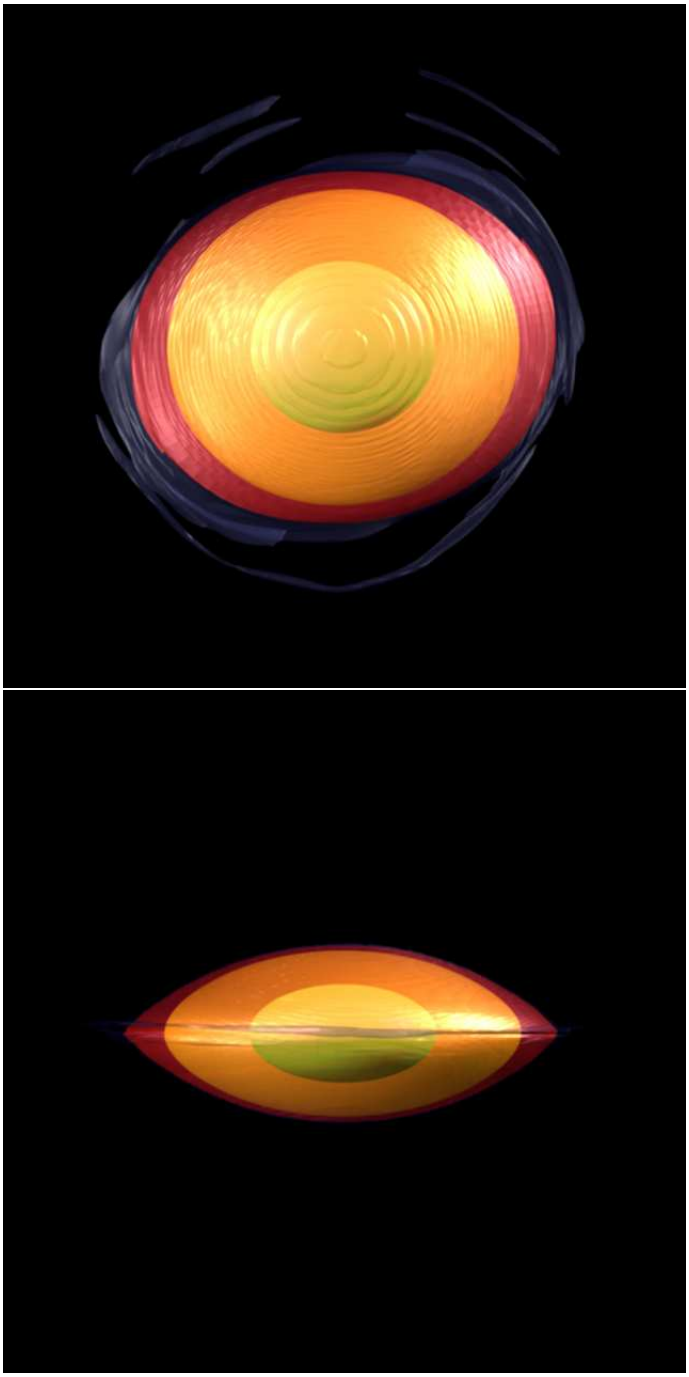

Figure 6.10: Same as Fig. 6.9, but at time $t = 6\tau_{\rm spin}$.

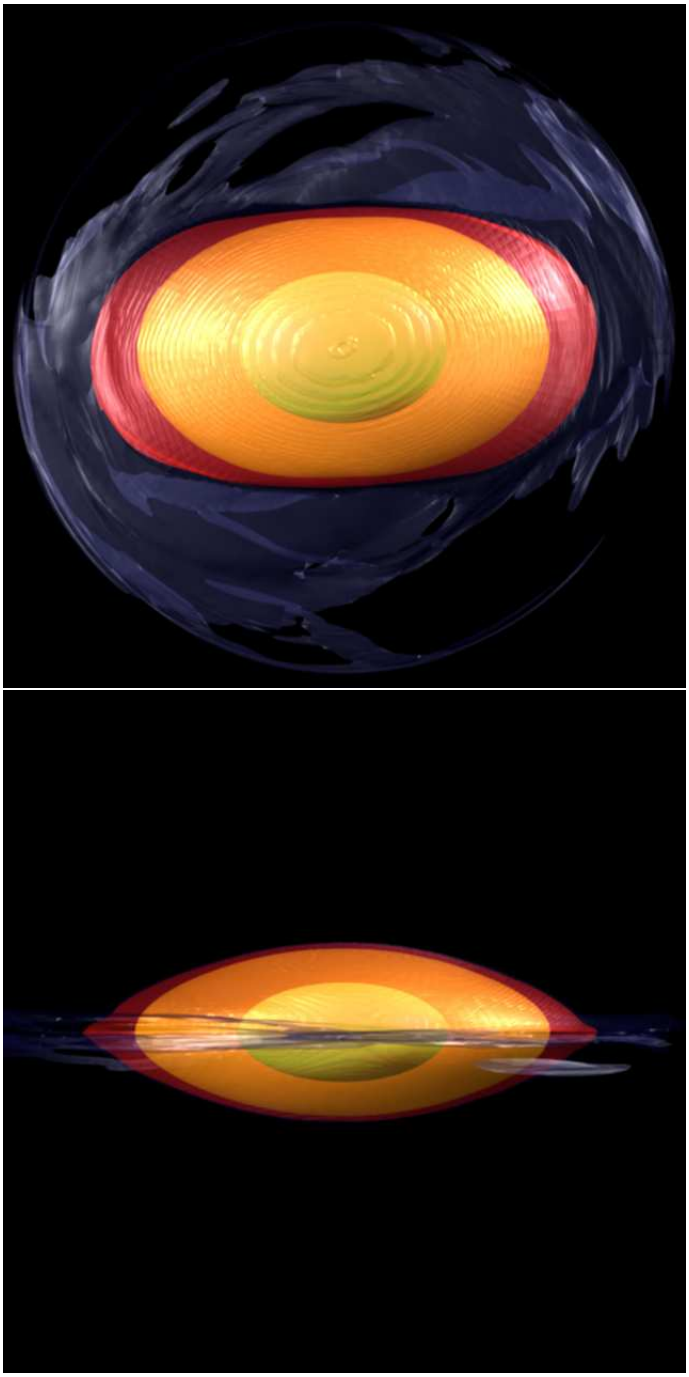

Figure 6.11: Same as Fig. 6.9, but at time $t = 10\tau_{\rm spin}$.

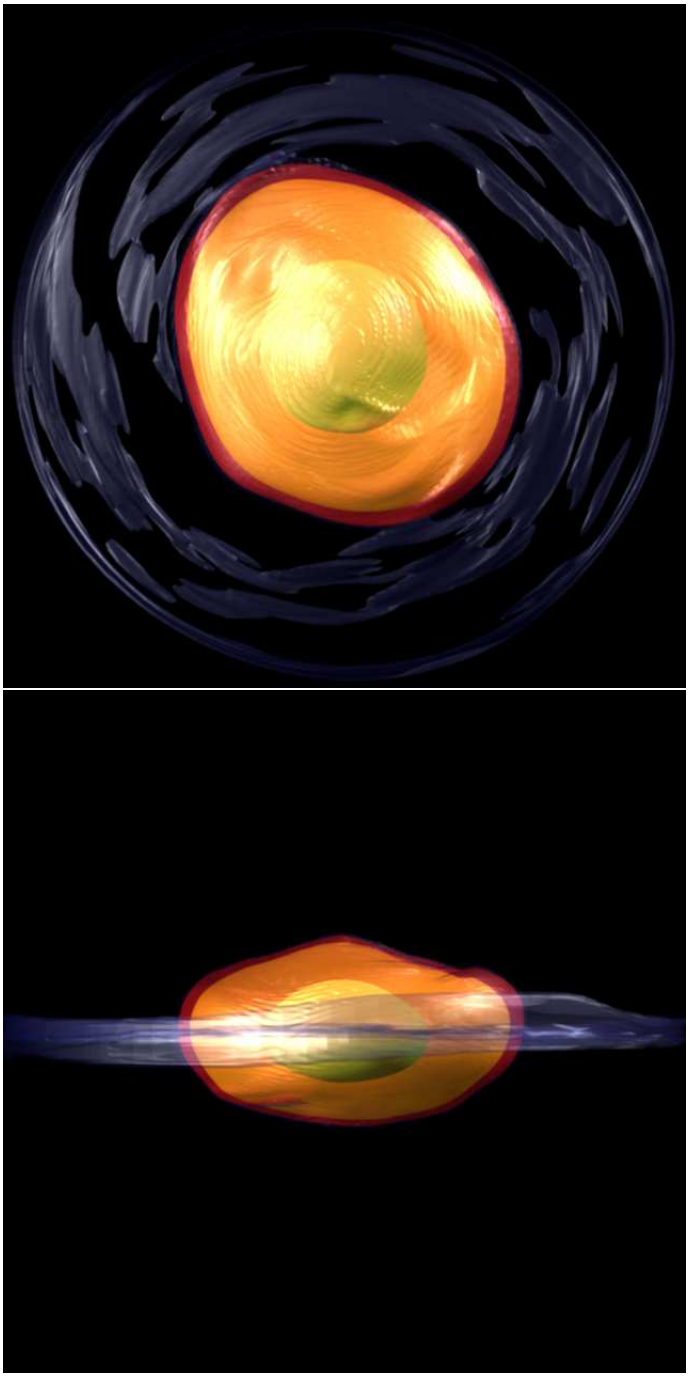

Figure 6.12: Same as Fig. 6.9, but at time $t = 19.7\tau_{\rm spin}$.

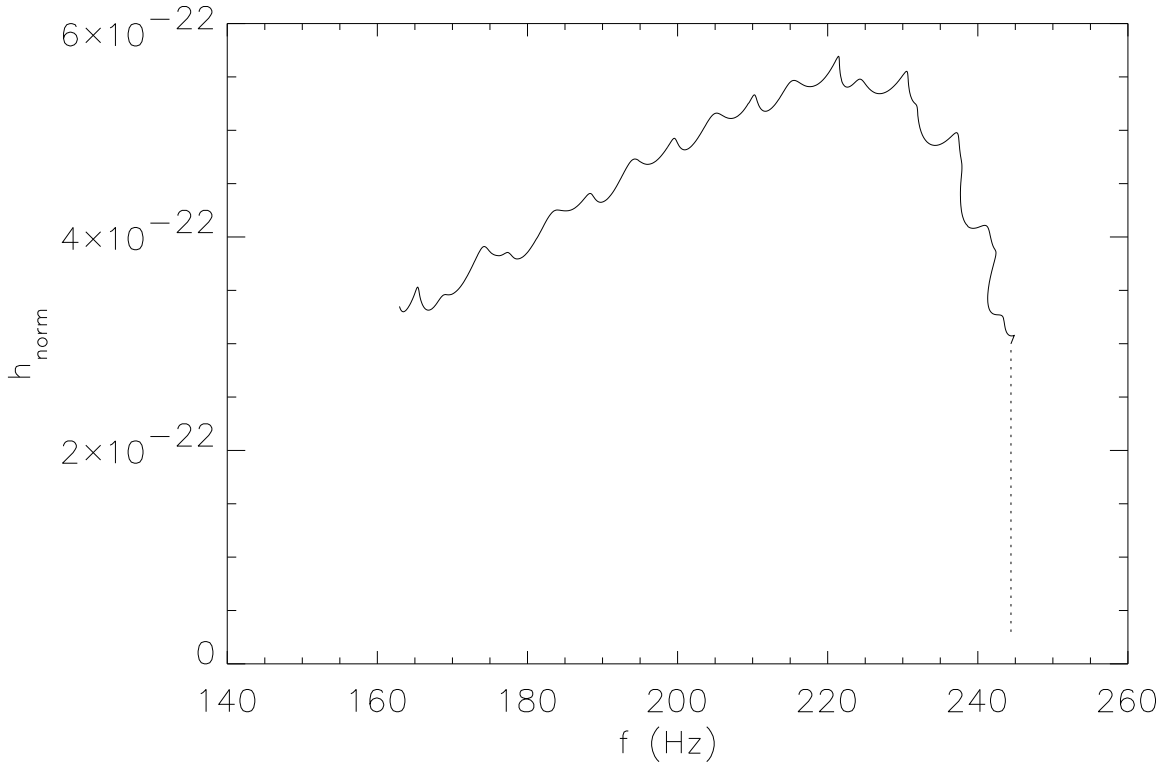

Figure 6.13: The solid curve traces the evolution of model ROT181 in a "strain-frequency" diagram from $6\tau_{\rm spin}$ to $11\tau_{\rm spin}$. As is schematically illustrated by the vertical dotted line, initially, the amplitude $h_{\rm norm}$ of the gravitational wave signal grows at a constant frequency, $f = \omega_{\rm r}/(2\pi) \approx 240$ Hz. As energy and angular momentum are radiated from the system, the frequency drops monotonically, and the strain reaches a maximum amplitude then steadily declines.

frequency" diagram, which is often referenced by the experimental relativity community when discussing detectable sources of gravitational radiation. To obtain the strain values $h_{\rm norm}$ shown in Fig. 6.13, we have assumed $r = 10$kpc, and the time-derivative of each reduced moment of inertia was evaluated numerically using the method recommended by Finn & Evans (1990). Model ROT181's evolutionary trajectory in this diagram is strikingly similar to the trajectory that was predicted by Lai & Shapiro (1995) – see their Fig. 4 – using a much simpler, approximate model for the development of the secular bar-mode instability in young neutron stars.

In order to estimate the distance to which a gravitational wave source of this type would be detectable by a gravitational-wave interferometer, such as LIGO, we could integrate under the curve in Fig. 6.13, taking into account the amount of time that the source spends in each frequency band. Because we have artificially amplified the strength of the GRR force, however, our model evolves through frequency space along the curve shown in Fig. 6.13 much more rapidly than would be expected for a real neutron star that experiences this type of instability, hence our model cannot be used directly to estimate the length of time that such a source would spend near each frequency. However, Owen & Lindblom (2002) have outlined a method by which the detectability of a source can be estimated from a knowledge of ΔJ, the total angular momentum that is radiated away from the source via gravitational radiation. Specifically, the signal-to-noise ratio S/N that could be achieved by optimal filtering can be estimated from the expression,

$$\left(\frac{S}{N}\right)^2 \approx \frac{4G}{5m\pi c^3 r^2}\frac{|\Delta J|}{f S_h(f)}\,, \tag{6.1}$$

where m is the azimuthal quantum number ($m = 2$ for the bar-mode), r is the distance to the source, and $S_h(f)$ is the power spectral density of the detector noise at frequency f. From our model ROT181 evolution, we find $\Delta J = 1.67 \times 10^{48}$ g cm^2 s^{-1}; (Based on results from model ROT179, which we evolved using grids with various azimuthal resolutions, we estimate that the uncertainty in this calculated $\Delta J/J$ is $\sim \pm 15\%$.) and during LIGO's third

(S3) science run in late 2003, the 4 km LHO (LIGO-Hanford Observatory) interferometer operated with a noise curve[1] that exhibited $\sqrt{S_h} \approx 8 \times 10^{-23} \sqrt{Hz}^{-1}$ at $f = 220$ Hz, which is the characteristic frequency of the spinning bar in model ROT181. From expression (6.1), we therefore estimate that a source of the type we are modelling could already be detected by LIGO with a $S/N \gtrsim 8$ out to a distance of 0.7 Mpc. With advanced LIGO (using sapphire test masses, the projected noise curve[2] gives $\sqrt{S_h} \approx 1.7 \times 10^{-24} \sqrt{Hz}^{-1}$ at $f = 220$Hz) we estimate that this type of source will be detectable with $S/N \gtrsim 8$ out to 32 ± 3 Mpc.

Of course the detectability of gravitational waves generated by the secular bar-mode instability will also depend on the frequency with which such events occur nearby. To estimate an event rate we can draw on the discussion of Kokkotas (2004) where an estimate was made of the event rate of the dynamical bar-mode instability in young neutron stars. Since the conditions required for the onset of the secular bar-mode instability ($T/|W| \gtrsim 0.14$) are almost as extreme as the conditions required for the onset of the dynamical bar-mode instability ($T/|W| \gtrsim 0.27$), it would be very surprising if the two event rates were not similar. If we assume that only young neutron stars can be rotating rapidly enough to be susceptible to either bar-mode instability, and if we assume that a neutron star can form only from the collapse of the core of massive star, then a reasonable upper limit on the rate of these events will be given by the event rate of Type II supernovae, that is, 1-2 per century per gas-rich galaxy (Cappellaro, Evans, & Turatto, 1999). (Another scenario is that rapidly rotating neutron stars form from the accretion-induced collapse of white dwarfs. But according to Liu 2002, the frequency of such events is orders of magnitude lower than the event rate of Type II supernovae.) Adopting a local galaxy density of $n_{\rm g} \approx 0.01$ Mpc^{-3} (Kalogera et al., 2001), we should expect $\lesssim 30$ Type II supernovae

[1]Noise curves for the three separate LIGO interferometers during the S3 science run can be obtained from URL http://www.ligo.caltech.edu/~lazz/distribution/LSC_Data /s3.html.

[2]Projected noise curves for the advanced LIGO design using either sapphire or silica test masses can be obtained from URL http://www.ligo.caltech.edu/advLIGO.

each year out to 32 Mpc. Now not all Type II supernovae will produce neutron stars (Kokkotas 2004 estimates, for example that 5-40% of supernova events produce black holes instead), and only a fraction $f_{\rm rot}$ of neutron stars will be formed with sufficient rotational energy to be susceptible to a bar-mode instability, so the predicted event rate should be reduced accordingly. A naive estimation based on angular momentum conservation during core collapse suggests that virtually all newly born neutron stars will be formed rapidly rotating and, therefore, $f_{\rm rot} \sim 1$; this is the direction Kokkotas (2004) leans. But models of axisymmetric core collapse (Tohline, 1984; Dimmelmeier, Font, & Müller, 2002a,b; Ott et al., 2004) indicate that the ratio of energies $T/|W|$ in a newly formed neutron star is quite sensitive to the equation of state of the core during its collapse and it is easy to imagine physical scenarios in which appropriately rapidly rotating neutron stars will rarely be formed; therefore, $f_{\rm rot} \ll 1$. At the present time it is not clear which picture is more correct, but adopting the more optimistic view it should be possible for LIGO to detect on the order of ten such events each year.

6.2.3 Late Evolution with $\kappa = 0$

In an effort to determine whether the Dedekind-like bar structure was destroyed during the *late* phase of the ROT181 model evolution as a result of physically realistic, hydrodynamical processes, or by a radiation-reaction force that was artificially too large, we set $\kappa = 0$ then re-ran the last segment of the simulation, starting from $t = 11\tau_{\rm spin}$. This "revised" evolution produced results that were qualitatively identical to the late phase of the GRR-driven evolution. That is, the bar was destroyed by the dynamical development of velocity and density structure on a wide range of scales in all three dimensions. In an effort to quantitatively describe this relatively complex structure, Fig. 6.14 shows a representation of the azimuthal Fourier-mode amplitudes of the model's density distribution at two points in time: $t = 10\tau_{\rm spin}$, when the bar was well-developed; and $t = 20\tau_{\rm spin}$, after the higher-order nonaxisymmetric structure was well-developed. (Note that the *late* phase of this "revised"

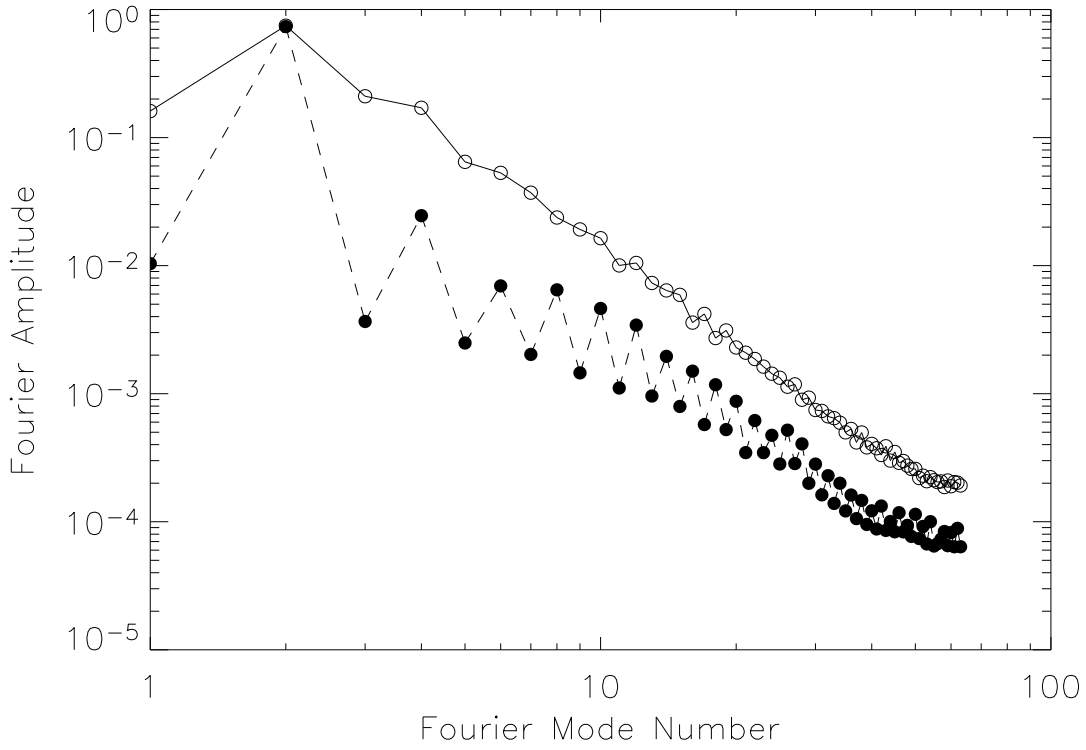

Figure 6.14: A spectrum of the Fourier-mode amplitude of the azimuthal density distribution is shown at time $t = 10\tau_{\rm spin}$ (filled circles), when the bar was well-developed, and at time $t = 20\tau_{\rm spin}$ (open circles), after the higher-order modes destroyed the coherent bar in the "revised" evolution of model ROT181. To guide the eye, amplitudes determined for various modes at the same time are connected by straight line segments.

evolution was followed somewhat farther in time than the original model ROT181 evolution described in §6.2.1.) At the earlier time, only the $m = 2$ amplitude contained a significant amount of power, and all odd amplitudes were smaller than their even neighbors. At the later time the Fourier-mode amplitudes appear to be related to one another by a simple power law, indicating that power has been spread smoothly over all resolvable length scales.

6.2.4 Analysis of the Dedekind-like Bar Structure

Contrary to the simulations of *dynamical* bar-mode instability (Cazes & Tohline, 2000), which produced very stable bar-like configurations that existed for many dynamical times, the Dedekind-like bar configuration that formed from our simulation only survived for a

few spin periods of the initial rotating neutron star. Its coherent bar-structure was then destroyed by high order turbulence that developed on small length scales. In order to understand the stability discrepancy between these two bar-like configurations, we have analyzed the internal structures of these bars in much more details. Although we have been unable to completely answer the question of why the Dedekind-like bar configuration is dynamically unstable, these additional analyses do help us to gain a better understanding of the properties of a GRR-driven Dedekind-like bar.

Figure 6.15 shows the contours of constant Mach numbers throughout the equatorial plane of the Dedekind-like bar at $t = 13\tau_{\rm spin}$, where the Mach number is the ratio between the fluid velocity in the inertial frame and local sound speed. Contours are plotted for four different mach numbers: 0.2, 1.0, 2.0, and 5.0. Most of the outer region of the bar is in supersonic motion (with Mach numbers greater than 1); the inner regions are in subsonic motion (with Mach numbers less than 1). This is a very surprising observation. For this system, which has a pretty stiff EOS ($n = 0.5$), a large portion of mass in the outer shells is moving supersonically; However, the bar studied by Cazes & Tohline (2000) was centrally condensed and had a softer EOS ($n = 3/2$), but it had only a very tiny portion of mass moving supersonically in the outermost region.

On the other hand, shocks might develop between these supersonic and subsonic regions and affect the adjoining flows. In order to locate where shocks might form in the Dedekind-like bar, Fig. 6.16 shows the divergence of the velocity field in the equatorial plane of model ROT181 at $t = 15\tau_{\rm spin}$. The blue regions are where the velocity divergence is positive, and the red regions are where the velocity divergence is negative, which should be regions that are undergoing compression and may give birth to shocks. There is a very clear quadrupole feature which is similar to that of the initial velocity perturbation we have applied to our SPH model.

According to linear theory, gravitational radiation tends to drain angular momentum from the system while conserving the fluid circulation. Figure 6.17 shows the circulation

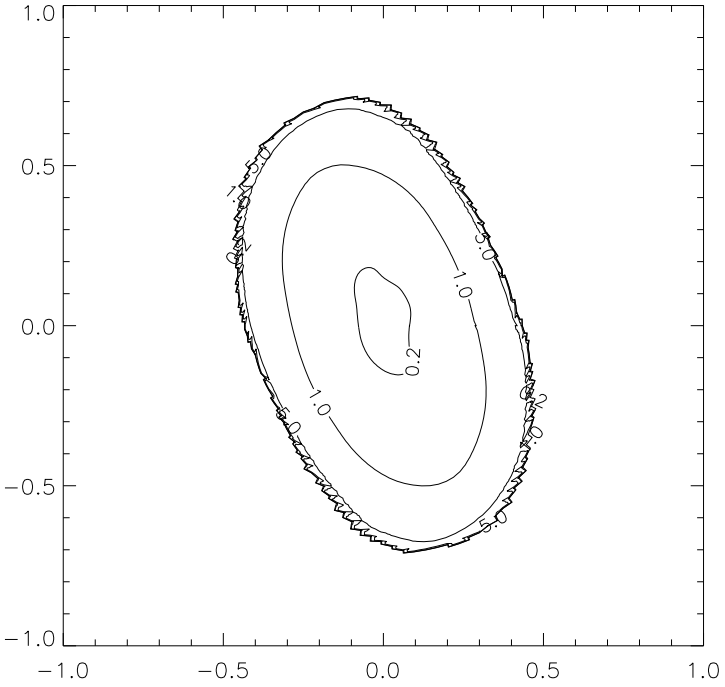

Figure 6.15: From model ROT181 with $\kappa = 1.75 \times 10^5$, the contours identify the local Mach numbers throughout the equatorial plane of the model at $t = 13\tau_{\rm spin}$. The four mach number levels are 0.2, 1.0, 2.0, 5.0 from the innermost region to the outermost region. Regions with a Mach number greater than 1 are in supersonic motion, whereas, regions with Mach number less than 1 are in subsonic motion.

in the equatorial plane at each cylindrical radius of the system at $t = 0$ and $t = 10\tau_{\rm spin}$. Since the initial configuration in the equatorial plane is circular, yet the late configuration in the equatorial plane is elliptical, it is unclear whether that the circulation should be conserved within a circle or an ellipse. However, in order to get a qualitative estimate, we chose to compute circulation at each cylindrical radius by integrating along a circle in the equatorial plane with the same radius both for the initial and late configurations. The sequence denoted by a series of unfilled squares shows the circulation as a function of cylindrical radius at $t = 0$; the sequence denoted by a series of asterisks shows the circulation as a function of cylindrical radius at $t = 10\tau_{\rm spin}$. These two sequences lie very close to each other.

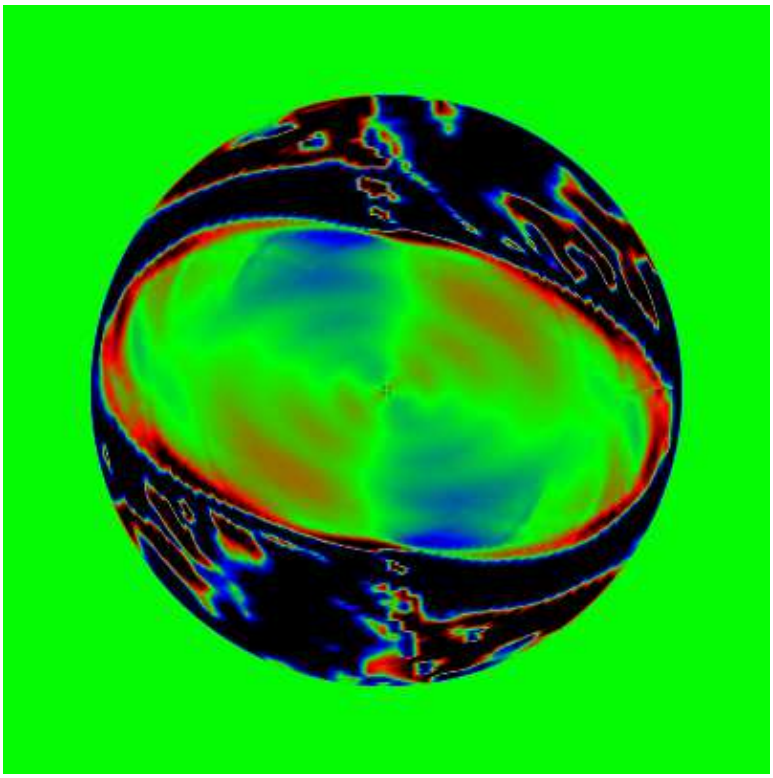

Figure 6.16: From model ROT181 with $\kappa = 1.75 \times 10^5$, this plot shows the divergence of velocity field throughout the equatorial plane at $t = 15\tau_{\rm spin}$. The blue regions are where the velocity divergence is positive and the red regions are where the velocity divergence is negative. A quadrupole structure is obvious.

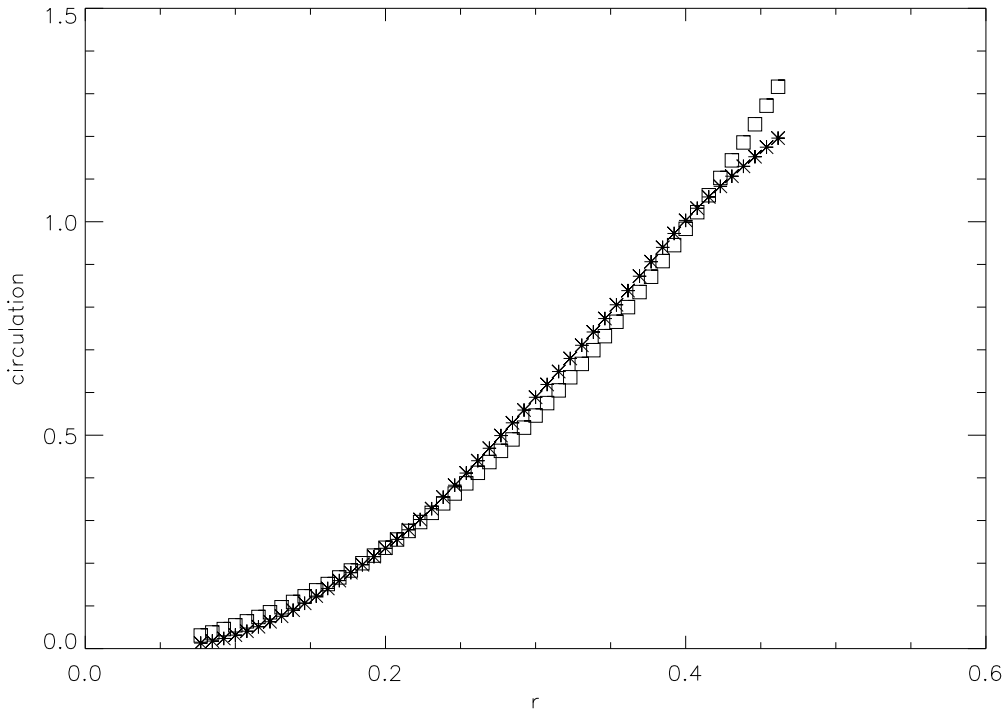

Figure 6.17: From model ROT181 with $\kappa = 1.75 \times 10^5$. The sequence denoted by a series of unfilled squares shows the fluid circulation as a function of cylindrical radius at $t = 0$; the sequence denoted by a series of asterisks shows the circulation as a function of cylindrical radius at $t = 10\tau_{\rm spin}$.

6.3 Evolution of Model ROT179

Our evolution of model ROT181 produced two particularly important results: (1) the linear growth of the bar-mode agrees well with the predictions of linear analysis and its nonlinear development also confirms the previous simplified estimation (Lai & Shapiro, 1995) of the character and strength of gravitational waves that come from the secular bar-mode instability in rotating neutron stars. (2) the fact that the Dedekind flow is destroyed in the late evolution of the bar-mode instability suggests that Dedekind-like ellipsoids tend to be short-lived and that the chance for a Dedekind configuration to exist in our universe is very rare. However, so far we have only followed the development of the secular bar-mode of one model (ROT181) into the nonlinear regime. In order to test if the breakdown of the Dedekind flow in the late evolution is robust, we have made two convergence tests.

Our first convergence test was performed by evolving model ROT179 on a computational grid of resolution $66 \times 66 \times 64$ in the radial, vertical, and azimuthal directions, respectively. (Notice that this grid has roughly a factor of two poorer resolution in each of the three spatial dimensions.) This model had a slightly different value of β from model ROT181, because the HSCF technique did not permit us to construct precisely the same initial state as model ROT181 on the coarser computational grid. We introduced a nonaxisymmetric density perturbation that produced approximately the same initial mass quadrupole moment amplitude $|D_{22}|$ as in model ROT181; and throughout the evolution the coefficient of the radiation-reaction force term was set to $\kappa = 1.75 \times 10^5$ as in the ROT181 run. Because model ROT179 had a lower β value, it had a smaller spin frequency and correspondingly a lower bar-mode frequency. Therefore, we expected the growth rate of the bar-mode in model ROT179 to be slightly slower than it was in the ROT181 simulation. Figures 6.18, 6.19, 6.20, and 6.21 show some key results from this convergence test. For comparison with the results of the ROT181 run, we also show quantities from model ROT181 on the same plots. Figure 6.18 shows the time-evolution of the quadrupole moment amplitude and

the bar-mode frequency. The amplitude of D_{22} grows exponentially to a lower nonlinear amplitude than that of model ROT181, then levels off. One important fact is that it grows slightly slower than it did in the ROT181 model, as expected. The turbulent behavior that destroys the Dedekind flow sets in at a much later time than it did in model ROT181 (This is indicated by the large oscillation of the mode frequency at late times). The delay in development of the smaller scale structure was almost certainly due, in part, to our inability to resolve structure on the smallest scales in model ROT179. But the delay may also have occurred, in part, because the bar itself was never as pronounced as in model ROT181. Similar behavior has been observed in simulations that have analyzed the long-term stability of r-mode oscillations in young neutron stars (Gressman et al. 2002). In Fig. 6.19, the time-evolution of $\beta = T/|W|$ and J show a time-decreasing behavior that is qualitatively similar to model ROT181, but on a much longer time scale. Figure 6.20 shows the time-evolution of the strength of GRR potential, $\sim \omega_{22}^5 |D_{22}|$, from both model ROT179 and model ROT181. The peak of this function also lags by about two spin periods than that of ROT181 model. In Fig. 6.21, the spectrum of the Fourier modes at two different times (when the bar mode is dominant and when the turbulence is fully developed) is also similar to that of model ROT181.

In our second convergence test, we evolved the same model ROT179 on a computational grid of resolution $66 \times 66 \times 128$ in the radial, vertical, and azimuthal directions, respectively. That is, the azimuthal grid resolution matched the grid resolution of our model ROT181 evolution. The key results of this run are shown in Figs. 6.22, 6.23, and 6.24. Figure 6.22 shows the time-evolution of D_{22} and the real and imaginary parts of the mode frequency ω_{22}, figure 6.23 shows the product of $|D_{22}|$ and $|\omega_{22}|^5$ as a function of time; and Fig. 6.24 shows the spectrum of the Fourier-mode amplitude at two different times (when the bar mode is dominant and when the turbulence is fully developed). The results from the *early* and *intermediate* phases of this simulation, when the bar-like structure grows exponentially to the nonlinear regime and levels off, agree completely with that of the lower resolution

ROT179 run. A more interesting thing is that the late break down of the Dedekind flow sets in at a much earlier time compared to the lower resolution run for model ROT179. This makes sense because the angular resolution is doubled, so the interactions between azimuthal modes on small scales are resolved to a much higher degree, which helps the turbulence to grow faster in the higher resolution run of model ROT179. In fact, the turbulent behavior of the system becomes noticeable after $t = 16\tau_{\rm spin}$, exactly as it does in the ROT181 run. This suggests that the turbulent behavior depends largely on the energy cascade among azimuthal modes.

The results of our two convergence tests on model ROT179 confirm the results of our model ROT181 evolution and give us confidence that the break down of the Dedekind flow in the late evolution is a very robust, physical phenomenon.

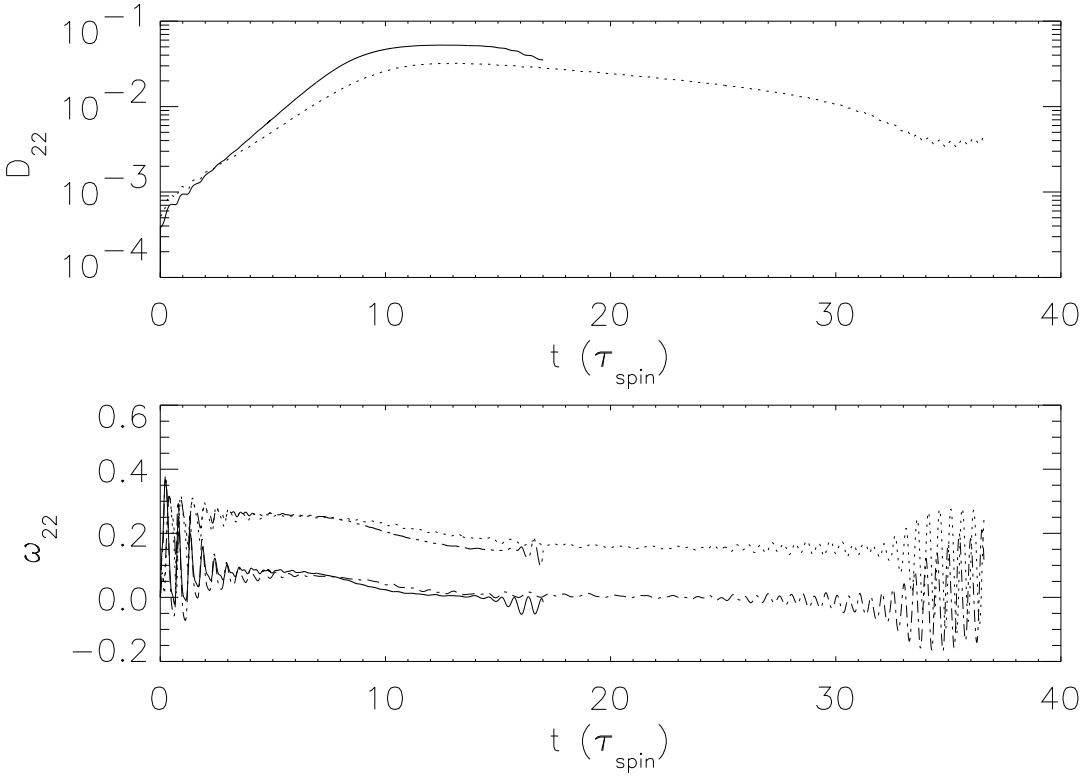

Figure 6.18: The time-evolution of $|D_{22}|$ (top: dotted line) and the real (bottom: dotted curve) and imaginary (bottom: dashed curve) components of the $\ell = m = 2$ bar-mode frequency from model ROT179 on a grid of resolution $66 \times 66 \times 64$. Time is shown in units of the initial rotation period $\tau_{\rm spin} = 2\pi/\Omega_{\rm rot}$ of the model; frequencies are shown in dimensionless code units. Curves from Fig. 6.4 are also drawn in order to provide points of comparison with the model ROT181 evolution. It is very clear that D_{22} of model ROT179 grows more slowly and to a lower amplitude. The higher order instability in model ROT179 also happens at a later time than it does in model ROT181.

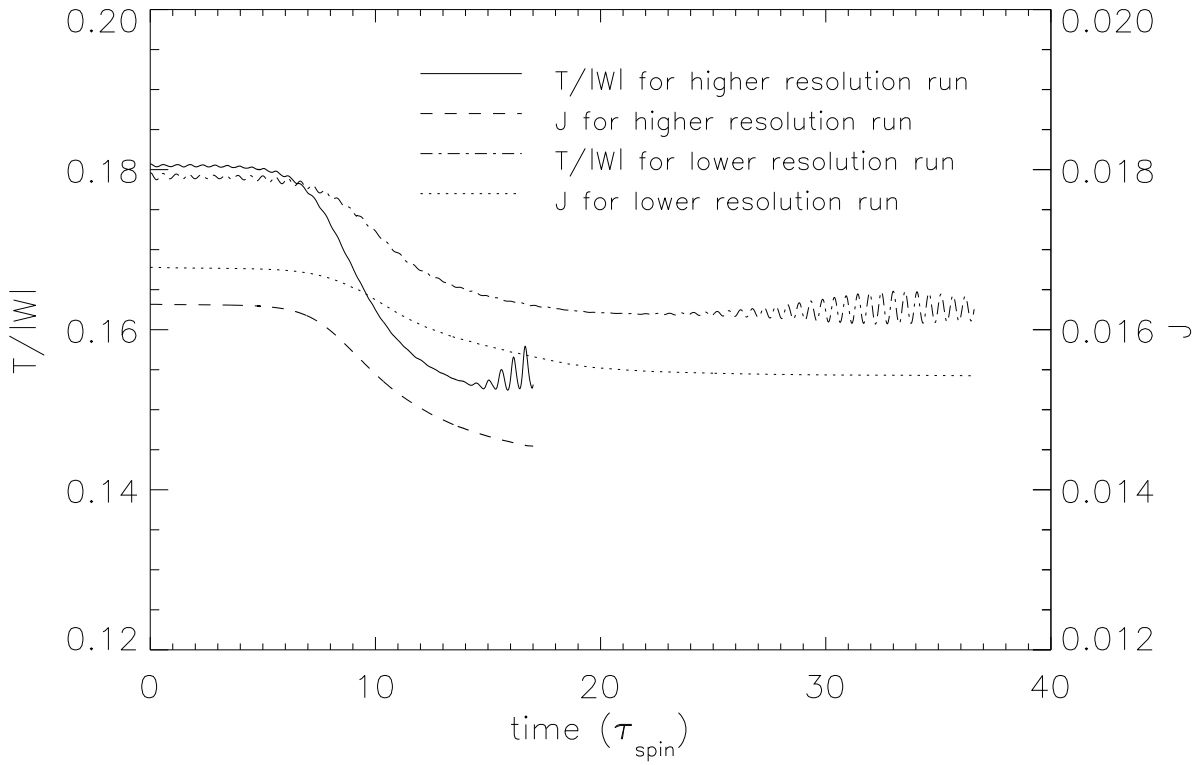

Figure 6.19: The time-evolution of the angular momentum J (dotted curve) and the energy ratio $T/|W|$ (dashed-dotted line) from model ROT179 on a grid of resolution $66 \times 66 \times 64$; J is in dimensionless code units, time is shown in units of the initial rotation period of the model. Curves from Fig. 6.5 are also shown in order to provide points of comparison with the higher resolution , model ROT181 evolution. Both quantities show similar time-decreasing behavior in both of the two models except that the characteristic decaying times are different.

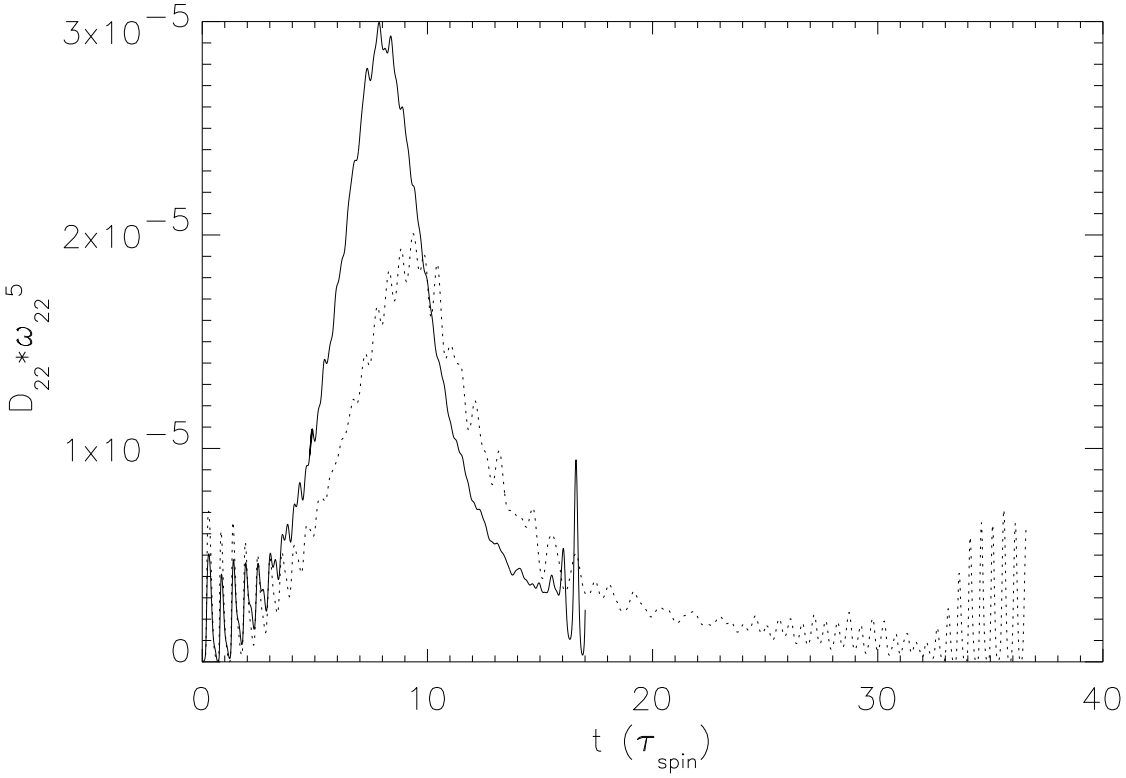

Figure 6.20: From model ROT179 on a grid of resolution $66 \times 66 \times 64$, the dotted curve depicts the time-evolution of the product $\omega_{22}^5 |D_{22}|$, which indicates the strength of $\Phi_{\rm GR}$ in the equation of motion. Time is shown in units of the initial rotation period. As a comparison, the solid curve (taken from Fig. 6.7) shows the same quantity from model ROT181 evolution. These two curves peak at different times and have a very obvious time shifting feature.

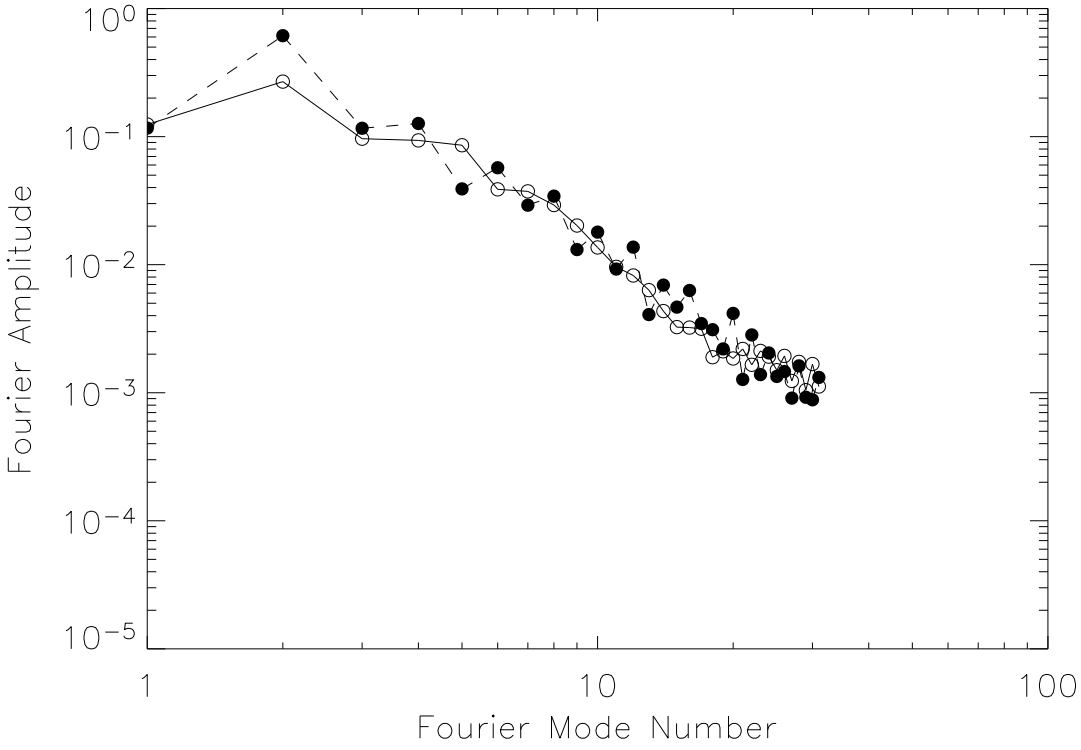

Figure 6.21: A spectrum of the Fourier-mode amplitude of the azimuthal density distribution is shown at time $t = 11\tau_{\rm spin}$ (filled circles), when the bar was well-developed, and at time $t = 36\tau_{\rm spin}$ (open circles), after the higher-order modes destroyed the coherent bar in the evolution of model ROT179 on a grid of resolution $66 \times 66 \times 64$. To guide the eye, amplitudes determined for various modes at the same time are connected by straight line segments.

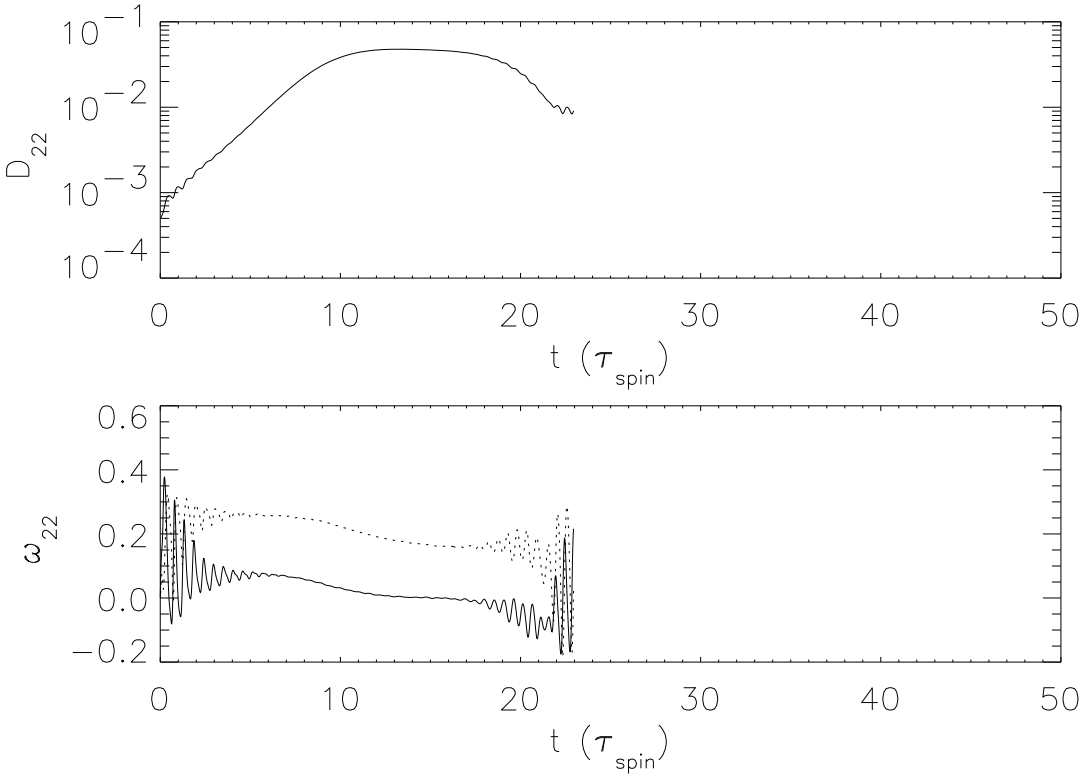

Figure 6.22: Same as Fig. 6.4, but the results are from model ROT179 on a grid of resolution $66 \times 66 \times 128$. It is very interesting that the turbulence instability in model ROT179 happens roughly at the same time as it did in in model ROT181.

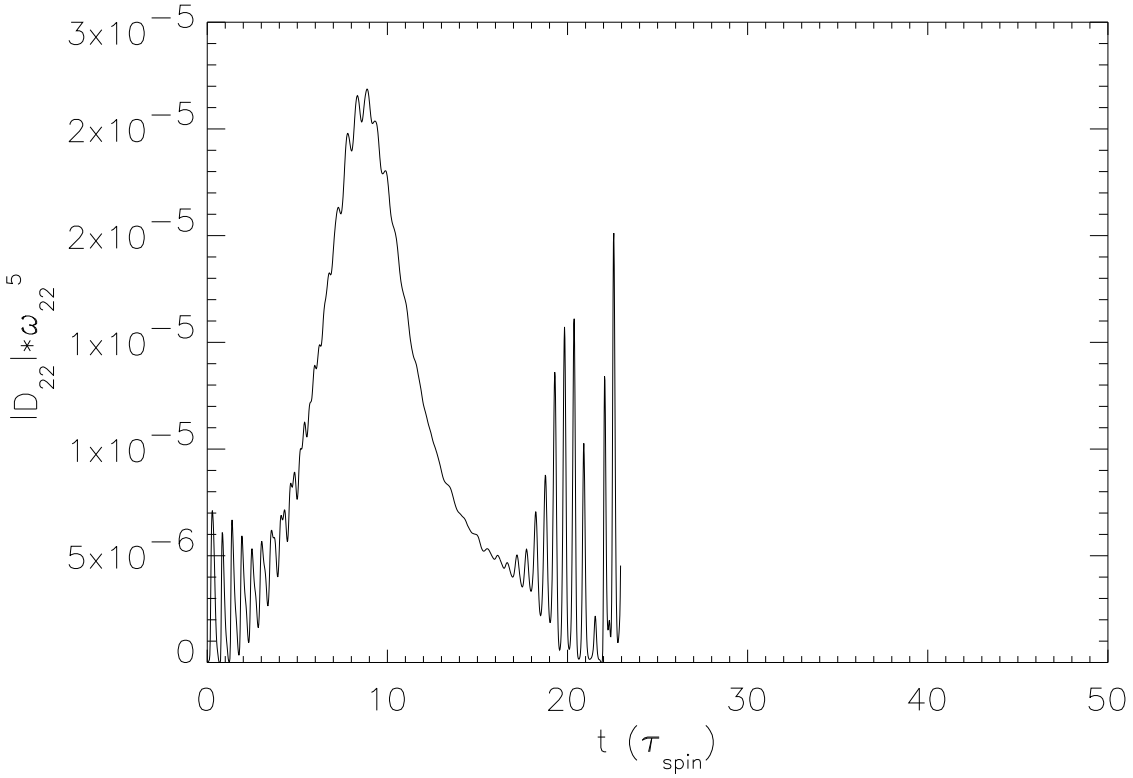

Figure 6.23: Same as Fig. 6.7, but from model ROT179 on a grid of resolution $66 \times 66 \times 128$.

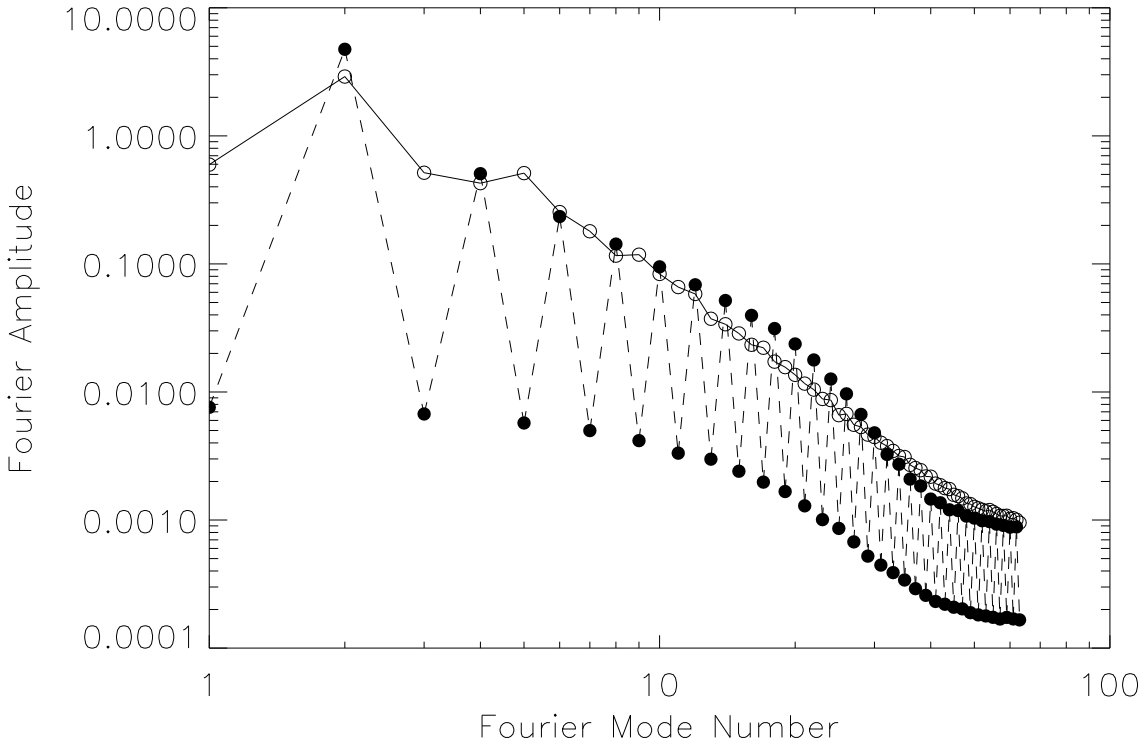

Figure 6.24: Same as Fig. 6.14, but from model ROT179 on a grid with resolution $66 \times 66 \times 128$. The filled circles are from when the bar was well-developed, and the open circles are after the higher-order modes destroyed the coherent bar.

7. Summary and Conclusions

Using nonrelativistic, numerical hydrodyamical techniques coupled with a post-Newtonian treatment of GRR forces, we have simulated the nonlinear development of the secular bar-mode instability in rapidly rotating neutron stars (approximated by $n = 0.5$ polytropes). In each simulation we have artificially enhanced the strength of the GRR force term in the equation of motion (by selecting values of the parameter $\kappa > 1$) in order to be able to follow the secular development of the bar with a reasonable amount of computing resources. In each case, however, κ was set to a small enough value that the amplitude of the mass-quadrupole moment changed slowly, compared to the dynamical time scale of the system, thus ensuring that the system as a whole remained in dynamical equilibrium.

We first tested our simulation technique by studying the evolution of the $\ell = m = 2$ bar-mode in a nonrotating neutron star model (model SPH) on a cylindrical grid having a resolution with $66 \times 130 \times 128$ in the radial, vertical, and azimuthal directions, respectively. According to linear theory, the bar-mode in this model is stable and should die out over time. In order to excite the $\ell = m = 2$ bar-mode, we applied to the initial neutron star model density and velocity perturbations, which closely mimicked the eigenfunctions of the bar-mode as described by linear theory. The results from our evolution of this model were in very close agreement with predictions: the developing bar-mode exhibited an azimuthal oscillation frequency within 3% of the frequency predicted by linear theory, and the amplitude of the bar-mode damped at a rate that was within 15% of the rate predicted by linear theory.

Next, we evolved a rapidly rotating model (ROT181), which was predicted by linear theory to be secularly unstable toward the growth of the bar-mode driven by gravitational radiation. The resolution of this simulation was $130 \times 98 \times 128$ in the radial, vertical, and azimuthal directions, respectively. From the *early* "linear-amplitude" phase of this model's evolution, we measured the bar-mode's azimuthal oscillation frequency and its exponential

growth rate; the values are summarized in Table 6.1, together with those of model SPH. The oscillation frequency $\langle\omega_{\rm r}\rangle/\Omega_0$ was almost an order of magnitude smaller than in model SPH, and $\langle\omega_{\rm i}\rangle/(\Omega_0\kappa)$ was four orders of magnitude smaller than (and had the opposite sign of) the value measured in model SPH. Both of these frequency values reflect the fact that model ROT181 was rotating only slightly faster than the marginally unstable model (predicted to have $T/|W| \approx 0.14$), in which both components of ω_{22} should be precisely zero. We watched the unstable bar-mode grow up to and saturate at a sufficiently large, nonlinear amplitude that the bar-like distortion was clearly visible in two- and three-dimensional plots of isodensity surfaces. The nonlinear bar that formed from this GRR-driven secular instability had a Dedekind-like ellispoidal structure; that is, it had a very large internal rotation yet maintained a very low pattern frequency compared to the initial spin rate of the star.

This nonlinear Dedekind-like bar structure persisted for several rotation periods. During this *intermediate* phase of the ROT181 model evolution, we tracked the frequency and amplitude of the gravitational-wave radiation that should be emitted from the configuration due to its time-varying mass-quadrupole moment. Our model's evolution in a "strain-frequency" diagram closely matched the evolutionary trajectory predicted by Lai & Shapiro (1995), lending additional credibility to their relatively simple (and inexpensive) way of predicting the evolution of such systems as well as to our first attempt to model such an evolution using nonlinear hydrodynamical techniques.

During the *late* phase of our model ROT181 evolution, the bar lost its coherent structure and the system evolved to a much more complex nonaxisymmetric configuration with high order modes growing to a significant amplitude. The general features of this *late* phase of the evolution were reproduced even when the GRR forces were turned off and when a very similar model (ROT179) was evolved on a computational grid that had a coarser resolution. So while the size and shape of the *intermediate* phase "Dedekind-like" structure of our model may well have been influenced strongly by the excessive strength of the GRR

force used in our simulation, it appears as though the final complex "turbulent" phase of the evolution was governed by purely hydrodynamical phenomena.

It is not clear what physical mechanism was responsible for the development of the small-scale structure and subsequent destruction of the bar during the *late* phase of the evolution of model ROT181. Because the bar's structure was "Dedekind-like" – that is, fluid inside the bar was moving along elliptical streamlines with a mean frequency that was significantly higher than the bar pattern frequency – it is tempting to suggest that the small-scale structure arose due to differential shear. But, according to Hawley, Balbus & Winters (1999), coriolis forces are able to stabilize differentially rotating, astrophysical flows against shearing instabilities even in accretion disks where the shear is much stronger than in our "Dedekind-like" bar. (See, however, Longaretti 2002 for an opposing argument.) Furthermore, other models of differentially rotating astrophysical bars (Cazes & Tohline, 2000; New, Centrella & Tohline, 2000) do not appear to be susceptible to the dynamical instability that destroyed the bar in our ROT181 model evolution. We suspect, instead, that the late-time behavior of model ROT181 results either from nonlinear coupling of various oscillatory modes within the star, or from an "elliptic flow" instability similar to the one identified in laboratory fluids that are forced to flow along elliptical streamlines. The dissipative effect of mode-mode (actually, three-mode) coupling has been examined in depth by Schenk et al. (2002) and Arras et al. (2003) in the context of the r-mode instability in young neutron stars, but the effect has not yet been studied to the same degree in relation to the $\ell = m = 2$ f-mode. Lifschitz & Lebovitz (1993), Lebovitz & Lifschitz (1996), and Lebovitz & Saldanha (1999) have demonstrated that the "elliptic flow" instability seen in laboratory fluids is likely to arise in self-gravitating ellipsoidal figures of equilibrium, especially if they have "Dedekind-like" internal flows. Additional analysis and, very likely, additional nonlinear simulations will be required before we are able to determine which (if either) of these mechanisms was responsible for the destruction of the bar in our ROT181 model evolution.

Our nonlinear simulation of model ROT181 demonstrates that when a rapidly rotating neutron star becomes unstable to the secular bar-mode instability, the bar-like distortion may grow to nonlinear amplitude and thereby become a strong source of gravitational radiation. However, it will not be a long-lived continuous-wave source, as one might optimistically have expected; in our simulation, the nonlinear-amplitude bar survived fewer than ten rotation periods. In a real neutron star the GRR forces will be much weaker than those of our simulation, so we expect the bar mode to grow and persist for many more rotation periods. However, we also expect the amplitude of the bar mode to saturate at a much lower amplitude in a real neutron star. Nevertheless, we expect the bar mode to persist in rapidly rotating neutron stars long enough to allow gravitational radiation to remove sufficient angular momentum for them to relax into a secularly stable equilibrium state. Thus the amount of angular momentum radiated away in real neutron stars should be comparable to that in our simulation. While such astrophysical systems may not be the easiest sources to detect with broadband, gravitational-wave detectors such as LIGO because the frequency of the emitted radiation will change steadily with time, our estimates suggest that gravitational waves arising from the excited secular bar-mode instability in rapidly rotating neutron stars could well be detectable in the not too distant future from neutron stars as far away as 32 ± 3 Mpc. This includes galaxies in the Virgo cluster.

Our results have cast some light on the long-believed evolutionary path of a secularly unstable rotating stars: According to the classical theory, such a configuration would evolve along a sequence of Dedekind-like ellipsoids under the influence of gravitational radiation and end up as a bar-like configuration that is stationary in the inertial frame yet maintains large internal rotational flows. Our results show that the bar-like structure that forms as a result of this GRR instability becomes dynamically unstable to high order turbulence while evolving toward the "stationary" figure. Hence, it is very unlikely that rotating neutron stars that become secularly unstable to the bar-mode instability end up as Dedekind-like

ellipsoidal configurations under the influence of gravitational radiation. This also suggests that it is very unlikely that Dedekind-like ellipsoids exist anywhere in our universe.

After submitting our results for publication (Ou, Tohline, & Lindblom, 2004), we became aware that Shibata & Karino (2004) have just completed an investigation similar to the one presented here in which they have utilized post-Newtonian simulations to study the nonlinear development of the secular bar-mode instability in rapidly rotating neutron stars. Their initial models were differentially rotating, $n = 1$ ($\Gamma = 2$) polytropes with $0.2 \lesssim T/|W| \lesssim 0.26$. The *early* and *intermediate* phases of their model evolutions agree well with the results of our model ROT181 evolution, that is, the bar-mode grew exponentially at rates consistent with the predictions of linear theory and reached a nonlinear amplitude, producing an ellipsoidal star of moderately large ellipticity. The strength of the GRR force used in our simulations was considerably larger than theirs. This may explain why the bar mode grows to a larger amplitude and why, in turn, there is a more significant decrease in the pattern frequency of the bar as it evolves toward a Dedekind-like configuration in our simulation. This may also explain why the bar mode structure was ultimately destroyed by short wavelength disturbances in our evolutions while such turbulence had not yet developed in theirs.

Bibliography

Abbott, B. et al. (LIGO Scientific Collaboration) 2004, PRD, 69, 102001(21)

Abramovici, A. et al. 1992, Science, 256, 325

Acernese, F. et al. 2002, Class. Quant. Grav., 19, 1421

Andersson, N. 2003, Classical and Quantum Gravity, 20, 105

Arras, P., et al. 2003, ApJ, 591, 1129

Backer, D. C., et al. 1982, Nature, 300, 615B

Brown, J. D. 2000, PRD, 62, 084024

Cazes, J. E., & Tohline, J. E. 2000, ApJ, 532, 1051

Cappellaro, E., Evans, R., & Turatto, M. 1999, Astronomy. & Astrophysics, 351, 459

Chandrasekhar, S. 1969, Equilibrium Figures of Equilibrium, New Haven, CT: Yale Univ. Press

Chandrasekhar, S. 1970, ApJ, 161, 561

Cohl, H. S., Tohline, J. E., 1999, ApJ, 527, 86

Comins, N. 1979a, MNRAS, 189, 233

Comins, N. 1979b, MNRAS, 189, 25

Cox, J. P., 1980, The theory of Stellar Pulsation (Princeton Press)

Cutler, C. 1991, ApJ, 374, 248

Cutler, C., & Lindblom, L. 1987, ApJ, 314, 234

Cutler, C., & Lindblom, L. 1992, ApJ, 385, 630

Detweiler, S. L., & Lindblom, L. 1977, ApJ, 213, 193

Di Girolamo, T., & Vietri, M. 2002, ApJ, 581, 519

Dimmelmeier, H., Font, J., & Müller, E. 2002, Astronomy & Astrophysics, 388, 917

Dimmelmeier, H., Font, J., & Müller, E. 2002, Astronomy, & Astrophysics, 393, 523

Durisen, R. H., Gingold, R. A., Tohline, J. E., & Boss, A. P. 1986, ApJ, 305, 281

Durisen, R. H., Tohline, J. E., 1985, in Protostars & Planets II (Tuscon: Univ. of Arizona Press)

Finn, L. S., & Evans, C. R. 1990, ApJ, 351, 588

Flowers, E., & Itoh, N. 1976, ApJ, 206, 218

Friedman, J. 1978, Comm. Math. Phys., 62, 247

Friedman, J., & Schutz, B. F. 1978, ApJ, 222, 281

Gossler, S., et al. 2002, Class. Quant. Grav., 19, 1835

Gressman, P., Lin, L.-M., Suen, W.-M., Stergioulas, N., & Friedman, J. L. 2002, Phys. Rev. D, 66, 041303

Hachisu, I. 1986, ApJs, 61, 479

Hawley, J. F., Balbus, S. A., & Winters, W. F. 1999, ApJ, 518, 394

Hulse, R. A., Taylor, J. H., 1975, ApJ, 195, L51

Imamura, J. N., Friedman, J. L., & Durisen, R. H. 1985, ApJ, 294, 474

Imamura, J. N., Toman, J., Durisen, R. H., Pickett, B. K., Yang, S., 1985, ApJ, 444, 363

Ipser, J. R., & Lindblom, L. 1990, ApJ, 355, 226

Ipser, J. R., & Lindblom, L. 1991, ApJ, 373, 213

Jones, P. B. 1971, Proc. Roy. Soc. London A, 323, 111

Kalogera, V., Narayan, R., Spergel, D. N., & Taylor, J. H. 2001, ApJ, 556, 340

Karino, S., & Eriguchi, Y. 2003, ApJ, 592, 1119

Kazanas, D., & Schramm 1977, ApJ, 214, 819

Kokkotas, K. D. 2004, Class. Quant. Gravity, 21, 501.

Lai, D., & Shapiro, S. L. 1995, ApJ, 442, 259

Lebovitz, N. R., 1987, in Highlights of Astronomy Volume 8, ed. D. McNally (Boston:Kluwer Academic Publishers), 129

Lebovitz, N. R., & Lifschitz, A. 1996, ApJ, 458, 699

Lebovitz, N. R., & Saldanha, K. I. 1999, Physics of Fluids, 11, 3374

Lifschitz, A., & Lebovitz, N. 1993, ApJ, 408, 603

Lindblom, L. 1997, in General Relativity and Gravitation, edited by M. Francaviglia, G. Longhi, L. Lusanna, E. Sorace, World Scientific, pp. 237–258.

Lindblom, L. 2001, in Gravitational Waves: A Challange to Theoretical Astrophysics, edited by V. Ferrari, J. C. Miller, L. Rezzolla, ICTP Lecture Notes Series, pp. 257–275.

Lindblom, L., & Detweiler, S. 1977, ApJ, 211, 565

Lindblom, L., & Detweiler, S. 1979, ApJ, 232, L101

Lindblom, L., & Hiscock, W. A. 1983, ApJ, 267, 384

Lindblom, L., & Mendell, G. 1995, ApJ, 444, 804

Lindblom, L., Tohline, J. E., & Vallisneri, M. 2001, Phys. Rev. Letter, 86, 1152

Lindblom, L., Tohline, J. E., & Vallisneri, M. 2002, PRD, 65, 084039

Lindblom, L., private communication, 2004

Liu, Y. T., PRD, 65, 124003

Longaretti, P.-Y. 2002, ApJ, 576, 587

Managan, R. A. 1985, ApJ, 294, 463

Motl, P. M., Tohline, J. E., & Frank, J. 2002, ApJs, 138, 121

New, K. C. B., Centrella, J. M., & Tohline, J. E. 2000, PRD, 62, 064019

Ott, C. D., Burrows, A., Livne, E., & Walder, R. 2004, ApJ, 600, 834

Ou, S., Tohline, J. E., & Lindblom, L. 2004, ApJ, 617, in press

Owen, B., Lindblom, L. 2002, Class. Quant. Grav., 19, 1247

Pickett, B. K., Cassen, P., Durisen, R. H., & Link, R. 1998, ApJ, 504, 468

Sawyer, R. F. 1989, PRD, 39, 3804

Schenk, A. K., Arras, P., Flanagan, É. É., Teukolsky, S. A., & Wasserman, I. 2002, PRD, 65, 024001

Shapiro, S. L., & Zane, S. 1998, ApJs, 117, 531

Shibata, M., Karino, S., Eriguchi, Y., 2003, MNRAS, 334,L27

Shibata, M., Karino, S., Eriguchi, Y., 2003, MNRAS, 343,619

Shibata, M., & Karino, S. 2004, Phys. Rev. D, in press (astro-ph/0408016)

Stergioulas, N. 2003, Living Rev. Relativity, 6, 3 [Online article]: cited on 26 September 2004 http://www.livingreviews.org/lrr-2003-3/

Stergioulas, N., & Friedman, J. L. 1998, ApJ, 492, 301

Tassoul, J.-L. 1978, Theory of Rotating Stars, Princeton: Princeton University Press

Tagoshi, H. et al. (TAMA300 collaboration) 2001, PRD, 63, 062001

Thompson, C., & Duncan, R. C. 1993, ApJ, 408, 194

Thorne, K. S., 1969, ApJ, 158, 997

Tohline, J. E. 1984, ApJ, 285, 721

Tohline, J. E., Durisen, R. H., & McCollough, M. 1985, ApJ, 298, 220

Williams, H. A., & Tohline, J. E. 1988, ApJ, 334, 449

Willke, B. et al. 2002, Class. Quant. Grav., 19, 1377

Yoshida, S., & Eriguchi, Y. 1995, ApJ, 438, 830

APPENDIX A: Determination of the Speed of Light in Hydrocode Units

As long as the evolution of a self-gravitating, polytropic gas is modelled using a Newtonian gravitational field, each simulation can be performed in dimensionless units (we typically employ "hydrocode" units for which $G = r_{\rm grid} = \rho_{\rm max} = 1$), then be scaled later to systems having a variety of masses and radii (Williams & Tohline 1978). Once relativistic effects are taken into account, however, the speed of light enters the problem as a fundamental parameter and dimensionless "hydrocode" units are no longer especially useful. We discuss here how the value of the speed of light is determined in hydrocode units for a specific neutron star simulation.

First, we specify the mass and radius of the neutron star under investigation, which in turn defines the relevant free-fall velocity of the system. For example, using the mass and equatorial radius specified in Table 1 ($M = 1.4{\rm M}_\odot = 2.8 \times 10^{33}$ g, $r_{\rm eq} = 12.5$ km),

$$v_{\rm ff} \equiv r_{\rm eq}\Omega_{\rm o} = r_{\rm eq}\sqrt{\pi G \bar{\rho}_0} = 1.059 \times 10^5 \text{ km s}^{-1} . \tag{A.1}$$

From this, we determine the ratio of $v_{\rm ff}$ to the speed of light c in this selected neutron star,

$$\alpha \equiv v_{\rm ff}/c = 0.3527 . \tag{A.2}$$

Now, in hydrocode units, our selected model (properties listed in Table 1) exhibits the following characteristic free-fall velocity:

$$v_{\rm ff}|_{\rm code} = r_{\rm eq}\Omega_{\rm o} = 1.102 . \tag{A.3}$$

Enforcing the proper ratio α of the free-fall velocity to the speed of light therefore demands that in the hydrocode, the speed of light,

$$c_{\rm code} = \frac{v_{\rm ff}|_{\rm code}}{\alpha} = 3.122 . \tag{A.4}$$

This is the value listed in column 3 of Table 1.

Hence, in the hydrocode the coefficient N_2 in the expression for the radiation reaction force was assigned the value,

$$N_2 = (8\pi G)/(75c^5) = 9.188 \times 10^{-3} . \tag{A.5}$$

APPENDIX B: Numerical Results of Rigidly Rotating Models

For incompressible rotating stars, i.e. $n = 0$ Maclaurin spheroid, it is possible to build uniformly rotating models ranging from $\beta = 0$ to $\beta = 0.5$ as the stars spins faster and faster. However, this is not true for uniformly rotating stars with a compressible equation of state. As the star spins up, the centrifugal force at the equator of the star would finally exceed gravity and cause mass to be shed from the star's equator. Therefore, for gas or fluid with different compressibility (or different values of n), there exists a certain critical limit varying with n, beyond which a uniformly rotating star will break up. James (1969) has shown that for $n > 0.808$, it is impossible to build a uniformly rotating stellar model with β above the critical limit for the secular bar-mode instability, e.g. $\beta = 0.14$. Figure B.1 shows our results of different sequences of uniformly rotating models for $n = 0.5, 1.0, 1.5$ that are built by our HSCF code. Along each sequence, the equatorial radius is fixed, then the polar radius is reduced in order to get uniformly rotating models that spin faster and faster. The vertical axis denotes the β value; the horizontal axis denotes the eccentricity of the object. As shown in the figure, there exists a maximum β value for each sequence. Only the maximum β of the $n = 0.5$ sequence has passed beyond the critical limit 0.14. Thus, in order to study the nonlinear development of the secular bar-mode instability, we have chosen $n = 0.5$, which denotes a pretty stiff equation of state for neutron stars.

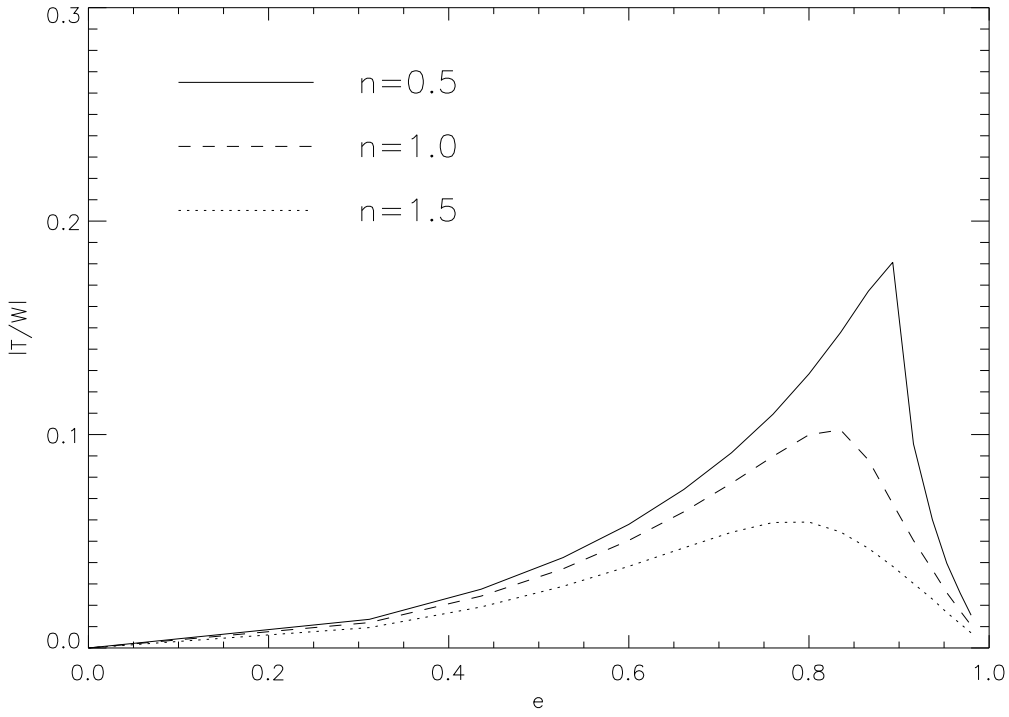

Figure B.1: The $\beta = |T/W|$ value versus the eccentricity e of uniformly rotating polytropes. The solid line denotes the sequence of $n = 0.5$; the dashed line denotes the sequence of $n = 1.0$; the dotted line denotes the sequence of $n = 1.5$. Among all three sequences, only the $n = 0.5$ sequence goes above the critical limit of secular bar-mode instability, i.e. $\beta = 0.14$.

APPENDIX C: The Perturbations Applied to Initial Models

From Eq. (12) of Ipser & Lindblom (1990), the velocity perturbation is

$$\delta v^a = iQ^{ab}\nabla_b \delta U, \tag{C.1}$$

where δU is the perturbed potential and the tensor Q^{ab} is defined in their equation (13).

In the nonrotating case, the angular velocity of the star $\Omega = 0$, thus Q^{ab} reduces to,

$$Q^{ab} = \frac{g^{ab}}{\omega}, \tag{C.2}$$

where ω is the eigenfrequency of each mode, and g^{ab} is the three metric related to the coordinate system. In cylindrical coordinate system, g^{ab} takes the form,

$$g^{11} = g_{11}^{-1} = 1, \tag{C.3}$$
$$g^{22} = g_{22}^{-1} = \varpi^2, \tag{C.4}$$
$$g^{33} = g_{33}^{-1} = 1; \tag{C.5}$$

all the other matrix elements vanish; and we obtain,

$$\delta v^{\varpi} = \frac{i}{\omega}\nabla_{\varpi}\delta U, \tag{C.6}$$
$$\delta v^{\phi} = \frac{i}{\omega\varpi^2}\nabla_{\phi}\delta U, \tag{C.7}$$
$$\delta v^{z} = \frac{i}{\omega}\nabla_{z}\delta U. \tag{C.8}$$

Here, we use ϖ for cylindrical radius and r for spherical radius. We can write the perturbed potential as the product of a pure spherical radial function $U(r)$ and Y_{22}, which yields,

$$\nabla_b \delta U = \nabla_b (U(r)Y_{22}) \tag{C.9}$$
$$= \sqrt{\frac{15}{32\pi}}\nabla_b (U(r)e^{2i\phi}\sin^2\theta). \tag{C.10}$$

In the cylindrical coordinate system, we have

$$\nabla_{\varpi}\sin^2\theta = \nabla_{\varpi}\left(\frac{\varpi^2}{\varpi^2+z^2}\right) \tag{C.11}$$
$$= \frac{2\varpi}{\varpi^2+z^2} - \frac{2\varpi^3}{(\varpi^2+z^2)^2} \tag{C.12}$$
$$= \frac{2\sin\theta}{r} - \frac{2\sin^3\theta}{r} \tag{C.13}$$

$$= \frac{2\sin\theta\cos^2\theta}{r}, \tag{C.14}$$

$$\nabla_z \sin^2\theta = \nabla_z(\frac{\varpi^2}{\varpi^2+z^2}) \tag{C.15}$$

$$= -\frac{2\varpi^2 z}{(\varpi^2+z^2)^2} \tag{C.16}$$

$$= -2\frac{\sin^2\theta\cos\theta}{r}. \tag{C.17}$$

After some manipulation of the above equations and taking the real part of the equations of velocity perturbations, we obtain the following expressions for the three components of velocity perturbations:

$$\delta v^{\varpi} = -\sqrt{\frac{15}{32\pi}}\frac{1}{\omega}\sin 2\phi(\partial_{\varpi}U(r)\sin^2\theta + U(r)2\cos^2\theta\frac{\sin\theta}{r}), \tag{C.18}$$

$$\delta v^{\phi} = -\sqrt{\frac{15}{32\pi}}\frac{1}{\omega}\frac{2U(r)\cos 2\phi\sin^2\theta}{\varpi}, \tag{C.19}$$

$$\delta v^{z} = \sqrt{\frac{15}{32\pi}}\frac{1}{\omega}\sin 2\phi(\frac{2U(r)\sin^2\theta\cos\theta}{r} - \partial_z(U(r))\sin^2\theta). \tag{C.20}$$

Vita

Shangli Ou was born in Junlian, China, on December 14, 1973. He graduated from Junlian High School in 1991. He then entered Nanjing University and earned his bachelor's degree of science in astronomy in 1995.

From 1995 to 1999, Shangli worked as a mission analysis engineer in the Geo-synchronous Satellite Division in Beijing Institute of Spacecraft System Engineering, Bejing. In 1997, he met his wife, Yu Zhao. They were married in 2000.

From 1999 to 2004, Shangli has been attending the graduate school at Louisiana State University. Shangli expects to receive his doctorate degree in December 2004.